N° d'ordre : 3609

THÈSE

Présentée à

L'UNIVERSITÉ BORDEAUX 1

ÉCOLE DOCTORALE DES SCIENCES CHIMIQUES

Par

Vanessa SCHMIDT GIACOMELLI

Pour obtenir le grade de

DOCTEUR

Spécialité : **POLYMÈRES**

****

Nanoparticules Décorées par des Protéines: Vésicules Lipidiques

Unilamellaires et Micelles à Base de Copolymères à Blocs

****

Soutenue le : 03 juillet 2008

Après avis de :

M. P. LABBÉ	Professeur, Université Joseph Fourier	**Rapporteur**
M. C. ROCHAS	Directeur de Recherches, Université Joseph Fourier	**Rapporteur**

Devant la commission d'examen formée par :

M. A. DEFFIEUX	Directeur de Recherches, Université Bordeaux 1	**Président**
M. P. LABBÉ	Professeur, Université Joseph Fourier	**Rapporteur**
M. C. ROCHAS	Directeur de Recherches, Université Joseph Fourier	**Rapporteur**
M. A. BRISSON	Professeur, Université Bordeaux 1	**Examinateur**
M. V. SOLDI	Professeur, Universidade Federal de Santa Catarina	**Examinateur**
M. R. BORSALI	Directeur de Recherches, Université Bordeaux 1	**Examinateur**

- 2008 -

To Cristiano,

Assunta and Edoardo.

Abstract (English)

Université Bordeaux 1

Protein decorated Nanoparticules: Small Unilamellar Lipid Vesicules and Block Copolymers Micelles.

by *Vanessa Schmidt Giacomelli*

The formation of protein Annexin-A5 decorated (bio-functionalized) nanoparticles is of particular interest in micelle-mediated target drug delivery, *in vivo* magnetic resonance imaging, or controlled fabrication of biochips. This work describes an easy access to the synthesis and manipulation of block copolymer nano-objects exhibiting binding ability for the Annexin-A5 protein. Well-defined spherical micelles containing negatively charged phosphonic diacid groups – which are potential binding sites for Annexin–A5 proteins – at their hydrophilic periphery originate from the self-assembly of polystyrene-*b*-poly(2-phosphatethyl methacrylate-*stat*-2-hydroxyethyl methacrylate) (PS-*b*-P(PEMA-*stat*-HEMA)) and poly(*n*-butyl acrylate)-b-poly((1-ethoxycarbonyl)vinylphosphonic diacid) (PBuA-*b*-PECVPD) amphiphilic macromolecules in aqueous media. The above cited block copolymers were synthesized mainly *via* Atom Transfer Radical Polymerization (ATRP). The herein discussed approach allows precise control over micellar dimensions and properties such as core radius (*i.e.*, payload capacity), corona width, and density of phosphate groups at the micelle periphery.

The polyelectrolyte behavior of block copolymer micelles originated from the self-assembly of block copolymers chains and their binding to Annexin-A5 protein was studied in detail by a combination of potentiometry, static and dynamic light scattering (SLS and DLS), small angle x-ray scattering (SAXS), transmission electron microscopy (TEM) and cryo-transmission electron microscopy (cryo-TEM), quartz crystal microbalance with dissipation monitoring (QCM-D), and polyacrylamide gel electrophoresis (PAGE).

Keywords: Block Copolymers, Self-Assembly, Micelles, Polyelectrolyte Behavior, Light Scattering, X-Ray Scattering, Transmission Electron Microscopy, protein decorated nanoparticles, Annexin-A5 protein, Atom Transfer Radical Polymerization (ATRP).

Résumé (Français)

Université Bordeaux 1

Nanoparticules Décorées par des Protéines: Vésicules Lipidiques Unilamellaires et Micelles à Base de Copolymères à Blocs
par *Vanessa Schmidt Giacomelli*

La formation de nanoparticules bio-fonctionnalisées et décorées par des protéines peut être très intéressante pour la détection et le ciblage de cellules, ainsi que pour et la vectorisation des principes actifs (médicaments). Ce manuscrit décrit la synthèse et la manipulation de nanoparticules qui se lient à la protéine Annexine-A5. Des micelles sphériques à base des copolymères à blocs portant des groupes diacide phosphonique chargés négativement – ces groupes ont la faculté d'interagir avec l'Annexine-A5 en présence d'ions calcium – ont été obtenues par l'auto-assemblage de copolymères à blocs polystyrène-b-poly(méthacrylate de 2-phosphatéthyle-stat-méthacrylate de 2-hydroxyéthyle) (PS-b-P(PEMA-stat-HEMA)) et poly((1-éthoxycarbonyl) vinyldiacide phosphonique)-b-(poly(acrylate de n-butyle) (PECVPD-b-PBuA) en milieu aqueux. Ces copolymères à blocs ont été synthétisés par polymérisation radicalaire par transfert d'atome (ATRP), de façon à contrôler leurs propriétés (longueur des blocs, charge, etc.) et celles des nanoparticules auto-organisées (épaisseur de la couronne, densité des groupements phosphates à la surface, etc.)

Le comportement polyélectrolyte des micelles chargées négativement et leur interaction avec l'Annexine-A5 ont été étudiés par plusieurs techniques : potentiométrie, diffusion dynamique et statique de la lumière (DLS et SLS), diffusion des rayon-X aux petits angles (SAXS), microscopie électronique à transmission (TEM et cryo-TEM), microbalance à crystal de quartz (QCM-D), et électrophorèse sur gel de polyacrylamide (PAGE).

Mots-Clé: Copolymères à blocs, auto-assemblage, micelles, effet polyélectrolyte, diffusion de lumière, diffusion de rayon-X, microscopie électronique à transmission, nano-objets décorés par des protéines, protéine Annexine-A5, Polymérisation Radicalaire par Transfert d'Atome (ATRP).

Table of Contents

_____

Introduction (English)

The present thesis work, wich is a result of a collaboration between the Laboratoire de Chimie des Polymères Organiques (LCPO) and the Laboratoire d'Imagerie Moléculaire et NanoBioTechnologie (IECB), both at Université Bordeaux 1, deals with the decoration of nanosized particles, small unilamellar vesicles (SUVs) and diblock copolymers micelles, with the Annexin-A5 protein.

The interaction between nano-sized lipid-based assemblies and annexins – a family of proteins that participate in a variety of membrane related processes as blood coagulation and inflammation, and bind to biological membranes through negatively charged phospholipids in a calcium-dependent manner – has recently attracted increasing attention worldwide. Such protein binding process is reversible, and removal of calcium ions by chelating agents leads to a liberation of annexins from the phospholipid matrix. Depending on the environmental surroundings, protein-decorated assemblies may interact with specific types of receptors. For instance, Annexin-A5 protein binds with strong affinity to phosphatidylserine moieties, whose exposition is considered a hallmark of programmed cell death or apoptosis. The LIMNT-IECB has developed an ensemble of modified Annexin-A5 molecules which can be used to target various types of cell receptors.[1, 2] Consequently, great potential for simultaneous in vivo monitoring and cancer treatment is expected for protein/drug carrier (e.g. micelles, vesicles) assemblies.

One of the most fascinating properties of amphiphilic block copolymers is their ability of the self-assembly into ordered structures in solution or even in bulk. The most common of these structures are illustrated in Figure 1.1. In recent years, the interest in these objects as potential delivery vehicles for pharmaceuticals and gene therapy agents has grown enormously, due to the fact that they can stabilize hydrophobic molecules with otherwise limited water solubility and/or decrease the high toxicity of potent anti-tumor drugs to healthy cells. However, targeting tumor sites and associated cells still remains a significant challenge for the development of micelle-mediated drug delivery systems. Several strategies have been developed to achieve this goal, which consist mainly in i) the use of stimuli (pH, temperature, applied magnetic fields)-responsive macromolecules at near physiological conditions and ii) the utilization of molecular markers (piloting functions that recognize and target specific sites in cancerous tissues). In both cases, however, landmark advances seem to be those linking

biological world, with its elaborate architectures, properties, and functions, to drug delivery nano-carriers.
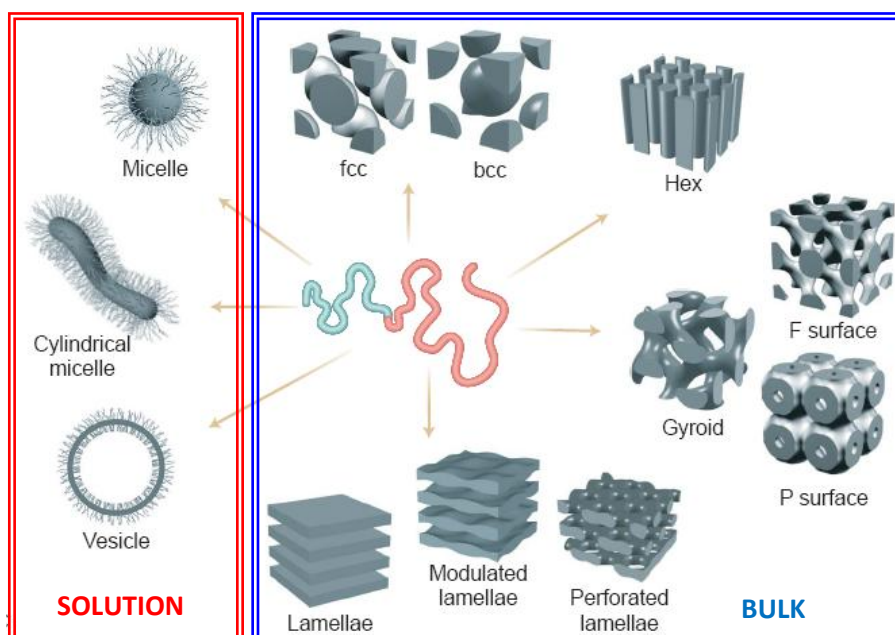
Figure I(EN). The most common self-assembled structures of amphiphilic diblock copolymers in solution and in bulk. Scheme formerly proposed by Förster and Plantenberg,[3] and Bucknall and Anderson. [4]

Objectives

The challenge of this work was to give (bio)functionality to more robust objects (micelles made from block copolymer or nano-organized bulk films), and offer another possibility as compared to liposomes with thin and deformable bilayers. The applications of such polymer-protein assemblies extend from target drug delivery to controlled fabrication of biochips.

The first objective of this work was to synthesize diblock copolymers having phosphate groups (similar to phospholipids) with ability to bind the Annexin-A5.

Once the first objective was successfully reached, the second step comprised the study of the self-assembly characteristics of such diblock copolymers in aqueous solution and in bulk. The presence of negatively charged phosphate groups in the corona of such micellar aggregates confer to these objects an interesting polyelectrolyte behavior. The influence of pH and salt concentrations on the assemblies was studied in details by SLS, DLS, SAXS and Cryo-TEM.

Finally, the third objective was to determine the nanoparticle-protein ability as a function of the copolymers molecular characteristics (degree of polymerization (DP), number of phosphate groups, polymer structure, etc.), and ultimately of the assemblies properties by combining techniques commonly used in different fields. In such a multidisciplinary investigation, spanning from polymer chemistry to biology, we take advantage of state-of-the-art instrumentation in these areas (SLS, DLS, QCM-D, PAGE).

Outline of the thesis

For the reader not familiar with the Anexinn-A5 protein, *Chapter 1* gives an introduction to its general characteristics, and to the principles of the Annexin-A5-phospholipid interaction. A literature review about block copolymers and Small Unilamellares Vesicles are also contemplated in the same chapter.

In *Chapter 2* the reader will find a brief description of the fundamentals of the techniques used to access the physical chemical properties of the nano-structures studied in the present work and the binding of the Annexin-A5 to these objects.

To prepare block copolymers with ability to bind the Annexin-A5 protein we first had to understand the binding between this protein and phospholipids. The SUVs characteristics and the SUV-Annexin-A5 interaction studied in solution by light scattering techniques are show in *Chapter 3.* This study was carried out to add more information to the current knowledge obtained by QCM-D and microscopy techniques.

Chapter 4 reports the results obtained for the first block copolymer synthesized with ability to bind the Annexin-A5 protein. The syntheses, characterization, self-assembly, polyelectrolyte behaviour, and the Annexin-A5 binding capacity of PBuA-*b*-PECVPD are presented. The same study was also undertaken using an alternative block copolymer system, PS-*b*-P(PEMA-co-HEMA) and the results are shown in *Chapter 5.* For the latter system, copolymers with different degree of *polymerization and density of phosphate groups are described.*

Finally, the Experimental Part provides all the details on the synthesis and characterization of amphiphilic block copolymers and the micelle-Annexin-A5 assemblies, as well as the SUV preparation and characterization, and the SUV-Annexin-A5 interaction. The description of equipments and setup used during the present work is also therein described.

Introduction (Français)

Ce travail de thèse est le résultat d'une collaboration entre le Laboratoire de Chimie des Polymères Organiques (LCPO) et le Laboratoire d'Imagerie Moléculaire et NanoBioTechnologie (LIMNT-IECB), de l'Université de Bordeaux 1. Il décrit la préparation et la décoration de nanoparticules (vésicules unilamellaires et micelles à base des copolymères à blocs) par la protéine Annexine-A5.

L'interaction entre les assemblages lipidiques et les Annexines – protéines qui sont impliquées dans plusieurs phénomènes biologiques au niveau des membranes, et qui se lient avec les membranes phospholipides négativement chargées– est un sujet de recherche qui attire l'attention de la communauté scientifique internationale. Cette liaison réversible se fait en présence des ions calcium, lesquels peuvent être complexés par certaines molécules (agents complexants) de façon à libérer l'Annexine de la surface lipidique. Le LIMNT-IECB a produit un ensemble d'outils moléculaires dérivés de l'Annexine-A5 qui permettent de cibler divers types de récepteurs cellulaires.[1, 2] Il a été déjà montré, par exemple, que des nano-objets (micelles, vésicules) contenant l'Annexine-A5 en surface pourront avoir des applications potentielles dans le domaine biomédical pour le diagnostique et l'évaluation de l'efficacité de traitements anti-cancéreux, en raison de la liaison de l'Annexine-A5 avec des molécules de phosphatidylserine qui sont spécifiquement présentes à la surface des cellules entrées en apoptose.

Une des plus remarquables propriétés des copolymères à blocs amphiphiles est leur capacité de s'auto-organiser en donnant lieu à des structures très bien définies aussi bien en solution qu'en masse. Les structures les plus couramment rencontrées sont illustrées dans la Figure 1.1. L'intérêt dans ces objets pour les applications pharmaceutiques a beaucoup augmenté ces dernières années car ils peuvent être utilisés dans la vectorisation des principes actifs (médicaments) grâce à leur capacité d'encapsuler, stabiliser, transporter et libérer certaines molécules insolubles dans les milieux aqueux (hydrophobes) et/ou encore réduire leur toxicité. Cependant, le ciblage des cellules cancéreuses par les micelles à base de copolymères à blocs reste toujours un grand défi. Différentes stratégies ont été développées dans cette thématique: i) l'utilisation des polymères qui répondent à des stimuli externes (pH, température, champ magnétique) et ii) l'utilisation de marqueurs (fonctions spécifiques qui peuvent guider les nanoparticules). Dans les deux cas, les plus grandes avancées obtenues sont clairement dues à la combinaison d'éléments biologiques et de nanostructures à base des polymères.

Objectifs

L'un des objectifs majeurs dans ce travail était la (bio)fonctionnalisation des nanostructures à base des copolymères à blocs (micelles et films) avec la protéine Annexine-A5 afin de développer des nouvelles stratégies de vectorisation de principes actifs hydrophobes. Pour y répondre, nous avons mis l'accent les aspects suivants : 1) synthèse des copolymères à blocs portant des fonctions phosphates (similaires aux groupements présents dans les phospholipides) capables d'interagir avec l'Annexine-A5 ; 2) étude de l'auto-assemblage des copolymères à blocs obtenus en solution et en masse ; analyse du comportement polyélectrolyte des structures présentant une surface négativement chargée ; 3) étude des interactions (liaisons) blocs-Annexine-A5 en fonction des différentes caractéristiques des copolymères préparés (degré de polymérisation, quantité de groupements phosphates, structure chimique, etc.), et par conséquence des assemblages obtenus en faisant appel à des techniques multidisciplinaires normalement utilisées par les polyméristes et les biologistes (SLS, DLS, QCM-D, TEM, cryo-TEM, PAGE).

Sommaire de la thèse

Pour les lecteurs non familiarisés avec l'Annexine-A5, le *Chapitre 1* donne une introduction sur les principales caractéristiques de cette protéine et son interaction avec les phospholipides. Une revue bibliographique sur les assemblages lipidiques et les copolymères à bloc est aussi présentée dans le même chapitre.

Dans le *Chapitre 2*, le lecteur trouvera une brève description des techniques utilisées pour l'étude des caractéristiques physico-chimiques des assemblages lipidiques et des micelles à base des copolymères à blocs et leur liaison avec l'Annexine-A5.
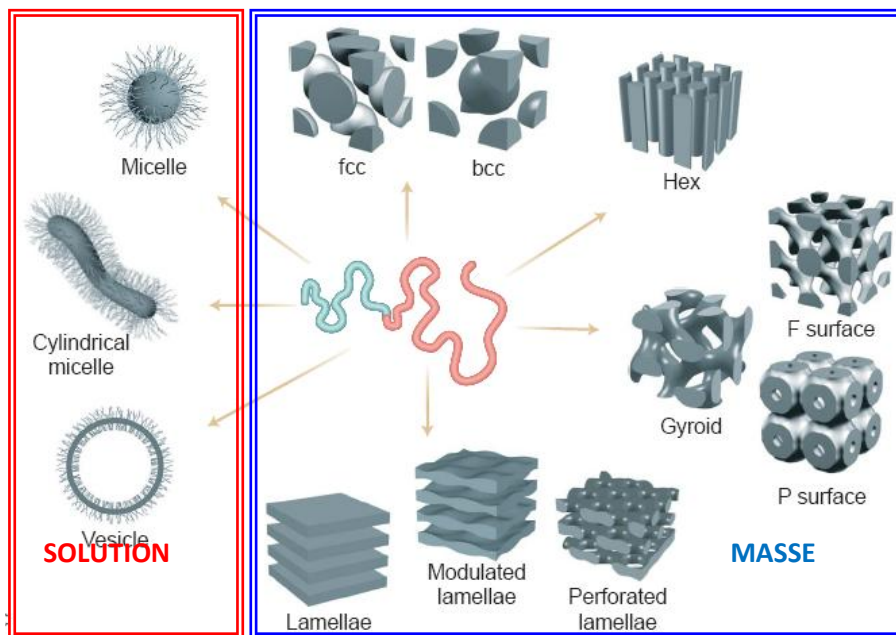
Figure I(FR). Structures les plus connues formées par des copolymères à blocs en solution et en masse. Proposée par Förster et Plantenberg,[3] et Bucknall et Anderson.[4]

Àfin de synthétiser des copolymères à blocs capables de se lier avec l'Annexine-A5 il faut, tout d'abord, comprendre les liaisons entre cette protéine et les assemblages lipidiques. La liaison entre cette protéine et de petites vésicules unilamellaires a été étudiée par des techniques de diffusion de la lumière. Les résultats obtenus sont présentés dans le *Chapitre 3*.

Dans le *Chapitre 4* sont réunis les résultats obtenus pour le premier copolymères à blocs préparé qui a clairement montré capacité à se lier à la protéine Annexine-A5. La synthèse, la caractérisation, l'auto-assemblage, l'effet polyélectrolyte et la liaison avec l'Annexine-A5 sont ~~donc~~ développés le long de ce chapitre. La même étude a été réalisée pour le deuxième système de copolymères à blocs, et les résultats sont décrits dans le *Chapitre 5*.

Finalement, la *Partie Expérimentale* décrit en détails les procédures adoptées pour la synthèse et la caractérisation des copolymères à blocs et les assemblages copolymères-Annexine-A5, aussi que la préparation et la caractérisation des petites vésicules unilamellaires et les assemblages SUV-Annexine-A5. La description des équipements est aussi présentée dans ce chapitre.

Chapter 1

Small Unilamellar Lipid Vesicles,

Annexin-A5 and Block Copolymers:

A Literature Review

This chapter is dedicated to the fundamental aspects and the literature review on the nano-structures studied in the present work, Small Unilamellar Vesicles and Block copolymer assemblies, as well as the Annexin-A5 protein and its interaction with phospholipid vesicles.

The first part is devoted to the overview of liposomes, particularly Small Unilamellar Vesicles (SUV), followed by a brief description of their preparation methods and applications proposed trough the latest years.

Afterwards, some aspects of the interaction between phospholipid vesicles and the Annexin-A5 will be described within the principal characteristics of such a very interesting protein.

Finally, the principal breakthroughs achieved in the block copolymers chemistry will be reviewed. The synthetic strategies to obtain such macromolecules and their fascinating self-assembly ability are contemplated in this chapter with emphasis to their aqueous solution properties. The recent applications of block copolymers self-assembled structures are also highlighted.

1.1. Liposomes

Liposomes, or (phospho)lipid vesicles, are self-closed colloidal particles composed from assembled lipid molecules that occur naturally and can also be prepared artificially. [5]

The liposomes nomenclature is based on the number of lipid bilayers (lamellaes) and size.[6] One can have *MLV* (Multilamellar Vesicles), formed by many almost concentric lipid bilayers with a size between 400 and 1000 nm, MVL (Multivesicular Liposomes) or unilamellar vesicles including *LUV* (Large Unilamellar Vescicles) with a diameter bigger than 50 nm and *SUV* (Small Unilamellar Vesicles) with a diameter close to 50 nm.

To prepare artificial liposomes the lipids are mixed in an organic solvent (very often chloroform), and the solvent is removed by evaporation, vacuum drying or lyophilization. The dry lipid film is then hydrated (normally in a buffer solution). Upon hydration of lipids, large multilamellar vesicles are typically formed. Their size can be reduced by extrusion, and homogenization or sonication to obtain *LUV*s and *SUV*s, respectively. Sometimes, especially to prepare LUVs, several freeze-thaw cycles are realized before extrusion or sonication to equilibrate the lipid concentration between the lamellae.[6]

At first, liposomes were used as a model to study biological membranes. Practical applications, notably in drug delivery, emerged in the 1970s.[5] Nowadays these systems are used in many fields of science, including mathematics and theoretical physics, biophysics, chemistry, colloidal science, biochemistry, biology and are applied in drug-delivery (antifungals, anticancer agents, vaccines), cosmetics (skin-care products, shampoo), diagnostics, and food chemistry.

Besides some advantages[7] (reduced accumulation by sensitive organs such as the heart and kidneys or increase uptake by target tissues), a major problem with liposomes is that they have very short lifetimes and are rapidly cleared from the blood stream mainly due to their inherent colloidal and biological instability.[8] Liposomes stability can be divided into chemical and biological stabilities, that are inter-related. The chemical stability depends on the size distribution, pH, ionic strength, while the biological stability depends on the presence of agents that interact with such structures. According to some studies, liposome's instability is due to the imposed curvature that results in thermodynamic metastability and colloidal instability causing aggregation due to ubiquitous van der Waals interaction.[9]
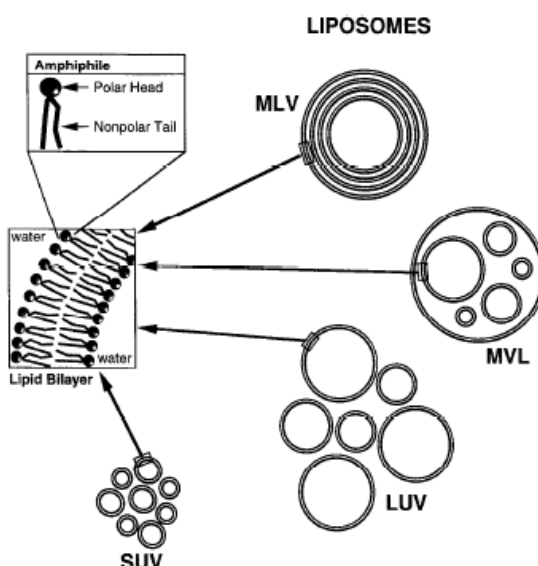

Figure 1.1. Schematich representation of different liposomes structures classified according to the number of lamella and size. *MLV* (Multilamellar Vesicles), *MVL* (Multivesicular Liposomes), *LUV* (Large Unilamellar Vesciles), and *SUV* (Small Unilamellar Vesicles).[9]

Among many techniques used to improve the colloidal and biological stability of liposomes the most promise is the coating of liposomes with inert hydrophilic polymers like PEG, for example, to obtain the so-called "stealth liposomes".[5] Such strategy prolongates liposome circulation in blood and reduced stability, reducing interactions with blood proteins.
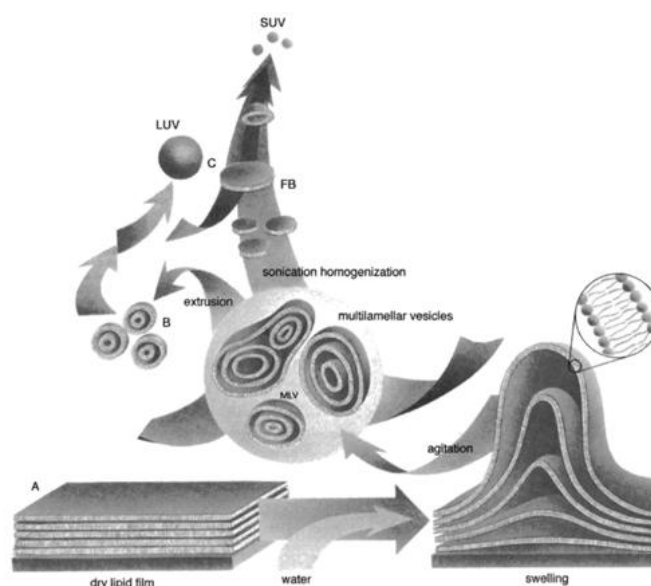

Figure 1.2. Schematic representation of *MLV (*Multilamellar Vesicles*)*, *SUV* (Small Unilamellar Vesicles), and *LUV* (Large Unilamellar Vesicles) preparation. Adapted from www.avantilipids.com.

1.2. The Annexin-A5 protein

Annexins form a subgroup of the Ca^{2+} binding proteins family. The name Annexin is derived from Greek *annex* meaning "bring/hold together" and describes the principal characteristic of such protein family: binding and possibly holding together of certain biological structures.[10] Such proteins are able to bind in a Ca^{2+}-dependent manner to negatively charged phospholipids. They contain a segment of 70 amino acid residues forming the annexin repeat (all the annexins contain 4 or 8 repeat units), consisting in a small NH_2-terminal domain and a COOH-terminal protein core (see figure 1.3). The binding between annexins and phospholipids can be reversed by removing the Ca^{2+} ions using Ca^{2+}-chelating agents.

Sopkova-de Oliveira Santos et al[11] used X-ray crystallography to study conformational changes in the Annexin-A5 in the presence of Ca^{2+}. These authors showed that the binding of calcium to carbonyl oxygens in domain III of such protein is accompanied by a large

conformational change involving surface exposure of a loop containing Trp187. Also according to the therein cited articles, it seems that this conformational change can also occur in acid pH or in the presence of high concentrations of calcium alone.

A versatile approach to study the interaction between phospholipids and the Annexin-A5 protein is through the formation of Supported Lipid Bilayers (SLBs). The formation of such structures and the characterization techniques applied has been reviewed by Richter and co-workers.[12] The deposition of model biological membranes onto solid supports allows the study of membrane processes and possible biotechnological applications (*e.g.:* biomedical devices and biofunctional materials) using surface techniques, like atomic force microscopy (AFM), surface plasmon ressonace (SPR), ellipsometry, quartz crystal microbalance (QCM-D).
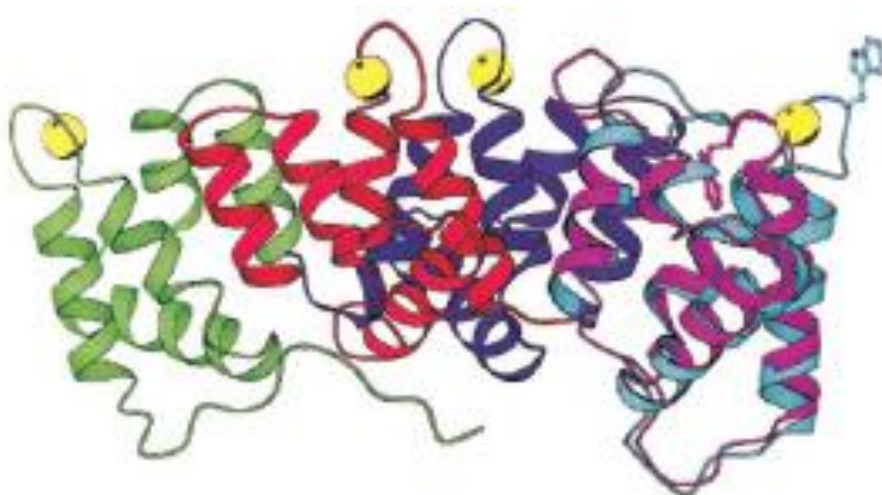

Figure 1.3. Crystal structure of human annexin-A5. Different colors represent different repeat units: repeat I in green, repeat II in blue, repeat III in red and repeat IV in violet/cyan. The NH2-terminal domain appears unstructured and extends along the concave side of the molecule (green). The high and low Ca^{2+} forms are shown in a superposition revealing the conformational change in repeat III, wich leads to the exposure of Trp-187 (violet for low and cyan for high Ca^{2+} form). Bound Ca^{2+} are represented as yellow spheres.[10]*

Some annexins participate in the regulation of the membrane organization and membrane traffic and the regulation of ion Ca^{2+} currents across membranes, others are also involved in regulation of blood coagulation, physiological stress and cancer. [10, 11]

Recently, the Annexin-A5 has been introduced as a diagnostic tool for labeling the surface of apoptotic cells due to its ability to bind to acid phospholipids [13-15]. Apoptosis, or

programmed cell death, is an important feature of normal tissue development and homeostasis (regulation of internal environment so as to maintain a stable, constant condition). Deregulation of such a program can indicate the presence of a variety of diseases, including cancer, autoimmune diseases, neurodegenerative diseases, atherosclerosis, and myocardial infarction.[15] The apoptotic cell death is accompanied by a change in plasma membrane structure with surface exposure of phosphatidylserine (PS). Exposed PS molecules can be detected by their binding to Annexin-A5. Such binding cannot occur in normal cells since the Annexin-A5 is not able to penetrate the phospholipid bilayer. [14]

1.3. Block copolymers

Block copolymers are macromolecules consisting of two or more blocks formed by different monomeric units linked together via covalent bonds. In the simplest case, a diblock copolymer consists of two different homopolymers linked end to end. The resulting material will have hybrid properties, coming from the physical characteristics of homopolymer sections, giving then numerous applications.

A very interesting class of block copolymers is the "Amphiphilic Block Copolymers". The fascinating characteristics of such macromolecules come from the opposed behavior of different chemical segments: hydrophobic versus hydrophilic. Self-assembled structures formed from these amphiphilic macromolecules, mainly micellar structures, have received increasing attention during the least years due to their potential for encapsulation of large quantities of guest molecules within their central cavity.

One of the advantages working with block copolymers, as compared with liposomes for example, is that the chemists can play with a variety of block copolymers, chemical functions and macromolecular characteristics to build up different self-assembled objects (micelles, vesicles) to the desired applications.

1.3.1. Synthesis

New developments in the synthesis technique, especially anionic and controlled free radical polymerization, has allowed the preparation of block copolymers with very well defined compositions, molecular weight and structures (controlled architectures).

Such breakthroughs in block copolymer synthesis has been broadly discussed and reviewed in the last years.[16-23] The reader is referred to the cited review articles[16, 18-21] and books[17, 22, 23] for detailed information.

In the synthesis of linear block copolymers two general reaction strategies can be applied[24]. In the first one, α or α,ω active sites are generated on a polymer chain A which then initiate the free radical, anionic or cationic polymerization of a second monomer B (Figure 1.4(a)). The second strategy, called condensation or coupling, is a reaction between chemical functional groups present at the end of different polymers (Figure 1.4(b)). The choice will depend on the polymerization mechanism, the copolymer structure, the desired molecular weight and the required dispersity.

In addition to the cited strategies, recently Taton and Gnanou[17] had reviewed other possibilities using the controlled/living polymerization (CLP) techniques, like combination of different modes of polymerization (switching from one to another) for the preparation of specific block copolymers that are not accessible from one polymerization mechanism only (Figure 1.4(c)), and one-pot initiation from dual bifunctional initiators for AB block copolymer synthesis (Figure 1.4(d)).

The classical approach represented by *route A* was used during this work to prepare amphiphilic diblock copolymers by atom transfer radical polymerization (ATRP) able to form micellar nanoparticles in water. The order of monomer addition is an essential consideration for the successful employment of this strategy. The growing chains from the polymerization of the first monomer A must be able to efficiently initiate the polymerization of the second monomer B. Another important requirement is that the conversion of the first monomer must be near quantitative in order to prepare well-segmented, structurally homogeneous macromolecules.
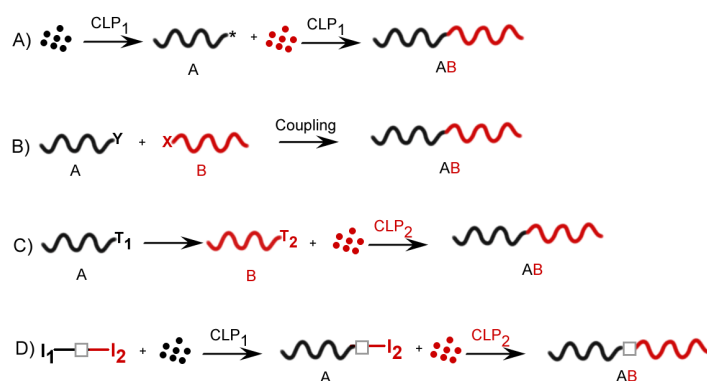
Figure 1.4. Illustration of possible routes toward the synthesis of di- or triblock copolymers, as proposed by Taton and Gnanou.[17]

Atom Transfer Radical Polymerization (ATRP)

The Atom Transfer Radical Polymerization (ATRP) has contributed enormously to the macromolecular domain,[23, 25-27] allowing the preparation of a multitude of macromolecules with controllable architecture, functionality, composition and topology, as illustrated in Figure 1.5.

This polymerization technique, a generation of controlled radical polymerization with origins on the Atom Transfer Radical Adition (ATRA) and the Transition Metal Living Radical Polymerization (TMMLRP), was described in 1995 almost simultaneously by Matyjaszewski and Sawamoto,[28, 29] and recently reviewed by Matyjaszewski and Xia[30]. The reader can use the later cited reference for better understanding on the ATRP technique.
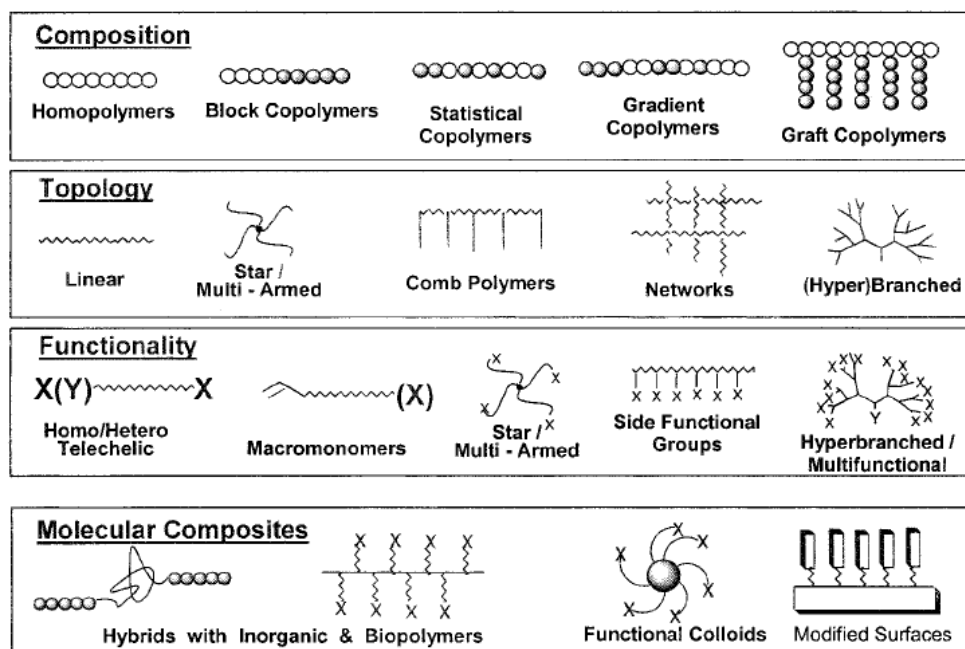

Figure 1.5. Schematic Representation of Controlled Topologies, Compositions, and Functionalities and Molecular Composites Prepared by ATRP [30]

Matyjaszewski et al.[28] reported on the ATRP of styrene at 130 ^{o}C using CuCl/2,2'-bipyridine as catalytic system. They intentionally use 1-penhylethyl chloride as the initiator to mimic the

structure of dormant extremity of the PS chain. The controlled character of this polymerization was supported by the linear dependence of the number average molar mass (M_n) with the monomer conversion. Also, pseudo first-order kinetics indicated that the concentration of the growing radical chains remained constant during the propagation and that termination was not significant, accordingly to a controlled radical polymerization (CRP). The polydispersity was relatively narrow (M_w/M_n = 1.5). The number average molar mass (M_n) of the resulting polymers could be easily controlled by the monomer/initiator ratio. Finally, a good agreement between theoretical M_n ($M_{n,theo}$) and experimental M_n ($M_{n,exp}$) values measured by GPC supported a high initiation efficiency (e.g., f = $M_{n,theo}/M_{n,exp}$ = 0.93. The synthesis of block copolymers was also reported by heating chloride end-capped PS in presence of methyl acrylate (MA) and the copper catalyst, thus yielding PS-*b*-PMA copolymer.
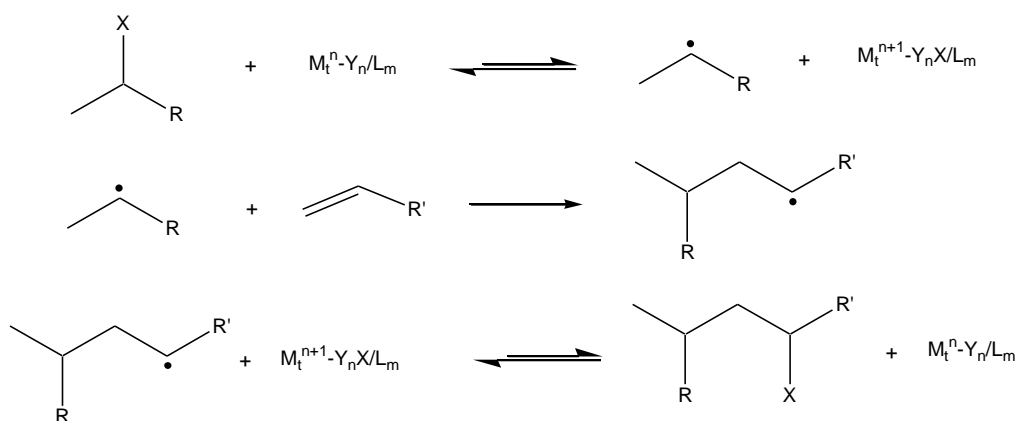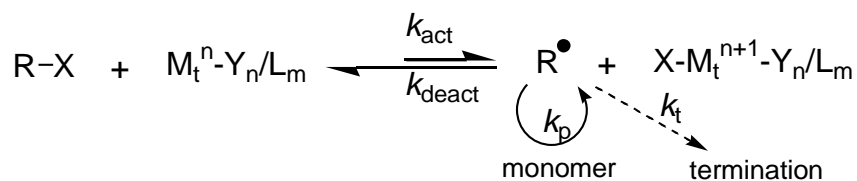

Scheme 1.1. General mechanism of ATRA.

Sawamoto[29] demonstrated that methyl methacrylate (MMA) could be polymerized using a ruthenium catalyst ($RuCl_2(PPh_3)_3$) and CCl_4 as the initiator. In that approach, the addition of an aluminum alkoxide was needed. Although its role is not clear, the authors proposed that it activated the C-Cl bound at the polymer chain end through coordination of the methyl ester group. In absence of this Lewis acid, only the mono-adduct was formed. Linear pseudo first order kinetic plots were obtained, in contrast to the dependence of $M_{n,exp}$ on the monomer conversion, while $M_{n,exp}$ was smaller than $M_{n,theo}$, suggesting that transfer reactions occurred.

The ATRP system is composed by a monomer, an initiator with transferable (pseudo)halogen, and a catalyst (composed of a transition metal species with any suitable ligand) [30]. This technique involves the radical or active species generation trough a reversible redox process catalysed by a transition metal complex (M_t^n-Y/Ligand, where Y may be another

ligand or the counterion) which undergoes a one electron oxidation with concomitant abstraction of a (pseudo) halogen atom, X, from a dormant species, R-X. This process occurs with a rate constant of activation, k_{act}, and deactivation, k_{deact}. Polymer chains grow by the addition of the intermediate radicals to monomers in a manner similar to a conventional radical polymerization, with the rate constant of propagation k_p. Termination reactions (k_t) also occur in ATRP, mainly through radical coupling and disproportionation; however, in a well-controlled ATRP, no more than a few percents of the polymer chains undergo termination. Typically no more than 5% of the total growing chains terminate during the initial, short, non-stationary stage of polymerization. This process generates oxidized metal complexes (deactivators), which behave as persistent radicals to reduce the stationary concentration of growing radicals and thereby minimize the contribution of termination at later stages.

$$R\!-\!X \;+\; M_t^{\,n}\text{-}Y_n/L_m \;\; \underset{k_{deact}}{\overset{k_{act}}{\rightleftharpoons}} \;\; R^{\bullet} \;+\; X\text{-}M_t^{\,n+1}\text{-}Y_n/L_m$$

monomer (k_p)   termination (k_t)

Scheme 1.2. General transition-metal-catalyzed ATRP mechanism, as proposed by Matyjaszewski.[30-32]

The equilibrium constant ($K_{eq} = k_{act}/k_{deact}$) determines the polymerization rate. ATRP will not occur or occur very slowly if the equilibrium constant is too small. In contrast, large equilibrium constants will lead to a large amount of termination because of a high radical concentration. This will be accompanied by a large amount of deactivating higher oxidation state metal complex, which will shift the equilibrium toward dormant species and may result in an apparently slower polymerization. Each monomer possesses its own intrinsic radical propagation rate. Thus, for a specific monomer, the concentration of propagating radicals and the rate of radical deactivation need to be adjusted to maintain polymerization control.

So far, a variety of transition metal complexes have been successfully used for ATRP. They include compounds from group VI (Mo), VII (Re), VIII (Ru, Fe), IX (Co, Rh), X (Ni, Pd) and XI (Cu), and are used almost invariably with halides and suitable ligands such as bipyridyls, aryl phosphines, aliphatic amines, able not only to facilitate solubility of the halide salts but also to modify the electronic (redox potential) and steric nature of the complexes. Typical initiators are halogenated alkanes, haloesteres, (haloalkyl)benzenes, sulfonyl halides, etc.

Using ATRP protocols, control of polymerization has been achieved for various monomers including methacrylates, acrylates, styrenes, etc., most of which are radically polymerizable conjugated monomers. This technique has also been proven to be a valuable tool for the synthesis of a variety of polymers with reactive groups (acids, hydroxyls, amines, etc.).[30, 33]This is one of the reasons to choose the ATRP for the synthesis of the block copolymers used in present work.
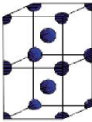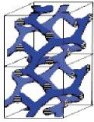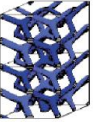
1.3.2. Phase behavior and Morphology

Dissimilar block copolymers tend to segregate into different domains due to their mutual repulsion and the extension of any domain in space is limited by the constraint imposed by the chemical connectivity of the blocks. Area minimization at the interface (the IMDS) of two blocks takes place to lower the interfacial energy. From an entropic standpoint, the molecules prefer random coil shapes but the blocks are stretched away from the IMDS to avoid unfavorable contacts. As a result of these competing effects, self-organized periodic microstructures emerge on the nanoscopic length scale. Various microdomain structures are obtained, depending on the relative volume ratio between blocks and chain architecture as well as the persistence lengths of the respective blocks.[34]

In the simplest case of non-crystalline flexible coil AB diblock copolymers, the composition of the AB diblock (i.e. the volume fraction f of block A) controls the geometry of the microdomain structure. As shown in Figure 1.6(a), for nearly symmetric diblocks ($f \sim 1/2$) a lamellar (LAM) phase occurs. For moderate compositional asymmetries, a complex bicontinuous state, known as the double gyroid (DG) phase, has been observed in which the minority blocks form domains consisting of two interweaving three fold coordinated networks. At yet higher compositional asymmetry, the minority component forms hexagonally packed cylinders (CYL) and then spheres (SPH) arranged on a body-centered cubic lattice. Eventually, as $f \rightarrow 0$ or 1, a homogeneous phase results.[35] The equilibrium morphologies of ABC triblock terpolymers are more diverse than those of AB diblock copolymers (Figure 1.6(b)). In ABC triblock terpolymers, there exist two composition variables and three interaction parameters, which make their phase behaviors much more complicated than AB diblocks having only one composition variable and one interaction parameter.[36] More extensive information regarding

morphologies of complex BCP systems including ABC triblocks and star copolymers can be found in the literature.[37]

Among many others,[38] the phase behavior of block copolymers was first described in 1980 by Bates using mean-field theory [39]. According to the cited theory, the phase behavior of diblock copolymers is dictated by the Flory-Huggins segment-segment interaction parameter,χ, the degree of polymerization, *N*, and the composition, ϕ, with the product $N\chi$ determining the degree of segmentation. In the case of $N\chi \leq 10$, the system is ruled by entropic terms, resulting in a disordered phase. If $N\chi \geq 10$, enthalpic terms dominate, causing an order-disorder transition (ODT) where the unlike segments segregate into a variety of ordered periodic microstructures.

(a)

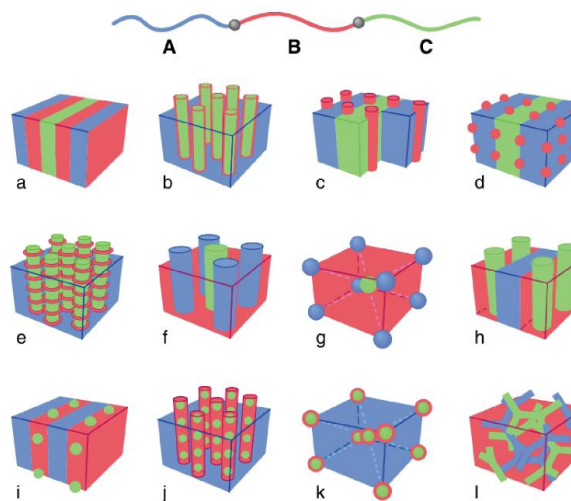| Nature of patterns	Spheres (SPH) (3D)	Cylinders (CYL) (2D)	Double gyroid (DG) (3D)	Double diamond (DD) (3D)	Lamellae (LAM) (1D)
Space group	$Im\bar{3}m$	p6mm	$Ia\bar{3}d$	$Pn\bar{3}m$	pm
Blue domains: A block					
Volume fraction of A block	0-21%	21-33%	33-37%		37-50%

(b)

Figure 1.6. Schematic phase diagram showing the various classical block copolymers morphologies(a) and Schematic of morphologies for linear ABC triblock copolymer(b). [36]

More recently, Matsen[40] used the self-consistent field theory (SCFT) to elucidate the phase behavior of binary triblock copolymer (ABA). Including higher harmonics into his computation, the author was able to bridge the gap between diblock and symmetrically composed triblock copolymers introducing an asymmetric parameter, τ, related to the number of segments of the shorter with that of the longer block.
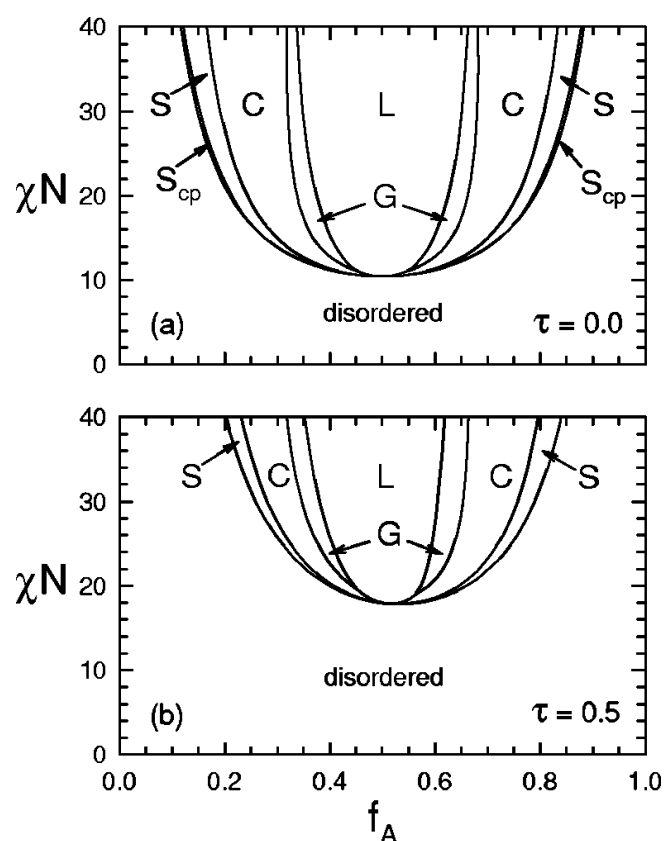

Figure 1.7. Mean-field phase diagrams for melts of *AB* diblock copolymer (a) and symmetric *ABA* triblock copolymer (b) plotted in terms of segregation χN and composition f_A calculated with SCFT.[40]

1.3.3. Self-assembly in aqueous medium

The self-assemble ability of amphiphilic block copolymers in selective solvents (*i.e.*, solvents thermodynamically good for one block and poor for the other) is largely described in the literature, and constitutes a hot research topic in modern polymer science.[4, 24, 38, 41-47]

In aqueous solutions, amphiphilic molecules orientate themselves so that the hydrophobic blocks are removed from the aqueous environment in order to achieve a state of minimum

free energy. As the concentration of amphiphile in solution is increased, the free energy of the system begins to rise due to unfavourable interactions between water molecules and the hydrophobic region of the amphiphile resulting in structuration of the surrounding water and a subsequent decrease in entropy. At a specific and narrow concentration range of amphiphile in solution, termed the critical micelle concentration (CMC) or also the critical association concentration (CAC), several amphiphiles will self-assemble into colloidal-sized particles (Figure. 1.8). If the amphiphiles concentration in solution remains above the CMC, micelles are thermodynamically stabilized against disassembly. Upon dilution above the CMC, micelles will disassemble with a rate being largely dependent on the structure of the amphiphiles and the interactions between the chains.[45] The micelle system may still be kinetically stable and survive at least for some period or time, if *i*) the core is large, *ii*) the core material is below the T_g (i.e., in a glassy state) or crystalline, and *iii*) the $\chi_{,PolymerCore\text{-}Solvent}$ parameter associated with the interaction between the hydrophobic core-forming block and the external selective solvent is high.
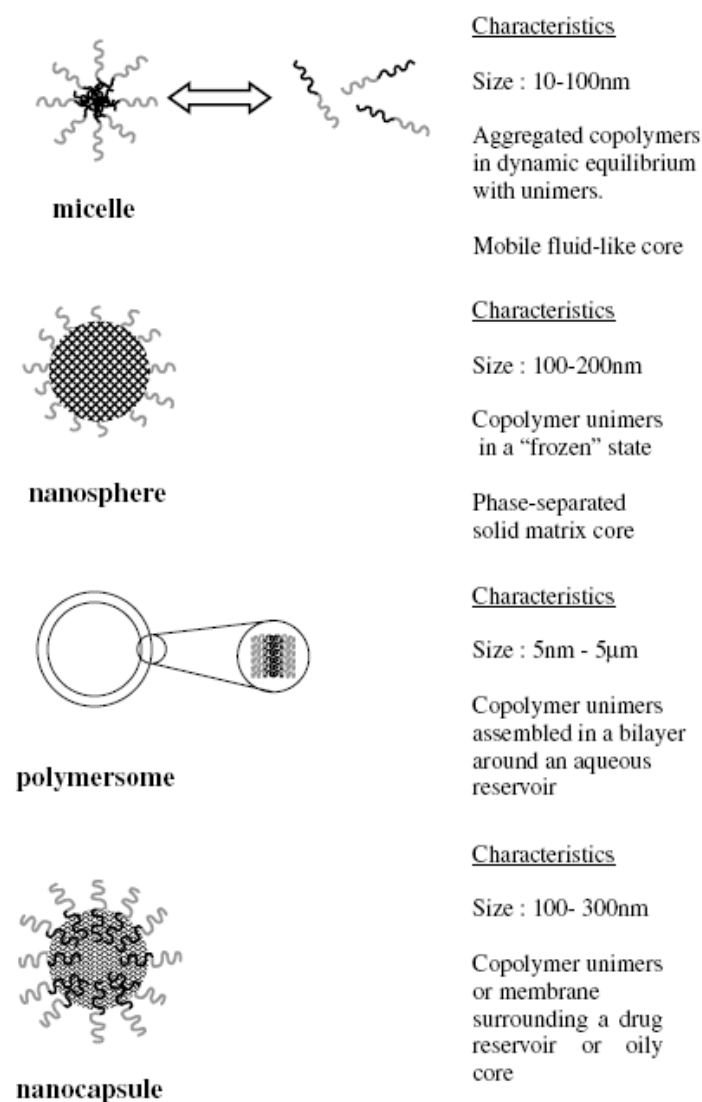
Characteristics

Size : 10-100nm

Aggregated copolymers in dynamic equilibrium with unimers.

Mobile fluid-like core

Characteristics

Size : 100-200nm

Copolymer unimers in a "frozen" state

Phase-separated solid matrix core

Characteristics

Size : 5nm - 5µm

Copolymer unimers assembled in a bilayer around an aqueous reservoir

Characteristics

Size : 100- 300nm

Copolymer unimers or membrane surrounding a drug reservoir or oily core

Figure 1.8. Nanoparticles formed by amphiphilic block copolymers and their general characteristics. Adapted from the work published by Letchford and co-workers.[46]

Different factors can affect the formation of amphiphilic block copolymers: the copolymer composition factors including block length composition and molecular geometry and the preparation methods. Studies published by Riley et al. and Heald et al. using MePEG-b-PDLLA copolymers with a range of PDLLA molecular weights and a fixed MePEG molecular weight of 5000 g/mol showed that if the PDLLA molecular weight was relatively low (2000–30,000 g/mol), the hydrodynamic radius (RH) of the resulting particles was independent of the concentration of the polymer used during preparation and the polydispersity index was low, characteristic of block copolymer micelles.[48, 49] It was determined that the R_H and aggregation

number (Nagg) of nanoparticles are highly dependent on the length of the constituent blocks. Power laws have been developed to express the dependence of the R_H and N_{agg} of nanoparticles on the hydrophobic and hydrophilic block lengths, designated N_A and N_B, respectively.[50-52] In the case of star micelles in which N_B>>N_A (Figure 1.9(a)), the scaling relationships were found to be:

$$R_H \propto N_A^{4/25} N_B^{3/5}$$ (eq. 1.1)

and

$$N_{agg} \propto N_A^{4/5}$$ (eq. 1.2)

or for strongly segregated blocks

$$N_{agg} \propto N_A^2$$ (eq. 1.3)

For the other extreme, crew cut micelle-like aggregates in which N_B<<N_A (Figure 1.9(b)) the scaling relationships were found to be:

$$R_H \propto N_A^{2/3}$$ (eq. 1.4)
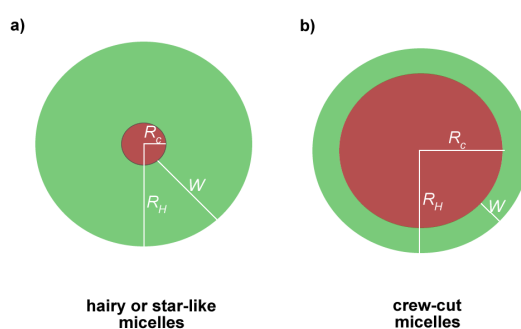
and

$$N_{agg} \sim N_A$$ (eq. 1.5)

Figure 1.9. Schematic representation of hairy or star-like (a) and crew-cut (b) micelles.

Preparation Techniques

The following preparation methods have been largely applied: direct dissolution, [24, 45, 53-55] indirect dissolution method (also called dialysis method) [24, 56-58], stimuli-induced self-assembling,[59-61] solvent casting/film re-hydratation[62, 63] and emulsion method[64]. The choice of the approach to use depends mostly on the copolymer solubility in the medium wherein the

assemblies are to be formed. Whenever the resulting assemblies are to exert a given function in a system, the choice of the method must consider the constraints of the latter.

In the present work the two methods applied are the direct and the indirect dissolution method. In the first technique, a solid sample of the copolymer is directly dissolved in a selective solvent; the micellar solution is left to anneal by standing and/or the annealing process is made by thermal treatment, eventually under ultrasonic agitation. In a second technique the copolymer is dissolved molecularly in a common solvent e.g. that is 'good' for both blocks, and then the conditions such as temperature or composition of the solvent, are changed in the way that requires formation of micelles. This is commonly achieved by adding gradually a selective precipitant of one of the blocks, eventually followed by stripping the common solvent. An alternative that is often recommended is the dialysis technique by which the common solvent is gradually replaced by the selective solvent. The reader is referred to the above cited works for more details on the preparation methods.

1.3.4. *Polyelectrolyte block copolymer micelles*

Polyelectrolyte block copolymer micelles originate from the self-assembly of macromolecular chains having, in the simplest AB-type architecture, a sequence of N_A hydrophobic monomers covalently linked to a sequence of N_B charged hydrophilic monomers with an overall composition $f = N_A/N$, where $N = N_A + N_B$. In aqueous environment, the micellar structure comprises a hydrophobic core made from A-blocks segregated from the aqueous exterior, and surrounded by a charged hydrophilic shell constituted of B-blocks. When the polyelectrolyte chains are densely tethered to the micelle core surface, they represent the so-called spherical polyelectrolyte brushes (SPB).[65, 66] With characteristically complex equilibrium of non-covalent forces (electrostatic, hydrogen bonding, van der Waals and hydrophobic interactions), SPBs are of great interest in academic research and commercial applications (e.g.: surfactants, emulsifiers, flocculants, colloids, rheology modifiers, associative thickeners).[65, 67-70]

The light, X-ray and neutron scattering behavior of charged linear chains, stars and block copolymer micelles has been the subject of intense research in recent years, and certain features are now reasonably well-established.[59, 71] A good summary of the current knowledge

of polyelectrolyte solutions with extensive references is given by Förster and Schmidt.[71] Among other parameters such as the solution pH and the degree of dissociation, the ionic strength plays a decisive role on the dimensions, and static and dynamic properties of these systems.[59, 66, 71-77] For instance, the variation of the brush thickness in a SPB (i.e., the corona width in the case of core-corona micelles) with added salt concentration or grafting density depends on whether the added salt concentration (C_s) is higher or lower than the intrinsic concentration of counter-ions in the brush ($C_{s,int}$). The two regimes are usually called "salted brush" ($C_s > C_{s,int}$) and "osmotic brush" ($C_s < C_{s,int}$), respectively.[69, 75] The presence of charges on polymer chains leads to their expansion with respect to the equivalent neutral counterparts (or highly screened equivalent polyelectrolyte chains), and the lowering in the ionic strength also results in the expansion of polyelectrolyte coils. As the ionic strength decreases, the repulsion between polyelectrolyte chains increases, leading to changes in the second virial coefficient, A_2, and a decrease in the scattering intensity due to osmotic pressure.[59, 65, 76, 77] A feature of polyelectrolytes at concentrations above the overlap concentration (c^*) is the appearance of a scattering peak (or correlation peak) that is frequently observed in x-ray and neutron experiments, while seldom detected using visible light.[76, 77]

Synthetic polyelectrolyte block copolymer micelles having poly(acrylic acid) (PAA), poly(methacrylic acid) (PMA) or poly(styrene sulfonic acid) (PSS) as corona-forming blocks are the most studied SPB systems. They can be distinguished between two classes: quenched (strongly dissociating chains such as PSS) and annealed (weak polyelectrolyte chains such as PAA and PMA) SPBs.[65, 69, 71] In the latter case, the number of charges along the hydrophilic segment depends directly on the local pH, which is affected by both the pH and the ionic strength in the bulk of the solution.

1.4. Polymer-Protein Systems

Systems based on polymer and proteins linked together are particularly suited for biological application and they may provide an interesting new bridge between the world of synthetic polymers and biological systems. This recent research topic emerged as an alternative in the use of polymers nanostructures in drug delivery systems, as an option for the target and biocompatible requirement.

One of the most studied strategies in this field is the use of biotin-streptavidin complex. [78-81] Broz et al.[78] have described the use of highly stable and biocompatible synthetic ABA copolymer vesicles (poly(2-methyloxazoline)–b-poly(dimethylsiloxane)–b-poly(2-methyloxazoline) as a delivery system, whereas activated macrophages and their scavenger receptor A1 were a model target. It was possible to make vesicles targeting the cells after they have been functionalized with the oligonucleotide poly(guanylic acid) (poly-G), which is a specific ligand for the SRA1 receptor. Linking the ligand to vesicle surfaces was accomplished via a biotin-streptavidin complex, Figure 1.10. Further loading of the nanocontainers with fluorescent labels allowed the microscopic observation of the binding and uptake of the vesicles by the cells. The major result from this study was achieving high receptor specificity of vesicle uptake. In addition, the absence of unspecific binding showed that uncontrolled uptake of the carrier by cells can be overcome using specific nanocontainer building blocks, exhibiting very low polymer–protein interaction.
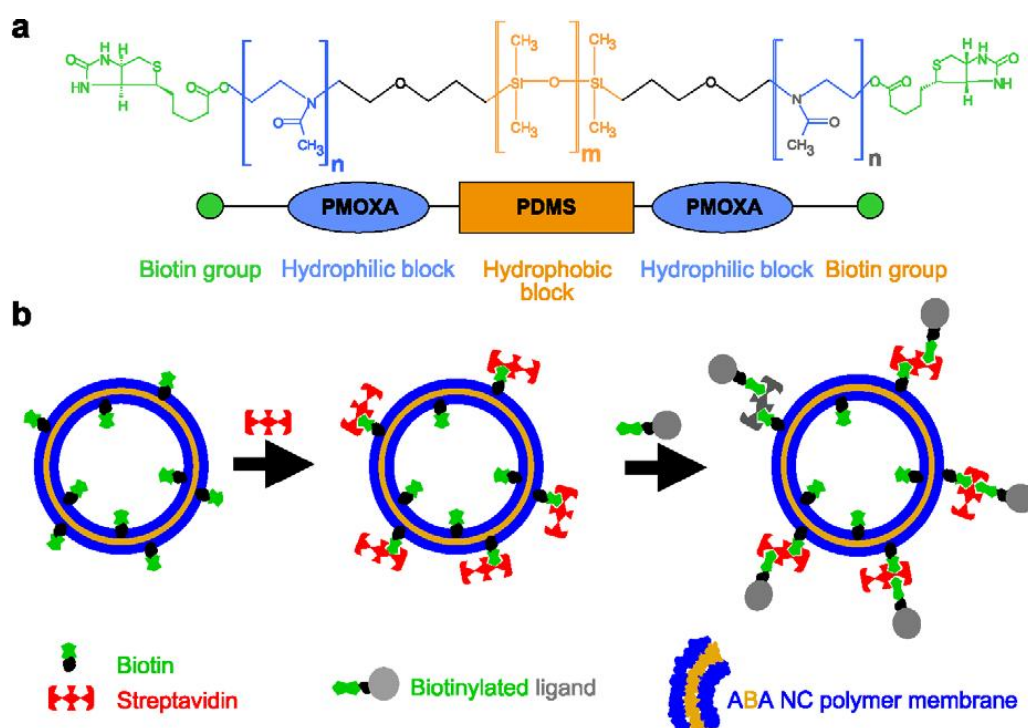
Figure 1.10. Biotin-functionalized (poly(2-methyloxazoline)–b-poly(dimethylsiloxane)–b-poly(2-methyloxazoline) triblock copolymers (a) and their self-assembly to form nanocontainers having biotinylated targeting ligands attached by using streptavidin as a coupling agent (b). Adapted from Broz et al.[78]

The interaction of proteins with polyelectrolytes is another way to obtain mixed polymer-biological systems.[67 82, 83] Witteman and Ballauff [84] have recently described the adsorption of bovine serum albumin (BSA) on spherical polyeletrolyte brushes (SPB) consisting of a solid polystyrene core onto which linear polyelectrolyte chains (poly(acrylic acid) (PAA)) are grafted. The authors have observed strong interactions even though both, the SPB and the BSA, are negatively charged in solution. This interaction depends on the salt concentration (strongest at low salt concentration and decreasing drastically with increasing amounts of added salt with no adsorption at 0.1 M) and, thus can be reversible.

The bovine serum albumin is a model system largely applied in the study of polymer-protein systems [82, 85, 86] but other proteins, such as collagen, fibronectin, myoglobulin, albumin, fibrinogen have also been studied. [87, 88]

Chapter2

Characterization Methods

2.1. Gel permeation chromatography (GPC)

Gel Permeation Chromatography, (GPC), also known as Size Exclusion Chromatography, (SEC) is one of the most useful techniques to characterize synthetic polymers as the molecular weight and the molecular weight distribution are highly relevant to their properties (mechanical and chemical resistance and biodegradability).[89]

The sample must be soluble in an appropriate solvent (a concentration of 0.10% (w/v) for a polymer of molecular weight ~100,000 is typical) and then it is introduced via an injection mechanism onto a set of columns (packed with finely divided solid particles containing pores), which act as a molecular filtration system, to finally reach the detector (the most common is the refractive index (*RI*) and/or the ultraviolet (*UV*)).[90] The GPC system configuration is shown in Figure 2.1. The mechanism of separation in SEC is based on the size of the macromolecules in solution (hydrodynamic volume). There should be no interaction with the column packing, (adsorption, partition, etc.).[91] The larger size molecules will not enter into the smaller pores while the smaller molecules will fit into most of the pores, and will be retained longer.
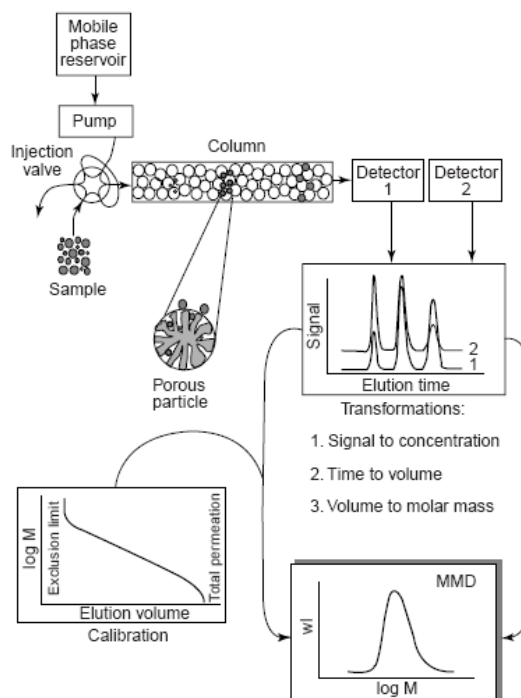
Figure 2.1. Schematic representation of SEC.[90]

Depending on how the polymerization was carried out, the distribution of the chain molecular weights can be narrow, or quite broad. The molecular weight averages across this distribution can be obtained by statistics. There is a height, (H_i, also represented as concentration, C_i) a retention time, and a molecular weight, (M_i), attributed to each slice. The molecular weight is obtained from a calibration curve performed using fractions of a particular polymer which have been well characterized in terms of molecular weights. By a summation it is possible to obtain the various molecular weight averages that describe the polymer molecular weight distribution.[92] The polydispersity index (*PD)* determined is the ratio between the weight average and the number average molecular weights (M_w/M_n) and is called the polydispersity, or sometimes simply, the dispersity of the polymer. This summation is just a simple way to obtain these four molecular weight statistical moments and describe the molecular weight distribution.

$$\bar{M}_X = \frac{\Sigma C_i M_i^n}{\Sigma C_i M_i^{n-1}}$$

C_i

n=0 (Mn)
n=1 (Mw)
n=2 (Mz)
n=3 (Mz+1)

PD = Mw/Mn

Retention Time (or Volume)
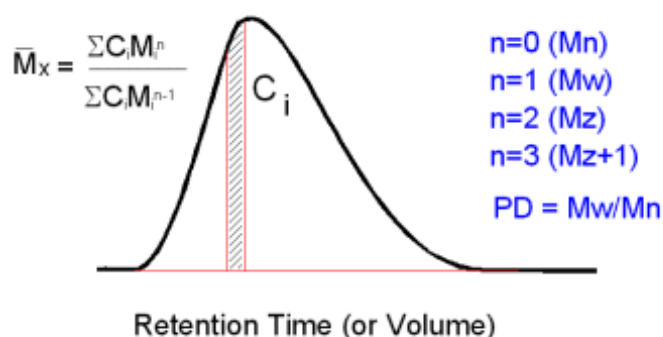
Figure 2.2. Calculation of molecular weight average.

2.2. Scattering Techniques

Many of the current techniques applied in the study of the structure and dynamics of matter make use of electromagnetic radiations. It is possible to find the application of such probe in the determination of the structure of complex macromolecules through largely applied techniques, such as IR, UV, X-Ray, Raman spectroscopy, etc.

When the radiation impinges on a sample, the electric field of the radiation induces an oscillating polarization of the electrons in the molecules. The molecules then serve as secondary sources of radiation and subsequently scatter the radiation. The frequency shifts,

the angular distribution, the polarization, and the intensity of the scattered radiation are determined by the size, shape, and molecular interactions in the scattering material.[93]

It is important to notice that radiation will be scattered by molecules in solution if the molecule has a polarizability α (thought as a difference in the refractive index between the particles and the solvent) different form its surroundings. In a perfect homogeneous medium the incident radiation will pass by and we will find the recombinant radiation with no scatter. In a non-homogeneous medium the radiation will be scattered in all directions. Even pure solvents can scatter the incident radiation due to Brownian motion. Macromolecular solutions are non-homogenous mediums were the mobility and diffusion of macromolecules can cause local changes in the concentration. More concentrated areas will scatter the incident radiation more strongly as a consequence of changes in the dielectric constant.

Depending to the incident radiation, three main different scattering techniques can be distinguished: light, X-ray, and neutron scattering. Light and X-rays are scattered by electrons present in the sample, while neutrons are scattered by the nucleus of the atoms. These techniques are also different concerning the wavelength of the incident radiation:

Light Scattering: 4000 Å $< \lambda_i <$ 7000 Å

Neutron Scattering: 1 Å $< \lambda_i <$ 20 Å

X-ray Scattering: : 0.2 Å $< \lambda_i <$ 2 Å

The typical setup used in a scattering experiment is represented in figure 2.3. An incident monochromatic beam with a wavelength λ_i and wavevector $\vec{k}_i$ impinges on the scattering medium and the scattered radiation (λ_{sc}, $\vec{k}_{sc}$) is analyzed as a function of the observation or scattering angle θ.
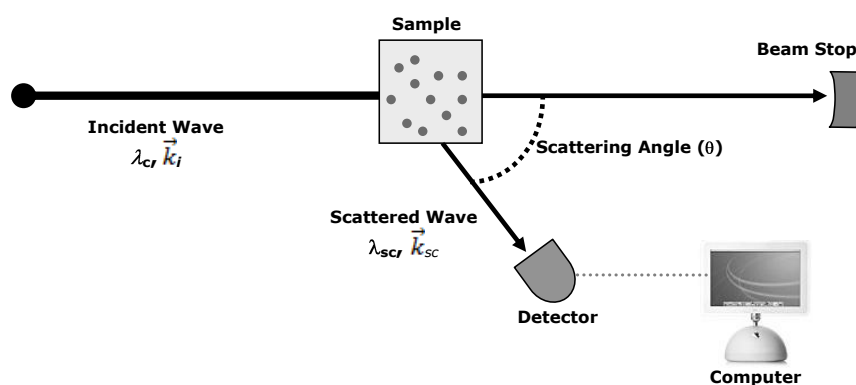

Figure 2.3. Typical setup used in a scattering experiment.

The incident and the scattered wavevector modulus, $\vec{k}_I$ and $\vec{k}_{sc}$ respectively, are defined by the relations bellow:

$$\left|\vec{k_\iota}\right| = \frac{2\pi n}{\lambda_i} \qquad \text{and} \qquad \left|\vec{k_{sc}}\right| = \frac{2\pi n}{\lambda_{sc}} \qquad \text{(eq. 2.1)}$$

with λ_i and λ_{sc} being, respectively, the incident and the scattered wavelength in vacuum, and *n* the refractive index of the medium. The scattered intensity in an arbitrary direction will be defined by scattering vector $\vec{q}$:

$$\vec{q} = \vec{k_\iota} - \vec{k_{sc}} \qquad \text{(eq. 2.2)}$$

For inelastic scattering (without energy transfer) the incident and the scattered wavelength values are the same, and for consequence the wave vector modulus have also the same values:

$$\vec{k_\iota} = \vec{k_{sc}} \qquad \text{(eq. 2.3)}$$

By using the equations 2.1, 2.2, and 2.3 the scattering vector $\vec{q}$ can be written as a function of the observation or scattering angle, θ:

$$|\vec{q}| = \frac{4\pi n}{\lambda_l}\sin\frac{\theta}{2} \qquad \text{(eq. 2.4)}$$

The later equation shows that the scattering vector $\vec{q}$ is proportional to $1/\lambda$, and therefore we can relate the different scattering techniques with the scattering vector:

Light Scattering: 5×10^{-5} Å^{-1} < q < 3×10^{-3} Å^{-1}

X-ray and Neutron Scattering: 2×10^{-4} Å^{-1} < q < 5×10^{-1} Å^{-1}

By combining the three different techniques we can have access to a large range of *q* values giving enough data to characterize macromolecules at different scales. The most important parameter in scattering techniques is the contrast between the sample and the environment (solvent). In each of the three techniques described the contrast has different origin as described in table 2.1.

Table 2.1.Contrast origin as a function of the scattering techniques.

Scattering Technique	Contrast Origin
Light	Difference of refractive index
X-ray	Difference of electronic density
Neutrons	Difference in the coherent length between the atoms

The measured scattering intensity can be described by the equation bellow:

$$I_{theo}(q) = Constrast \times P(q) \times S(q) \qquad \text{(eq. 2.5)}$$

with *P*(*q*) being the Form Factor of the particles and *S*(*q*) the Structure Factor. For dilute systems the structure factor can be considered equal to 1, and thus the scattering intensity will be a function of the form factor. The latter case is illustrated in Figure 2.4, where the Form Factor is represented as a function of the *q* for the different scattering techniques.
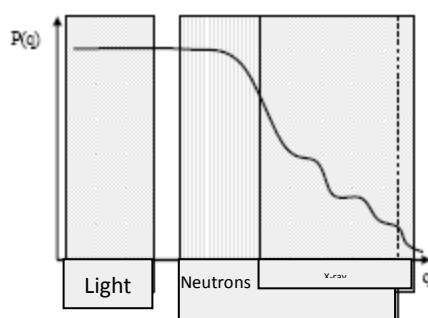
Figure 2.4. Schematic representation of the Form factor *P*(*q*) as a function of the wave vector *q* for different scattering techniques.[53]

2.2.1. Light Scattering

In LS experiments, a monochromatic beam impinges on a sample and is scattered into a detector placed at an angle θ with respect to the transmitted beam. The intersection between the incident and the scattered beams defines a volume *V*, called scattering volume or illuminated volume.[93] All the elements (solvent and particles such as micelles, cylinders, vesicles, etc) within such a space will scatter the light in all directions at a given intensity, which depends on their polarizability. In other words, light scattering only occurs in media having an inhomogeneous refractive index. This techniques can be applied to diverse systems as food, liquid crystals, gels, solutions of macromolecules, electrolyte solutions, membrane vesicles, proteins, etc. [93, 94]

Depending on the data treatment applied to the scattered intensity arriving at the detector, different information can be obtained. Whilst static light scattering (SLS) measures the time-average intensity of scattered light arriving at the detector, in dynamic light scattering (DLS) the information comes from the fluctuations of the scattered light intensity as a function of time.

Static Light Scattering

As mentioned before the static light scattering (SLS) measurements make use of the time-average intensity of scattered light to determine the molecular weight, form, size, and the Second Virial Coefficient A_2 (related to the particle solvent interactions) through the Form Factor and the Structure Factor of the particles in solution. For macromolecules, colloids, and aggregates, the light scattered for different dipoles in the same particle will form constructive and destructive interferences and, therefore, the scattering intensity will depend on the particle form and the scattering angle θ.

The mathematic relationship below was proposed by Debye for a non-ideal solution having a concentration C without interactions between particles:

$$\frac{KC}{\Delta R_\theta} = \frac{1}{M_w P(q)} + 2A_2 C \qquad \text{(eq. 2.6)}$$

where M_w is the weight average molecular weight, A_2 is the second Virial coefficient, $P(q)$ is the form factor of the particle, and K is the scattering constant defined as:

$$K = \frac{4\pi^2 n^2}{\lambda_i^4 N_A} \left(\frac{dn}{dc}\right)^2 \qquad \text{(eq. 2.7)}$$

with n being the refractive index of the medium, N_A the Avogrado number, and dn/dc the increase in the refractive index with the concentration. In practical, the Rayleigh factor ΔR_θ is obtained indirectly using the relation bellow:

$$\Delta R_\theta = \frac{I - I_{solvent}}{I_{standard}} \left(\frac{n_{solvent}}{n_{standard}}\right)^2 R_{standard} \qquad \text{(eq. 2.8)}$$

where I, $I_{solvent}$, and $I_{standard}$ are respectively the measured intensity for the sample, the solvent, and the standard, $n_{solvent}$ and $n_{standard}$ respectively the refractive index for the solvent and for the standard, and $R_{standard}$ the Rayleigh factor for the standard. In the present work the standard used was toluene with an already know Rayleigh factor equal to 1.3522 x 10^{-5} cm^{-1} at λ_l = 632.8 nm. In the Guinier regime (qR_g << 1) the form factor P(q) is related to the gyration radius R_g by the equation:

$$P(q)_{q\to 0} \approx 1 - \frac{q^2}{3}\langle R_g^2 \rangle \qquad \text{(eq. 2.9)}$$

In a classic static light scattering experiment, the scattering intensity is measured at different scattering angles θ for solutions containing different sample concentrations. Usually the results are assembled in a Zimm graph where $KC/\Delta R_\theta$ are plotted as a function of C and q. This method can be applied for dilute systems with particles smaller them 200 nm, and allow

the calculation of M_w, R_g, and A_2 through a double extrapolation to 0 ($C = 0$ and $q = 0$). The second virial coefficient A_2 is related to the thermodynamics properties of the solution, being negative for a bad solvent, positive for a good solvent, and zero for a θ solvent. The extrapolation to $\theta = 0$ and $q = 0$, give $2A_2$ and $\langle R_g^2 \rangle / 3M_w$, respectively. In both cases the extrapolation lines at the origin (x = 0) gives M_w. The Zimm plot is illustrated in Figure 2.5.
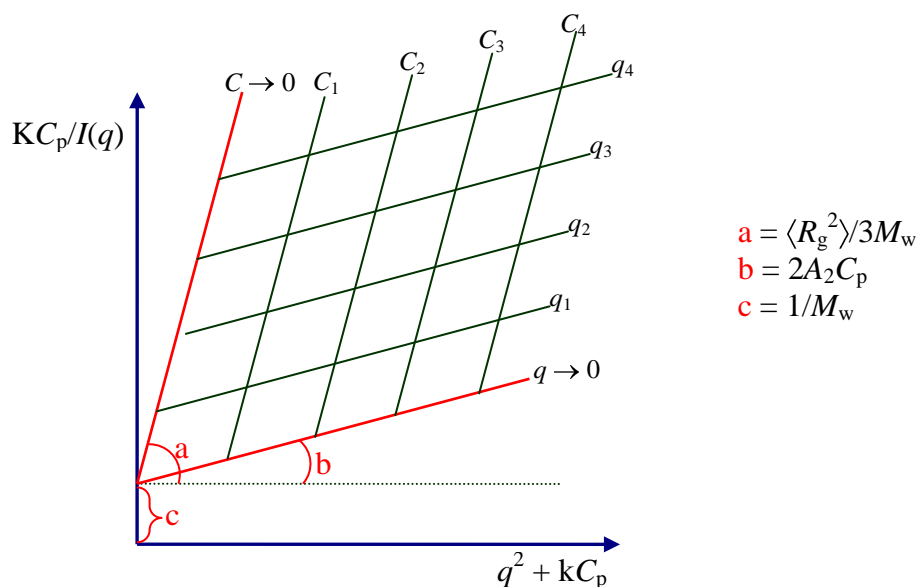
Figure 2.5. Typical Zimm plot showing the determination of M_w, R_g and A_2 values, as indicated.

Dynamic Light Scattering (DLS)

The foundation of Dynamic light scattering (DLS) is based on the scattering of light by moving particles.[94] The experiment involves the measurement of the very tiny Doppler shifts in the scattered light due to the presence of this motion. The principle of DLS is shown in Figure 2.6. On the left, the signal detected at a given observation scale (q-value) is shown. The perpetual particle motion (Brownian motion or "random walk") causes statistic fluctuations in $I(q)$ as a function of time. Certainly, such fluctuations carry very important information about the dynamics of the scattering particles, which is ultimately defined by the properties of the latter such as size, shape, molecular interactions, repulsions, etc.[22, 93, 95] The detailed analysis of these fluctuations with the aid of electrodynamics and theory of time dependent statistical mechanics, is at the origin of DLS techniques.[93] The fluctuation pattern is firstly transferred into an intensity correlation function, using the following scheme: the time-dependent scattered

intensity is multiplied with itself shifted by a distance τ in time, and these products are averaged over the total measurement time.
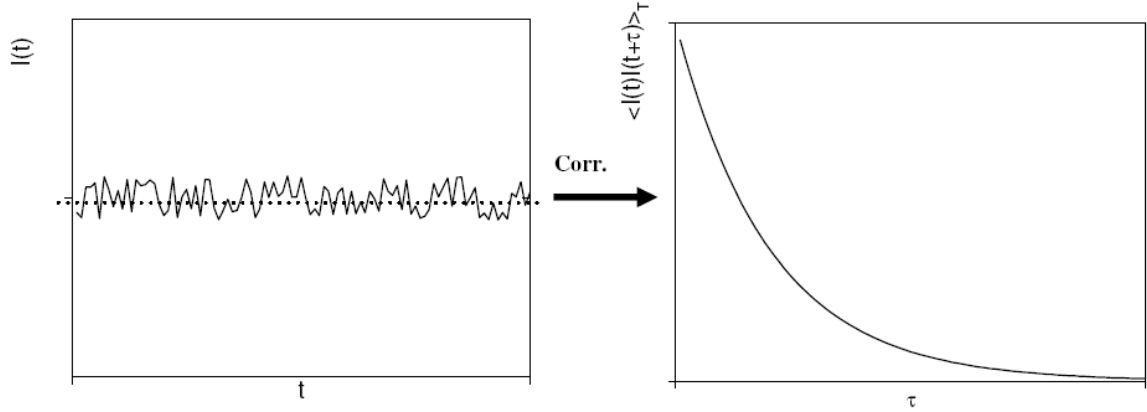
Figure 2.6. Principle of a DLS measurement.

The auto-correlation function can be defines as

$$g^2(q,t) = \frac{\langle I(q,0)I(q,t)\rangle}{\langle I(q,t)\rangle^2}$$

(eq. 2.10)

where *t* is the time. Through this relationship, it is possible to determine the variations in the scattered light intensity at a given observation scale (*q*-value) at two different moments (*I(q,0)* and *I(q,t)*). It is easy to conclude from eqn. 2.10 that when the signal at an instant *t* is compared to itself, the correlation is perfect and $g^2(q,t)$ = 1. Inversely, $g^2(q,t)$ = 0 when no correlation exist; i.e., the particle "lost" the information regarding its initial position due to the random walk. Assuming a Gaussian distribution of the electrical field, one can use the Siegert approach to obtain a relation between the auto-correlation functions of the scattered intensity $g^2(q,t)$ and the scattered electric field $g^1(q,t)$, which corresponds to the inverse Laplace transformation of the relaxation times. As a consequence, the relaxation times for a given *q*-value can be obtained from information contained in $g^2(q,t)$ function.

$$g^2(q,t) = 1 + \left| g^1(q,t) \right|^2$$

(eq. 2.11)

However, different methods apply to the analysis of the auto-correlation functions. In the present work, the CONTIN analysis[96] was used in most of the cases, while cumulants analysis was applied to estimate the polydispersity of the particles.

In the cumulants method,[97] the first order electric field correlation function of laser light scattered by polydisperse solutions of macromolecules is written as a sum or distribution of

exponentials (eqn. 2.12), with decay rates proportional to the diffusion coefficients of the solute molecules. The coefficients Γ_n are the so-called cumulants. For an ideal solution containing monodisperse scattering particles, the development of eqn. 2.12 stops at Γ_1 (or simply Γ). In the case of a polydisperse systems, though, the first cumulant Γ corresponds to an average relaxation time, while the second cumulant μ_2 is related to the distribution of the relaxation times, and thus to the extent of polydispersity index (PDI = μ_2/Γ^2).

$$\ln(g^1(q,t)) = \ln(A) - \Gamma t + \mu_2 \frac{t^2}{2} + \ldots \qquad \text{(eq. 2.12)}$$

A more powerful method, which has become the standard in analyzing DLS data, uses mathematical algorithms to perform an inverse Laplace transform on the data (described by eqn. 2.13) to obtain the distribution function of relaxation times $A(\Gamma)$.[98] In eq. 2.13, $A(\Gamma)d\Gamma$ is the fraction of the correlation function decaying with reciprocal relaxation time between Γ and $\Gamma + d\Gamma$. To find $A(\Gamma)$ from $g^1(q,t)$, which is the Laplace transformation of the former, is a non-simple problem.[98] In fact, mathematical techniques for performing such transformations known as regularization techniques were developed, and applied to the analysis of DLS by Provencher,[96] who wrote the CONTIN program.

$$g^1(q,t) = \int_0^\infty A(\Gamma)e^{-\Gamma t}dt \qquad \text{(eq. 2.13)}$$

The CONTIN routine is probably the most interesting approach to fit auto-correlation functions recorded from solutions of macromolecules and their self-assemblies.[93, 95, 98] It allows the analysis of multi-modal distribution of scattering particles, within limitations in terms of the separation of $A(\Gamma)$ peaks, which should be about a factor of five or more as, experienced during this work.

The relaxation frequency, Γ ($\Gamma = \tau^{-1}$) depends generally on the scattering angle, and in the case of a diffusive particle, this frequency is q^2-dependent.[95] The apparent diffusion coefficient (D_{app}) at a given copolymer concentration (C_p) is calculated from

$$\left.\frac{\Gamma}{q^2}\right|_{q\to 0} = D_{app} \qquad \text{(eq. 2.14)}$$

The hydrodynamic radius (R_H) (or diameter, $2R_H$) is then calculated from the Stokes-Einstein relation when assuming a spherical shape

$$R_H = \frac{k_B T}{6\pi\eta\Gamma}q^2 = \frac{k_B T}{6\pi\eta D_{app}} \qquad \text{(eq. 2.15)}$$

where k_B is Boltzmann constant, T is the temperature of the sample, and η is the viscosity of the medium.

Combining SLS and DLS experiments

In the case of block copolymer micelles, however, one can have access to the inner structure not only via measurements using large instruments (SANS and SAXS), but also via a rather simple combination of results from SLS and DLS experiments. The following physical chemical parameters can be determined using the approach described below:

- Micelle molar mass ($M_{w,mic}$)   SLS
- Micelle aggregation number (N_{agg})   SLS
- Radius of gyration (R_g)   SLS
- Interparticle interactions (A_2)   SLS
- Hydrodynamic radius (R_H)   DLS
- Corona thickness (W)   SLS + DLS
- Core radius (R_c)   SLS + DLS
- Compactness of the core   ($V_{monomer}$)   SLS + DLS

The N_{agg} is calculated using eqn. 2.16, where $M_{w,mic}$ is the micelle molar mass determined by SLS, and $M_{w,unimers}$ is the molar mass of the respective individual block copolymer chains.[99]

$$N_{agg} = \frac{M_{w,mic}}{M_{w,unimers}}$$

(eq. 2.16)

The R_c can be derived from eqn. 2.17, where N_A is the Avogadro number, $wt_{hydrophobic}$ is the weight fraction of hydrophobic block in the copolymer chain, $d_{hydrophobic}$ is its solid-state density, and $\Phi_{hydrophobic}$ is its volume fraction in the micelle core, which was assumed to be equal to unity (*i.e.* all the hydrophobic segments chains are located within the micelle core).[99] Thus the volume occupied by a single monomer unit inside the micelle core ($V_{monomer}$) can be estimated from eqn. 2.17 on the basis of R_c-values, where $DP_{hydrophobic}$ is the mean degree of polymerization of the hydrophobic block.

$$R_c = \left(\frac{3 M_{w,mic} wt_{hydrophobic}}{4\pi N_A d_{hydrophobic} \Phi_{hydrophobic}} \right)^{1/3}$$

(eq. 2.17)

$$V_{monomer} = \frac{4\pi R_c^3}{3N_{agg}DP_{hydrophobic}}$$ (eq. 2.18)

The corona width (*W*) is then calculated from the following relation

$$W = R_H - R_c$$ (eq. 2.19)

The R_g/R_H ratio is often useful to characterize and block copolymer self-assembly with respect to its morphology.[100, 101] The theoretical value of R_g/R_H for a homogenous hard sphere is 0.779, and it increases substantially for less dense structures. For vesicular structure, R_g/R_H is close to 1, whereas for coils R_g/R_H = 1.5 (θ-solvent) or R_g/R_H = 1.8 (good solvent).

2.2.2. X-ray Scattering

The basic formalism of small-angle scattering is similar for light, neutrons and X-rays. The important difference is in the interaction of the radiation with the scattering medium. The scattering of light originates from refractive index variations while neutrons are scattered by atomic nuclei. As a result, these scattering techniques are very complementary. In the following some basic definitions common to all scattering methods but more specific to SAXS is provided.

The X-rays scattering at small angles is fully elastic because of the high energy of the radiation as compared to typical excitations in the sample. Therefore, the magnitudes of the incident and scattered wave vectors are equal (similar to light scattering, equation 2.3) and the refractive index is close to unity. The momentum transfer or scattering vector is also given by equation 2.4.

In a typical x-ray scattering experiment, the incident photon intensity per unit area per unit time (I_0) is scattered by a sample and the scattered photons are acquired by each detector element subtending a solid angle, ΔΩ, with efficiency (ε). The measured scattered intensity for negligible absorption is given by:

$$I_S = I_0 \varepsilon \Delta\Omega \frac{d\sigma}{d\Omega}$$ (eq. 2.20)

where dσ/dΩ is the differential cross-section.

In addition to scattering, part of the incident radiation is also absorbed along the beam path in the sample. Therefore, the measured scattered intensity can be expressed by:

$$I_s = I_0 \varepsilon T_r \Delta\Omega A_S l_S \frac{d\Sigma}{d\Omega}$$ (eq. 2.21)

where A_s is the cross section of the beam and $d\Omega/d\Sigma$ is the differential scattering cross section per unit volume. $d\Omega/d\Sigma$ contains information about the structure and the interactions in the system over the range of q spanned by the scattering experiment, and it is expressed in unit of reciprocal of length times solid angle (m^{-1} sterad^{-1}). Therefore, an essential step to reach a quantitative understanding of the measured intensities is the normalization of the experimental data to $d\Omega/d\Sigma$ which henceforth will be denoted by *I(q)* and given simply in unit of reciprocal length.

For a dilute system containing *N* uniform particles per unit volume, the interparticle interactions can be neglected and *I(q)* mainly depend on the shape and size of the particles.

$$I(q) = N|F(q)|^2$$ (eq. 2.22)

where *F(q)* is the coherent sum of the scattering amplitudes of the individual scattering centres within the particle given by the Fourier transform of the electron density distribution. Here coherent implies that the phase relationship between different scattered waves is preserved and their amplitudes are added up.

For randomly oriented scatters, the intensity will be isotropic in the azimuthal plane. For a uniform spherical particle of radius, R_s, and volume, V_s, the second term in the right hand side can be written as follow:

$$|F(q)|^2 = V_S^2 \Delta\rho^2 P(q, R_S)$$ (eq. 2.23)

where ρ is the electron density.

The shape of the particle is described by the Bessel function inside the brackets and *P(q,R$_S$)* is the scattering form factor for a sphere. Table 2.2 lists *P(q,R)* function for a few shapes.

A comprehensive list of *P(q,R)* functions for different particle shapes frequently occurring in scattering from soft matter systems can be found in the literature.[75] The product *N V$_S$* is the volume fraction of the particles, ϕ_S.

For non-interacting particles *I(q)* can be described by the Guinier law :

$$I(q) = NV^2 \Delta\rho^2 exp\left(-\frac{q^2 R_g^2}{3}\right)$$ (2.24)

This approximation is valid only for $1 < qR_g$ (or the leading term in q^2) and it is widely used in small angle scattering for determining R_G from the *ln I(q)* vs q^2 plot.

In the asymptotic limit, $qR_g \gg 1$, the scattering probes the interface of the particles. In the case of homogenous particles with average surface area, S, this leads to the Porod behavior,

$$I(q) = 2\pi\Delta\rho^2 S q^{-4} \tag{2.25}$$

signifying a sharp interface between the particle and the medium. Power law variation of *I(q)* is very commonly observed in SAXS from particulate systems composed of both compact and fractal morphologies as summarized in the sequence ,

$$I(q) \propto q^{-p} \begin{cases} \text{p} = 4 & \Rightarrow \quad \text{sharp interface} \\ 3 \leq \text{p} \geq 4 & \Rightarrow \quad \text{surface fractal} \\ \text{p} < 3 & \Rightarrow \quad \text{mass fractal} \\ \text{p} \approx 2 & \Rightarrow \quad \text{gaussian polymer chain} \end{cases}$$

Table 2.2: Form factors of a few commonly observed shapes in scattering from soft matter systems.

Uniform sphere of radius, R_S	$P(q, R_{S)} = \left(\dfrac{3[\sin(qR_S) - qR_S\cos(qR_S)]}{(qR_S)^3} \right)^2$
Randomly oriented cylinder of radius R_C and height H	$P(q, R_C, H) = \displaystyle\int_0^{\pi/2} \left\{ \left[\frac{2J_1(qR_C\sin\varphi)}{qR_C\sin\varphi} \right] \left[\frac{\sin((qH/2)\cos\varphi)}{(qH/2)\cos\varphi} \right] \right\}^2 \sin\varphi \, d\varphi$ J_1 – first order Bessel function and φ – orientation angle.
Spherical shell of inner and outer radii R_1 and R_2	$V^2 P(q, R_1, R_2) = 16\pi^2 [R_2^3 P(qR_2) - R_1^3 P(qR_1)]^2$ *P(q,R)* – sphere function given above.
Spherical core-shell of core and shell radii R_1 and R_2	$F^2 P(q, R_1, R_2) = [V_2\Delta\rho_2 P(qR_2) - V_1\Delta\rho_1 P(qR_1)]^2$ V_1 and V_2 are volumes of inner and outer spheres, $\Delta\rho_1$ and $\Delta\rho_2$ are contrast between shell and core, and shell and medium, respectively.

The normalized background scattering by the capillary filled with the solvent was subtracted from the normalized intensity profiles of the sample and the resulting quantity is denoted by *I(q)*:

$$I(q) = N_p V_p^2 \Delta\rho^2 P(q) S(q) \tag{eq. 2.26}$$

where N_p is the number density of scattering particles, V_p is their volume, $\Delta\rho$ is the scattering contrast, $P(q)$ is the form factor describing the shape of the particles and $S(q)$ is the structure factor describing interparticles interactions. For a relatively dilute suspension, $S(q) \approx 1$ and $I(q)$ is governed by the shape of the scattering objects. In real systems, the scattering objects have a finite size distribution, and the resulting $I(q)$ in the non-interacting case is given by

$$I(q) = N_p \Delta\rho^2 \int_0^\infty V_p^2 P(q,R) f(R) dR \qquad \text{(eq. 2.27)}$$

where $f(R)$ can be described using Schulz size distribution function[102]

$$f(R) = \left(\frac{Z+1}{R_m}\right)^{Z+1} \frac{R^Z}{\Gamma(Z+1)} \exp\left(-\frac{Z+1}{R_m}R\right) \qquad \text{(eq. 2.28)}$$

with $Z=1/(1-p^2)$, being p the polydispersity and R_m the average size.

$P(q)$ can be expressed in terms of the scattering amplitudes of two spheres of radii (R_c) and $(R_c + t)$, where t is the thickness of the shell:

$$V_p^2 \Delta\rho^2 P(q,R) = (16\pi^2/9) \left\{ (\rho_{core} - \rho_{shell}) R_c^3 F(q,R_c) - (\rho_{solvent} - \rho_{shell})(R_c+t)^3 F(q,R_c+t) \right\}^2$$

$$\text{(eq. 2.29)}$$

with

$$F(qR_i) = 3 \left[\sin(qR_i) - qR_i \cos(qR_i) \right] / (qR_i)^3 \qquad \text{(eq. 2.30)}$$

and

$$P(q,R_i) = F^2(q,R_i) \qquad \text{(eq. 2.31)}$$

ρ_{core}, ρ_{shell} and $\rho_{solvent}$ are the scattering length densities of core, shell and solvent, respectively.

Data were analyzed using the form factor $P(q)$ of spherical core-shell objects and the best fits of the modeled SAXS functions were derived by using the form and structure factors implemented in BHplot program.[103]

Above the overlap concentration (c^*) the interactions between the particles are not negligible. For simplicity, *S(q)* is approximated by an effective structure factor of hard spheres system within Perkus-Yevick approximation.[104] In this case the effective volume fraction is given by:

$$\varphi = \frac{\pi}{6} N_p \sigma^3$$

(eq. 2.32)

where $\sigma = 2(R_c + t + R_e)$ is the effective diameter taking into account the contribution of hard core, the impenetrable shell and the range of electrostatic interactions (R_e). In both the cases of solution with and without added salt the particles form permanent clusters which give rise to an excess of scattering in the low-*q* region. This additional scattering can be described with a Lorentian term $S_c(q)$, corresponding to the structure factor of the clusters[104]

$$S_c(q) = \frac{I_M}{(1 + \xi^2 q^2)^d}$$

(eq.2.33)

where I_M and ξ are proportional to the average mass and characteristic size of the clusters ($\xi^2 \approx R_g^{\,2}/3d$) and *d* is a power law exponent related to the fractal dimension of the clusters ($d \approx d_f/2$).

Thus, the total intensity including the cluster term is given by:

$$I(q) = N_p \Delta\rho^2 V_p^2 P(q)[S(q) + S_c(q)] \quad \text{(eq. 2.34)}$$

2.3. Transmission Electron Microscopy (TEM)

The Transmission Electron Microscopy (TEM) is an imaging technique largely applied in material and biological sciences. In polymer science, TEM is very helpful to determine morphologies and morphology transitions of block copolymers self-assemblies.[105] In this technique, a beam of electrons is scattered by a specimen, then an image is formed, magnified

and directed to appear either on a fluorescent screen or layer of photographic film, or to be detected by a sensor such as a CCD camera.

The layout of a transmission electron microscope is shown in figure 2.8. At the top of the column, there is a high voltage electron emitter that generates a beam of electrons that travel down the column. These electrons are scattered by the sample and an image is formed via a series of magnifying magnetic lenses. The image is ultimately focused on a detector at the bottom of the column. Apertures along the column can be used to change the contrast and resolution of the image. The column itself is at a very high vacuum to prevent interactions between the electron beam and air molecules.
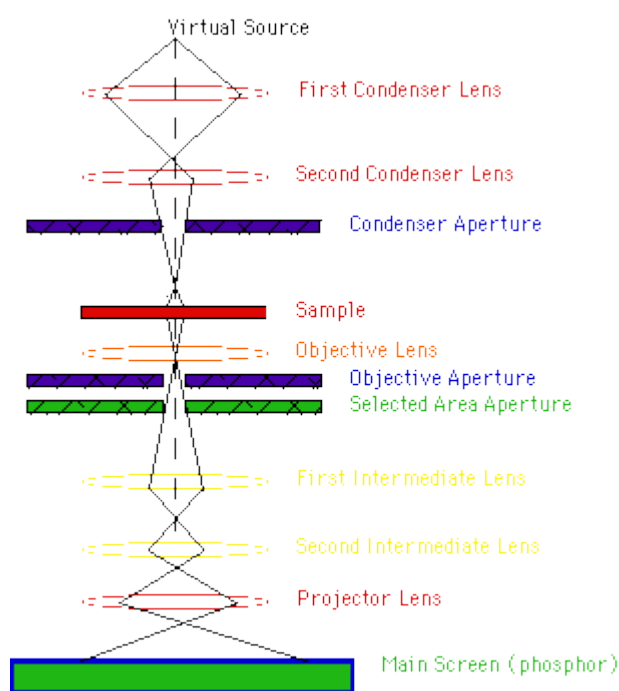
Figure 2.8. Schematic representation of a Transmission Electron Microscope setup.

The contrast in TEM is a result of interference between electrons coming in from different angles. When electrons interact with the sample they are bent away from their original path, and will thus interfere with the main electron beam. If a small objective aperture is used, electrons that get deflected at a large angle are blocked, and the contrast of the image is enhanced. However, electrons with a high deflection contain high resolution information and are therefore lost. A balance needs to be achieved between having good contrast and having a high resolution.

Normally, small copper discs also called grids (Figure 2.9) with a fine mesh are used in TEM experiments. A thin layer of carbon is deposited on top of this grid, by evaporating carbon onto it. This thin carbon film must be made hydrophilic for facilitativy sample spreading.
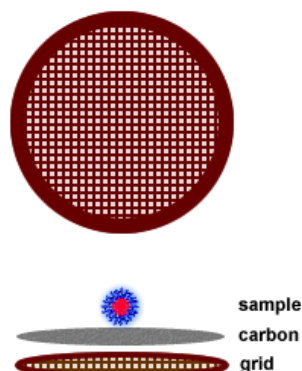
Figure 2.9. *Top:* Overhead view of a grid, showing the mesh. *Bottom:* Side view of a carbon coated grid showing the relative position of the carbon film to the grid and sample.

The main components of many organic molecules are carbon, oxygen, nitrogen, and hydrogen. These atoms are not very dense, and the amount of electrons they scatter is minimal compared to the intensity of the electron beam. Therefore, for normal EM viewing, samples are negatively staining with a heavy metal salt that readily scatters strongly electrons (Figure2.10).
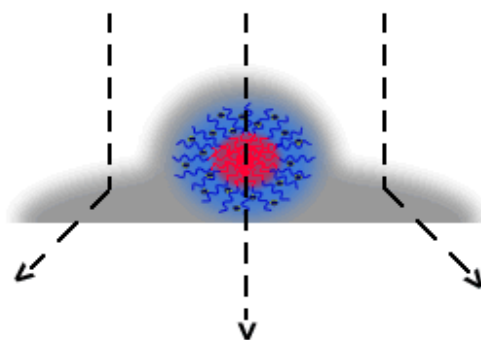
Figure 2.10. A sample (micelle) deposited on a carbon coated grid and surrounded by stain interacting with the electron beam (arrows).

For high resolution studies unstained samples are observed by cryo-electron microscopy, holey grids are used in conjunction with freeze-sample (cryo) electron microscopy. Similar to normal carbon coated grids, holey grids are covered with a fine perforated layer of carbon (Figure 2.11). One of the purposes of these holes is to eliminate any absorption and scattering

of the electron beam by the carbon film, which will generate noise and obstruct the signal. The holes also allow for "pockets" of solvent to form. Within these pockets, the specimen remains fully hydrated, even when the sample has been frozen.
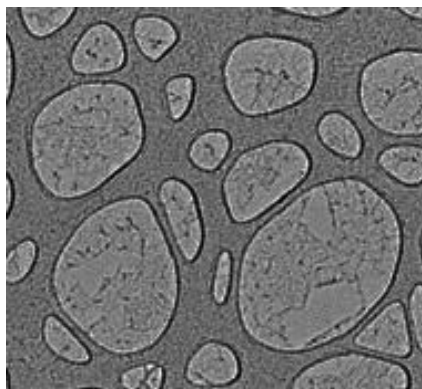
Figure 2.11. Image of a perforated carbon film, often referred as holey grid.

2.4.   Quartz Crystal Microbalance with Dissipation Monitoring (QCM-D)

A complete description of the piezoelectric quartz crystal microbalance (QCM) setup has been done by Rodahl et al.[106] The QCM is an ultrasensitive weighing device, consisting of a thin disk of single crystal quartz, with metal electrodes deposited on each side of the disk. The crystal is connected to an external driving oscillator circuit and oscillates at its resonant frequency (*f*). As this device is weight sensitive, any mass added or removed from the crystal surface will induce a frequency shift (Δf) related to the mass change (Δm).

The mass of the adhering layer is calculated by using the Sauerbrey relation[107]

$$\Delta m = -\frac{C \times \Delta f}{n}$$

(eq. 2.35)

C = 17.7 ng Hz^{-1} cm^{-2} for a 5 MHz quartz crystal.
n = 1,3,5,7 is the overtone number.
If the adsorbed film is not rigid (viscoelastic), the Sauerbrey relation becomes invalid because it will underestimate the mass at the surface. The film's softness or viscoelasticity can be measured using the dissipation (D), defined as:

$$D = \frac{E_{lost}}{2\pi E_{stored}}$$

(eq. 2.36)

where, E_{lost} is the energy lost (dissipated) during one oscillation cycle and E_{stored} is the total energy stored in the oscillator.

2.5.   PolyAcrylamide Gel Electrophoresis (PAGE)

The Polyacrylamide Gel Electrophoresis (PAGE) technique is a classical biochemical method allowing to separate proteins by their electrophoretic mobility, wich is a function of the protein size (molecular weight, folding).

Very often electrophoresis is done in the presence of sodium dodecylsulphate (SDS) (SDS-PAGE). This anionic detergent binds and denatures proteins by breaking up the non-covalent, implying that protein mobility is determined primarily by the mass, with minor influence of folding. The measurements can also be done without SDS, but in this case different proteins with similar molecular mass will migrate differently due to differences in folding.

In a typical procedure, the sample is placed on the top of the gel (stacking gel) containing a buffer solution and an electrical field is applied across the gel from the top to the bottom (resolving gel) carrying the negatively charged anions down through the gel. The molecules are separated as a function of their mobility, which is proportional to its charge/mass ratio. Molecules with the same charge/mass ratio are sieved by size (small proteins move faster them the large ones).

2.6.   Fluorescence Spectroscopy

One of the most fascinating characteristics of block copolymers is their ability to self-assemble in selective solvents. The formation of well defined structures can be studied specially using fluorescent probes to evaluate the polarity of various microenvironments.

The pyrene molecule is widely used to study such a phenomenon. Several absorption bands can be observed in its emission spectra, and two among them (F1 at 372 nm and F3 at 383 nm for λex = 335 nm) are affected principally by the polarity of the probe surroundings, as shown in Figure 2.12. The ratio between F3 and F1 intensities can be related not only with the self-assembly process but also with the local structure of the resulting object.[108] The transfer of pyrene molecules from the solvent (polar) to inside micellar core (apolar) during the micellization of amphiphilic copolymers in aqueous media can be followed by measuring F1 and F3 intensities and, consequently, the critical micelle concentration (CMC) can be determined (see Figure 2.12(b)). The critical micelle concentration is the concentration below which only molecularly dissolved chains exist but above which both micelles and single chains are present simultaneously.

For a copolymer concentration Cp above the CMC the micelle is thermodynamically stable with respect to dissociation . If Cp < CMC, micelles may still be kinetically stable and survive for a given period of time, depending on the characteristics of the core-forming block (size, glass transition temperature, crystallinity, etc).[45, 109]
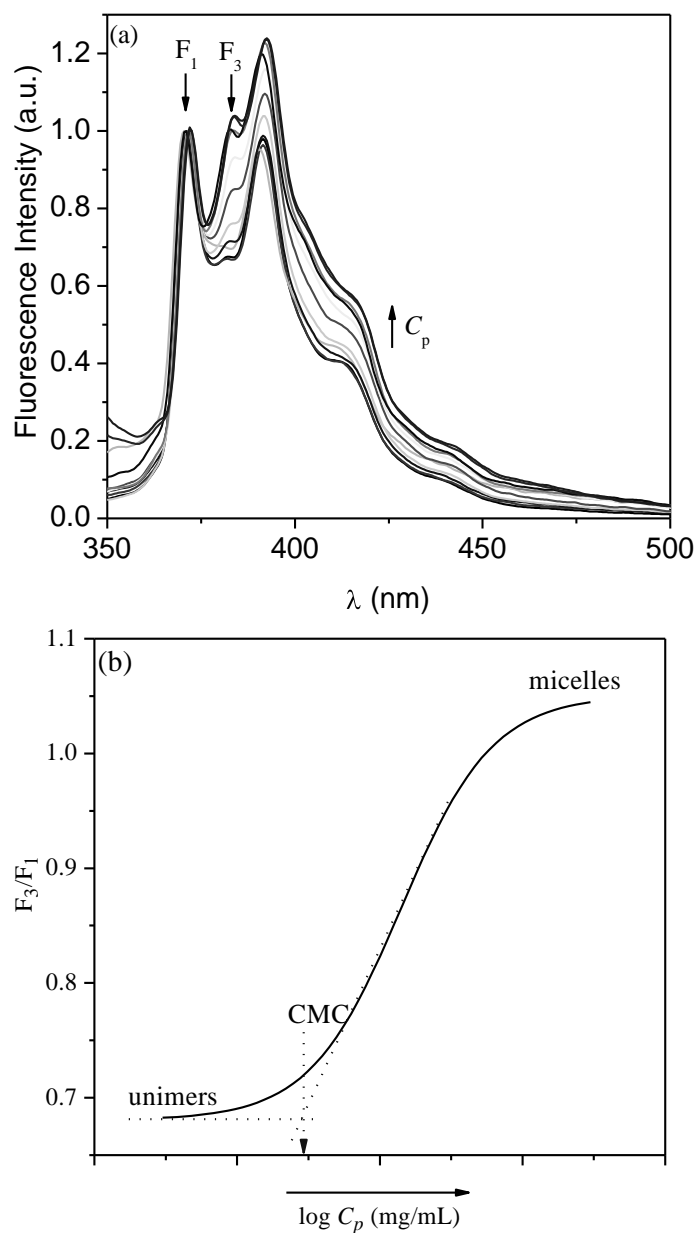
Figure 2.12. Pyrene fluorescence emission spectra (a) and the corresponding variation in the F3/F1 ratio (b) as a function of the copolymer concentration ([pyrene]$_{ct}$ = 6.0x10-7 mol/L, λex = 335 nm).

Chapter 3

Small unilamellar Lipid Vesicles

decorated with Annexin-A5 protein

The present chapter deals with the study of the binding of Annexin-A5 to small unillamelar vesicles by QCM-D, scattering (DLS) and imaging (TEM) techniques. The use of QCM-D and TEM in the study of lipid vesicles and theiur interaction with proteins is already well stablished and described in the literature, whilst the use of DLS is still comparatively limited in spite the fact of being an extremely powerful technique.

Indeed, scattering techniques (DLS, SLS, and X-ray) have been rarely used in the study of lipid structures. However, in the present work they have provided important complementary insights into the system, allowing for a better understanding of the lipid-protein interaction and behavior in solution. This preliminary study was the starting point in the elaboration and development of the present work.

A stock solution of small unillamelar vesicles at a C_{lip} = 5.0 mg/mL was prepared using a mixture of DOPC (1,2-dioloeyl-sn-glycero-3-phosphocoline) and DOPS (dioleoyl-phosphatidylserine) with a molar ratio of 4:1, as described in the *Experimental Part*. All the results herein reported were obtained using dilute solutions from the same stock solution.

3.1. Quartz Crystal Microbalance with Dissipation Monitoring – QCM-D

The formation of a Supported Lipid Bilayer (SLB) by deposition of lipid vesicles is illustrated in Figure 3.1. The QCM-D response shows a two phase behavior in agreement with the work published by Richter et al.[12] The initial phase corresponds to the formation of a stable but incomplete vesicular layer (SVL) due to the adsorption of intact vesicles and, in the second phase, surface bound vesicles transform into a continuous SLB. This second phase is evidenced by the decline in dissipation as a result of the transformation into a rigid structure and, the decrease in frequency in part due to the release of water from the surface bound lipid structure. The final frequency shift was -26.1 Hz, and the final dissipation was < 0.1 x 10^6, in agreement with the results reported in the above cited reference.
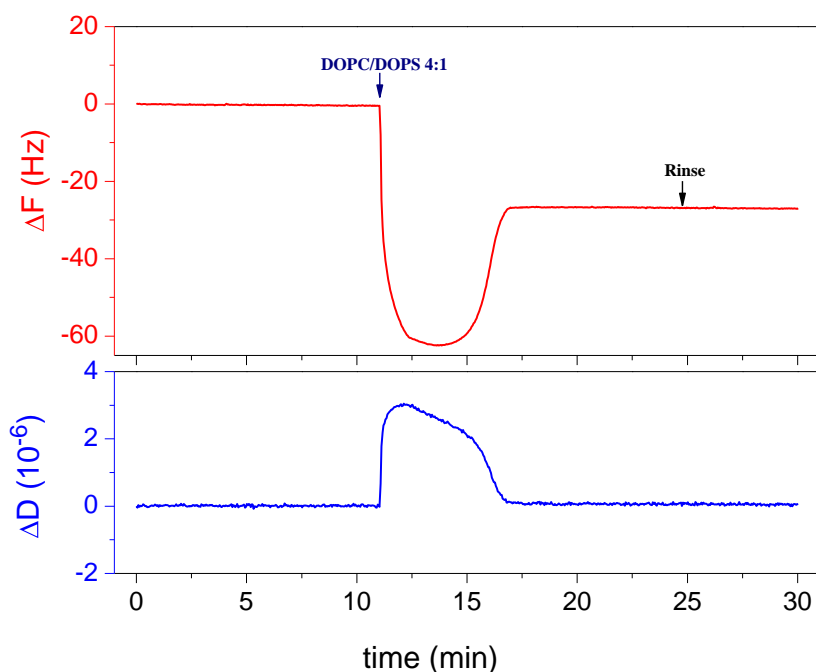
Figure 3.1. QCM-D data for the deposition of small unilamellar vesicles (SUV) made of 80% DOPC and 20% DOPS on silica.

The adsorption of the Annexin-A5 on silica-SLBs is shown in Figure 3.2.   After incubation with Annexin-A5 in presence of calcium ions ([CaCl$_2$] = 2.0 mM), the protein adsorption causes a decrease in frequency depending on the protein concentration. The maximum frequency shift was -15.3 Hz (close to the literature report of -18 Hz for DOPC/DOPS 4:1)[110], corresponding to the maximum surface coverage at a protein concentration of 20 μg/mL. The dissipation remains almost constant suggesting a tight protein association on the SLB. The equilibrium is reached in a few minutes, and the frequency remains constant after rinse with a solution containing the same calcium concentration. However, the Annexin-A5 can be released by decreasing the calcium concentration (free calcium cations) using a solution containing a calcium chelating agent (EGTA). After rinse with EGTA, the SLB can be recovered without significant perturbation as judged from the QCM-D data, even after repeated cycles of protein adsorption and desorption.[110]
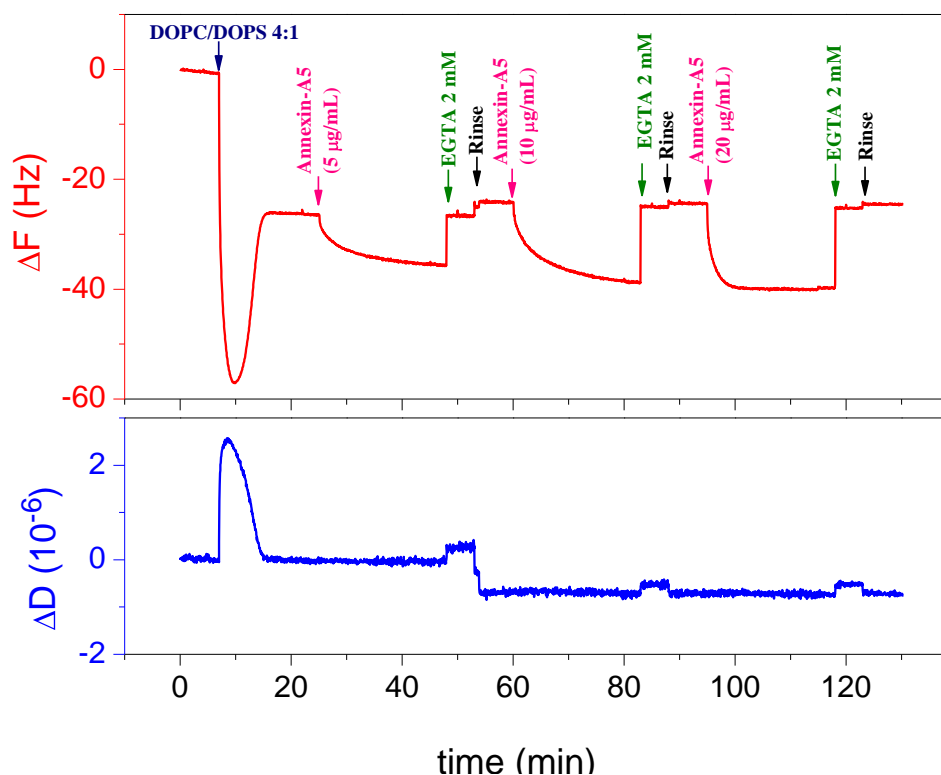
Figure 3.2. QCM-D response (frequency (Δf) and dissipation (ΔD)) for the adsorption of Annexin-A5 on to SLB. The process was measured for the incubation of different protein concentrations (as indicated) in the presence of 2 mM $CaCl_2$.

3.2. Static and Dynamic Light Scattering (SLS and DLS)

It has been shown that Annexin-A5 binds onto Support Lipid Bilayers or Small Unilamellar Vesicles in solution formed by mixtures of lipids having phosphatidylcholine (neutral) and phosphatidyl serine (negative) motifs (Scheme 3.1).[10, 111-114] In the case of SUVs in aqueous solutions, the binding process can be readily evidenced by Dynamic Light Scattering (DLS).

Figure 3.3 shows typical autocorrelation functions $C(q,t)$ and distributions of the relaxation times $A(t)$ at scattering angle of 90° as revealed by CONTIN analysis for 0.1 mg/mL solution of DOPC/DOPS 4:1 freshly prepared (a) and after 3 months (b) . Narrow distributions of relaxation times, with a single dominant mode corresponding to the diffusive motion of the small unillamelar vesicles in solution, whose characteristic hydrodynamic diameter ($2R_H$) was 66 nm were obtained for freshly prepared (sonicated) samples. The inset in Figure 3.3(a) depicts the typical q^2-dependence of the relaxation frequency (Γ) for diffusive scattering particles.[95]

However, after a few months (picture 3.3(b)) the distribution of the relaxation time observed is larger than for freshly prepared vesicles, and the q^2-dependence of the relaxation frequency (Γ) reveals contributions of different species that cannot be resolved by CONTIN analysis. Such a change in the light scattering behavior as a function of the time can be attributed to the aggregation due to van der Waals interactions[9] and merging of various individual SUVs. The appearance of a second distribution of relaxation times for high q-values (small scattering angles) confirms the formation of aggregates.
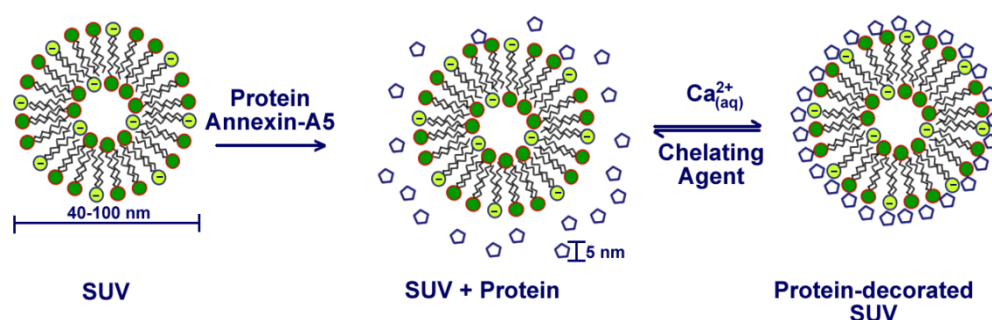
Scheme 3.3. Formation of protein-decorated SUVs.

The ratio between the radius of gyration (R_g) and the hydrodynamic radius (R_H) for a freshly prepared SUV solution could be calculated using the R_g determined by the dissymetry method (Figure 3.4).[115] With an angular coefficient of 0.380, a R_g = 40.38 nm was calculated, and consequently a R_g/R_H ratio of 1.22 was obtained, in good agreement with the formation of vesicular structures. [100, 101]
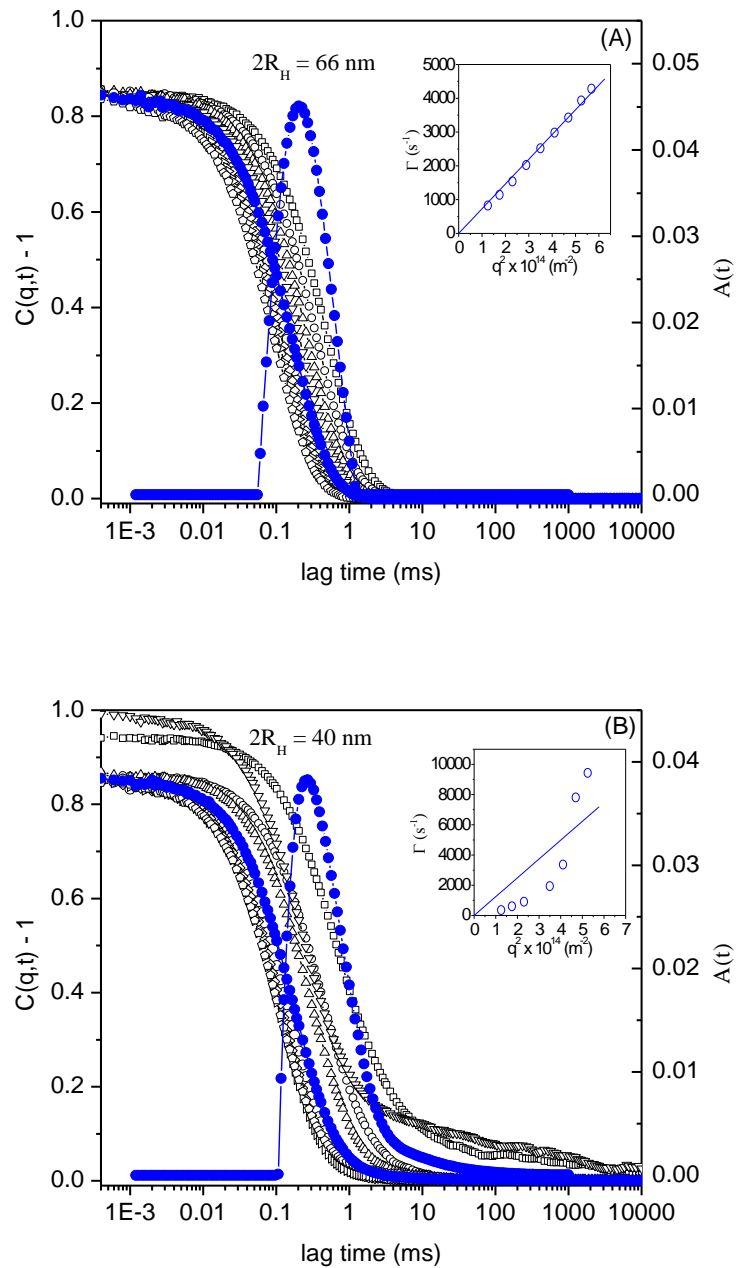
Figure 3.3. Autocorrelation functions *C*(q,t) measured at scattering angles between 50° and 130°, and distributions of relaxation times *A*(t) at 90° as revealed by CONTIN analysis for 0.025 mg/mL solutions of SUVs made of DOPC/DOPS (4:1) in HEPES buffer solution at pH 7.4 freshly prepared **(A)**, and after 3 months **(B)**.
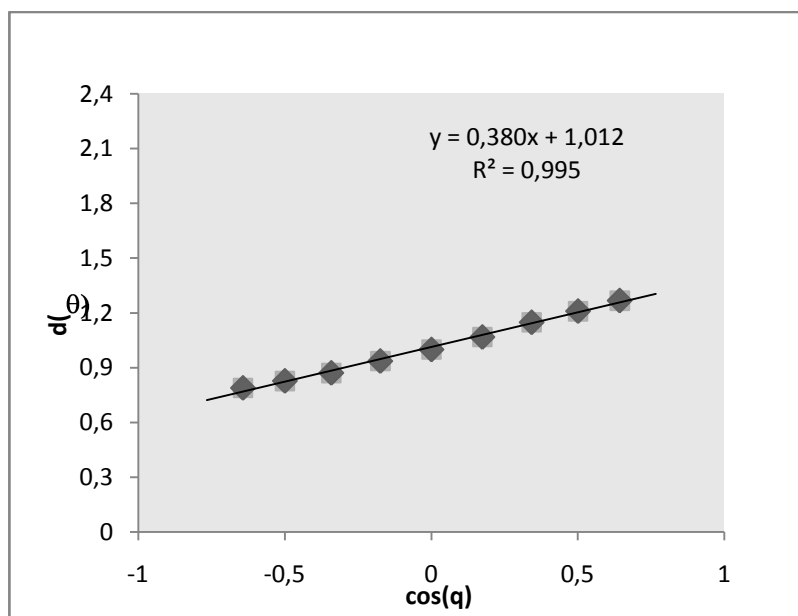
Figure 3.4. Dissymmetry, d(θ),of the static scattering intensity for 0.1 mg/mL solutions of SUVs made of DOPC/DOPS (4:1) freshly prepared in HEPES buffer solution at pH 7.4.

The concentration influence on the vesicular size was also studied using dynamic light scattering. The variation of the hydrodynamic radius as a function of the lipid concentration is shown in Figure 3.5. The overall behavior comprises an increase in the vesicular size as the lipid concentration increases from 0.025 up to 0.10 mg/mL, followed by a decrease as the lipid concentration increases up to 0.20 mg/mL. The same behavior has been described for unillamelar vesicles formed with dihexanoyl phosphorylcholine (DHPC) and dimyristoyl phosphorylcholine (DMPC).[116] At high scattering angles a slight dependency is observed, however it becomes significant as the scattering angle decreases. Such angular dependency can be explained by considering the fact that the solution in this case was not freshly prepared, due to reasons already discussed above for figure 3.3(B).
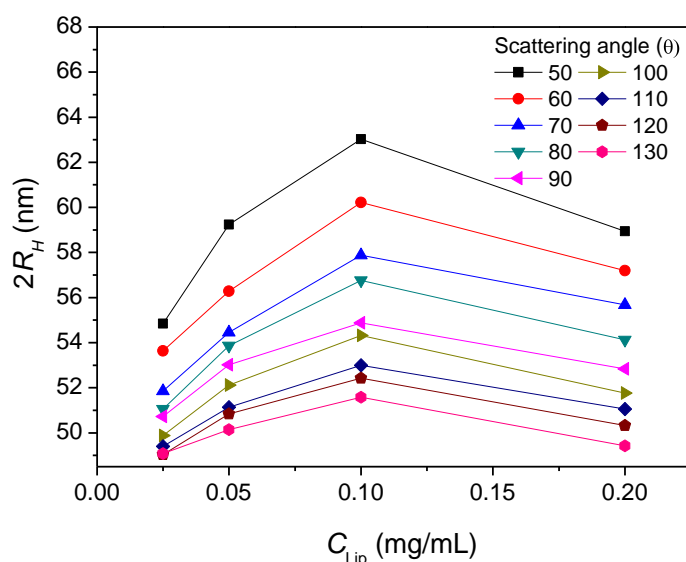
Figure 3.5. Hydrodynamic radius (R_H) as a function of the lipid concentration (C_{Lip}) for small unillamelar vesicles formed by DOPC/DOPS (4:1) in HEPES buffer solution at pH 7.4.

Figure 3.6 displays the autocorrelation functions C(q,t) and distributions of the A(t) at scattering angle of 90° as revealed by CONTIN analysis for 1.0 mg/mL solution of Annexin-A5. Narrow distributions of relaxation times with two dominant modes corresponding, respectively, to the diffusive motion of Anexin-A5 protein and its aggregates in solution were observed. The inset in Figure 3.6 corresponds to the fastest relaxation time due to Annexin-A5, whose characteristic hydrodynamic diameter ($2R_H$) was 5.6 nm, and depicts the typical q^2-dependence of the relaxation frequency (Γ) for diffusive scattering particles.

As showed in Figure 3.7, when a solution of Annexin-A5 and a solution containing SUV are mixed-up the light scattering experiments present a result corresponding to the sum of the results in Figure 3.5 and 3.3, independent of protein and SUVs concentrations. It is possible to see typical distributions of relaxation times corresponding to Annexin-A5 and SUVs, with the same original hydrodynamic sizes ($2R_H$ = 5.6 and 62 nm, respectively).
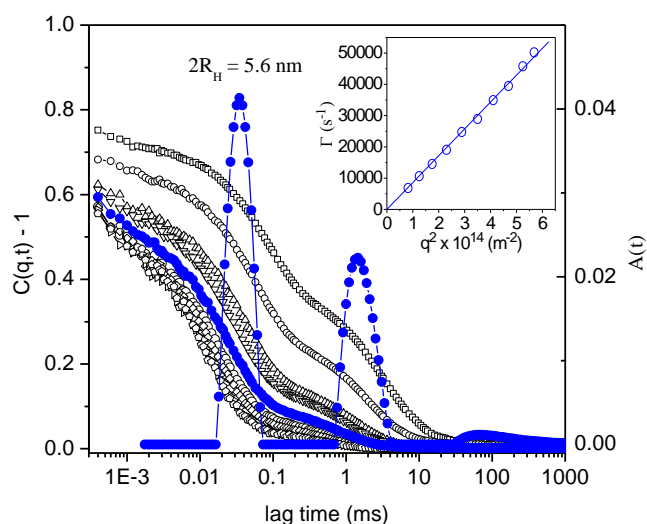
Figure 3.6. Autocorrelation functions C(q,t) measured at scattering angles between 50° and 130° and distributions of relaxation times A(t) at 90° as revealed by CONTIN analysis for 1.0 mg/mL solutions of Annexin-A5 in TRIS buffer solution at pH 8.0**.**
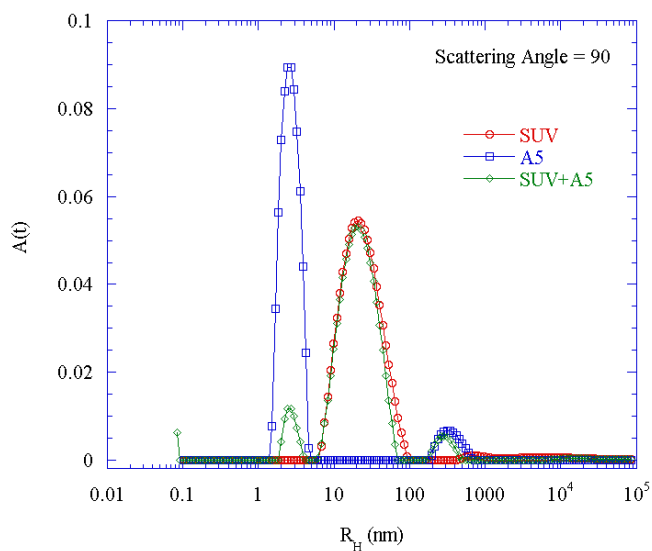
Figure 3.7. Distributions of hydrodynamic radius (R_H) for solutions containing 2.4 mg/mL of Annexin-A5 in TRIS buffer solution at pH 8.0, 1.0 mg/mL of SUVs made from DOPC/DOPS (4:1), and a mixture of 0.6 mg/mL of Annexin-A5 and 0.025 mg/mL of SUVs, as indicated.

Upon calcium addition, the Annexin-A5 binds to the phospholipids present in SUVs surface, and, as a consequence, there occurs an increase in the size of the assembled structure. As

represented in Figure 3.8, an increase of 6 nm is observed in the $2R_H$-value. The protein bind was also confirmed by an increase in the total scattered light intensity upon calcium addition, as well as by the reversibility of the process evidenced upon EGTA addition (Figure 3.9).
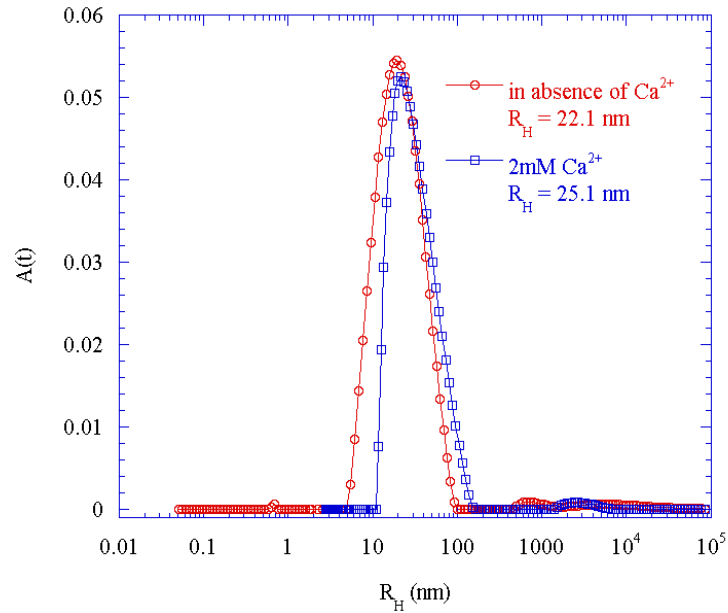
Figure 3.8. Distributions of hydrodynamic radius (R_H) for solutions containing 0.6 mg/mL of Annexin-A5 plus 0.025 mg/mL of SUVs in presence and absence of 2mM Ca^{2+}, as indicated.
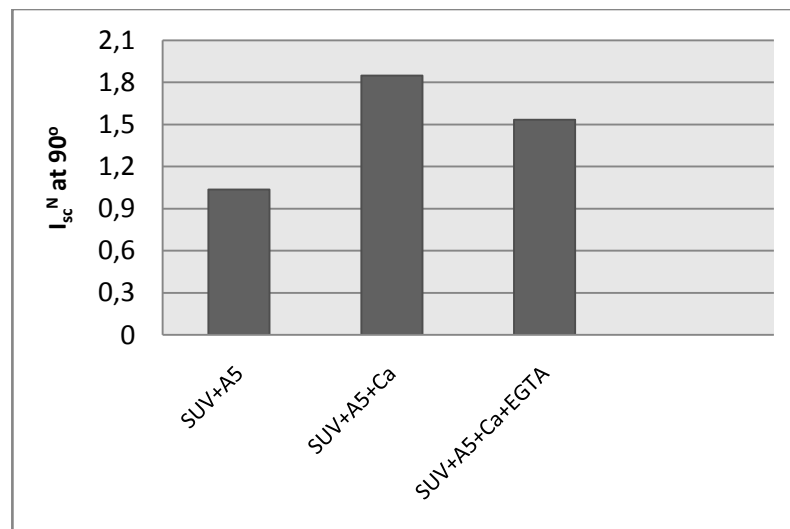
Figure 3.9. Total scattered light intensity at a scattering angle of 90° for solutions containing 0.6 mg/mL of Annexin-A5 plus 0.025 mg/mL of SUVs in presence and absence of 2 mM Ca^{2+}, and after addition of 2 mM EGTA, as indicated.

Cryo-TEM

Figure 3.10 shows a cryo-TEM image of a SUV formed with DOPC/DOPS (4:1). As we can observe, the image confirms the presence of a vesicular structure with a typical diameter of 84 nm, and a wall thickness of 40 Å corresponding to the lipid bilayer. The size of such an object is a bit larger than the one reported by DLS experiments ($2R_H$ = 62 nm). However, this is an expected difference, as the DLS reports an intensity-average value while the TEM reports a number-average value. For SUVs decorated with Annexin-A5, a wall structure with high contrast and with a 60 Å thick wall is observed (Figure 3.11). Such an increase in both, wall thickness and contrast, is due to the protein binding to the lipid bilayer, thus increasing the density and thickness of the vesicular wall. The image shows a protein decorated SUV with a diameter of 70 nm.
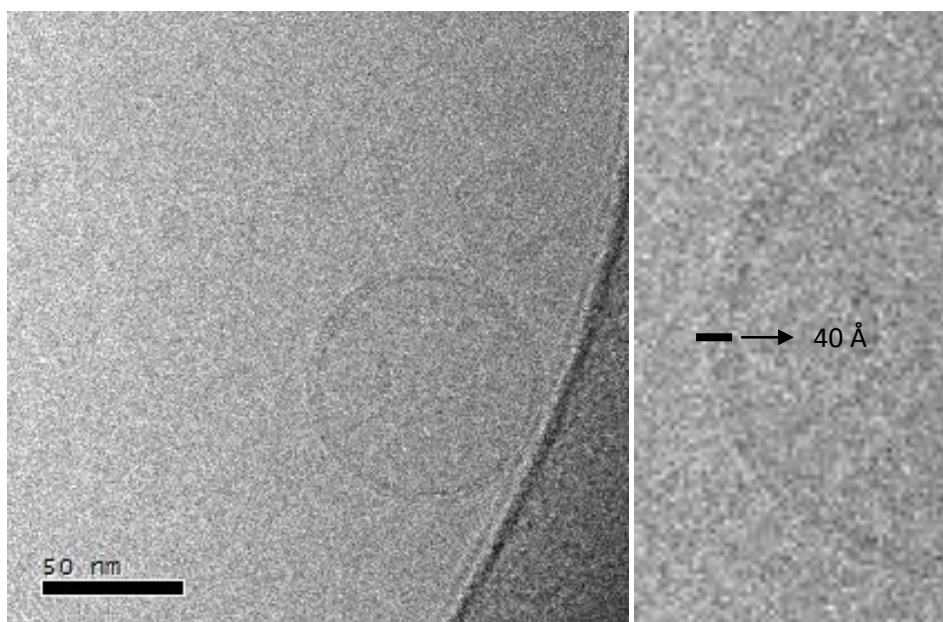
Figure 3.10. Cryo-TEM image of SUV made from DOPC/DOPS (4:1) **(a)**, and an magnified image of the same SUV showing the lipid bilayer (the vesicle wall) with a thickness of 40 Å **(b)**.
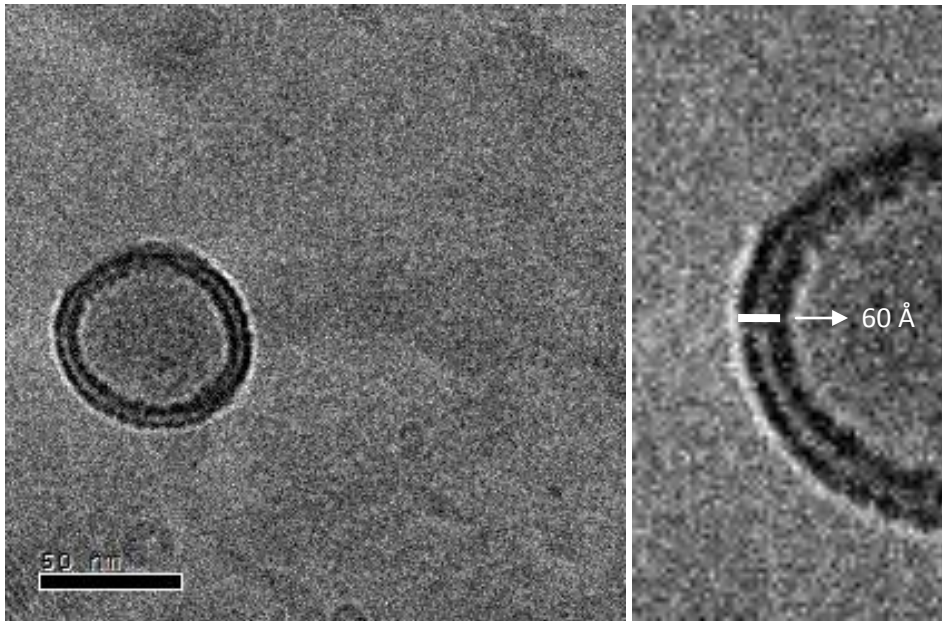
Figure 3.11. Cryo-TEM image of SUV made from DOPC/DOPS (4:1) decorated with Annexin-A5 **(a)**, and an magnified image of the same assembled structure showing a vesicular wall with a thickness of 60 Å corresponding to the lipid bilayer decorated with Annexin-A5 **(b)**
.

Chapter 4

PBuA-*b*-PECVPD

micelles decorated with Annexin-A5

4.1. Copolymer Synthesis and Characterization

The synthesis procedure employed to prepare the PECVPD-*b*-PBuA diblock copolymer is illustrated in Scheme 4.1. The bromo-terminated poly(n-butyl acrylate) (PBuA) macroinitiator was prepared using ethyl α-bromoisobutyrate (EBriBu) as the initiator and PMDETA as the ligand in toluene with mesitylene (1.0 mL) as internal ^{1}H NMR standard. After 75 min at 70^oC, the conversion was 59%, as judged by ^{1}H NMR. The characteristics of the PBuA$_{35}$-Br macroinitiator are summarized in Table 4.1

Dimethyl(1-ethoxycarbonyl)vinyl phosphate monomer (DECVP) was synthesized as described by Barton et al.[117] (Scheme 4.1), and the distilled product gave 60% of yield.

The transition metal mediated living radical polymerization of (DECVP) monomer was reported recently by Huang and Matyjaszewski.[118] In the cited article, the authors gave a comprehensive study on the effect of initiator and ligand structures, catalyst and deactivator concentrations, temperature and reaction time. In our approach to prepare diblock copolymer micelles with protein binding ability, experimental conditions were those resulting in the highest monomer conversion (entry 8 ref. [118]) using standard Atom Transfer Radical Polymerization (ATRP) protocols.[23]

Macroinitiator

Buthyl acrylate (BuA)

A

Bromo-terminated poly(buthyl acrylate)
(PBuA-Br)

Monomer

Trimethyl phosphite

i) room temperature, 1h
ii) 50 $^{\circ}$C, 1h
iii) distilled under reduced pressure

B

Dimethyl(1-ethoxycarbonyl)vinyl phosphate
(DECVP)

Diblock Copolymer

A + **B**

CuBr, HMTETA

2-butanone
70 $^{\circ}$C, 6h

C

PDECVP-*b*-PBuA

Poly((1-ethoxycarbonyl)vinyl phosphate diacid)-*b*-poly(buthyl acrylate)
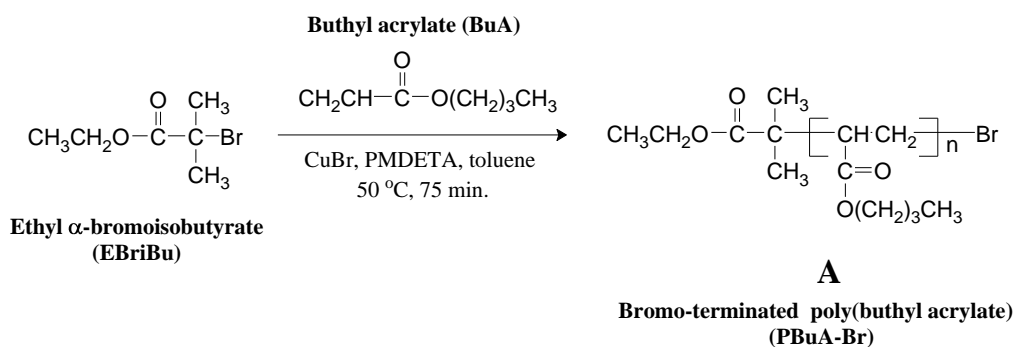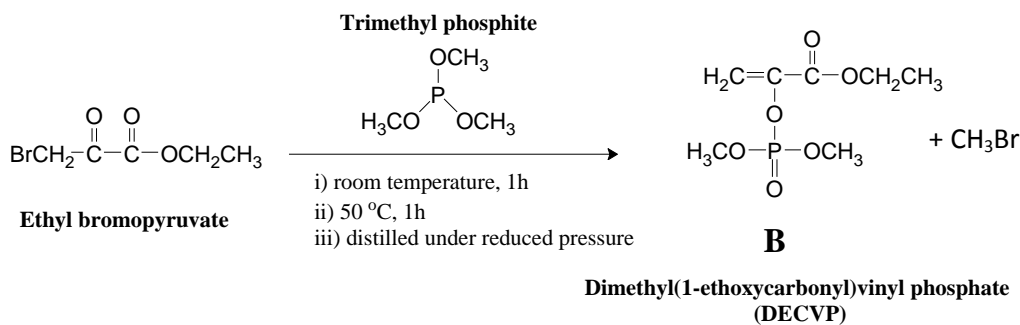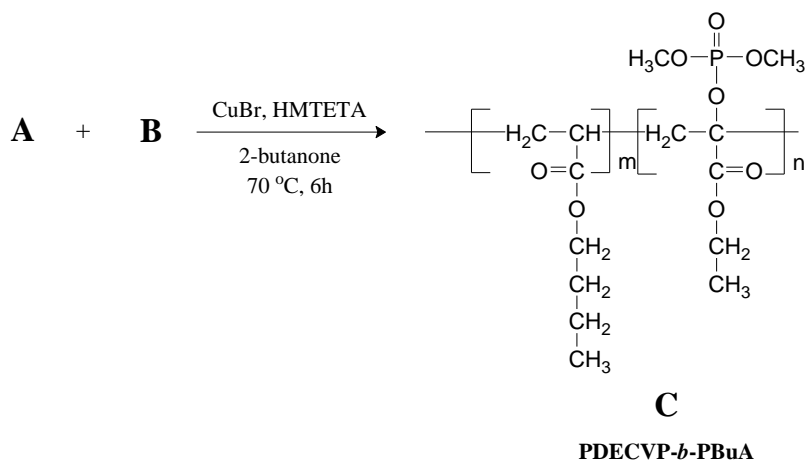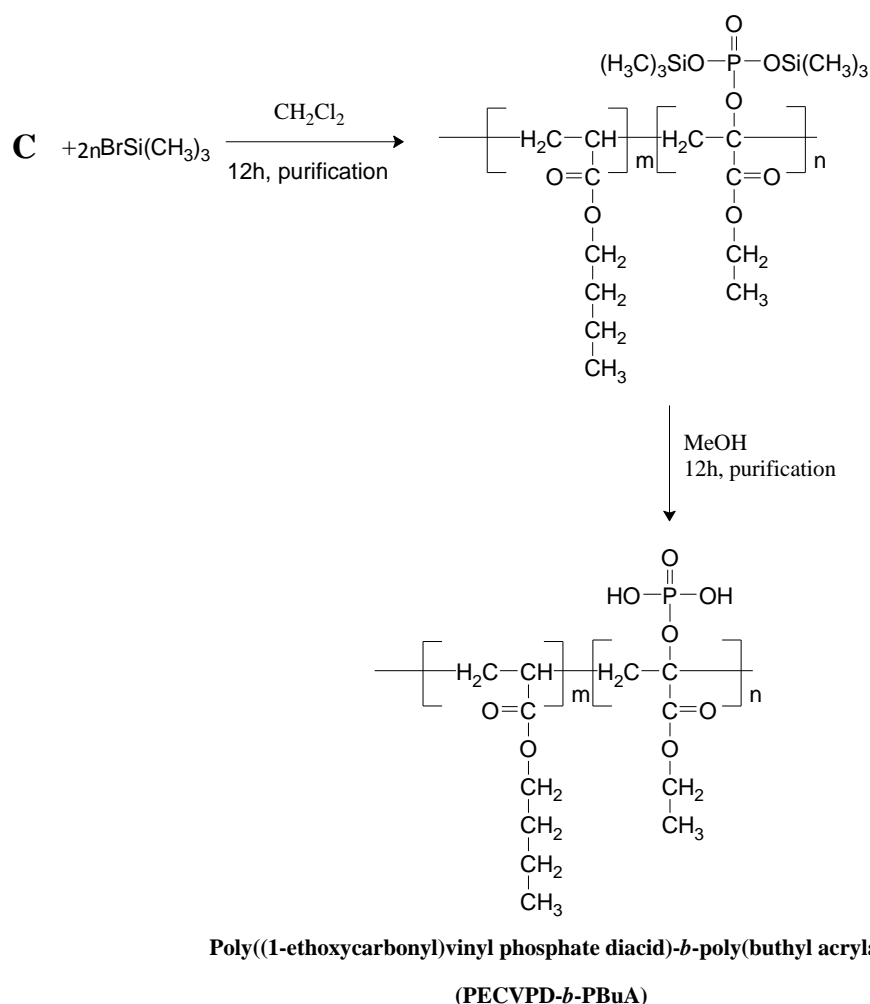
(PECVPD-*b*-PBuA)

Scheme 4.1. Method employed to synthesize PECVPD-*b*-PBuA diblock copolymers.

Using the PBuA-Br macroinitiator, after 4h at 70 $^{\circ}$C the conversion of DECVP monomer progressed up to 33% , and no further chain extension was observed for longer reaction times. Presumably, this phenomenon is due to premature termination.[118]. Figures 4.1 and 4.2 depict assigned ^{1}H NMR spectra in CDCl$_3$ and DMF GPC traces, respectively, for PBuA$_{35}$-b- PDECVP$_{30}$ diblock copolymer and PBuA$_{35}$-Br macroinitiator. In Figure 4.1, the appearance of chemical shifts related to functional groups present in the PDECVP block are noticeably observed after extension of PBuA chains by ATRP of DECVP monomer. Very importantly, the comparison of GPC traces (Figure 4.2) show that the molar mass of the macroinitiator indeed shifted towards lower retention times corroborating chain extension, and no significant trace of unreacted macroinitiator in the copolymer was observed. M$_n$(GPC)-value was recorded using DMF (at

room temperature) as eluent. The molecular characteristics of PBuA$_{35}$-b- PDECVP$_{30}$ are summarized in table 4.2.

Table 4.1. Characteristics of the PBuA$_{35}$-Br macroinitiator.

M$_n$ (target)[a]	Mn(theo)[b]	M$_n$ (^{1}H NMR)[c]	M$_n$ (GPC)[d]	M$_w$/M$_n$
(g/mol)	(g/mol)	(g/mol)	(g/mol)	
8,900	5,200	4,400	4,500	1.12

[a] At quantitative monomer conversion.
[b] Calculated based on the conversion (59%) estimated by ^{1}H NMR in CDCl$_3$
[c] Determined by ^{1}H NMR measurements in CDCl$_3$ using the initiator ethyl moiety as reference.
[d] Determined by GPC measurements in THF with poly(styrene) standards.
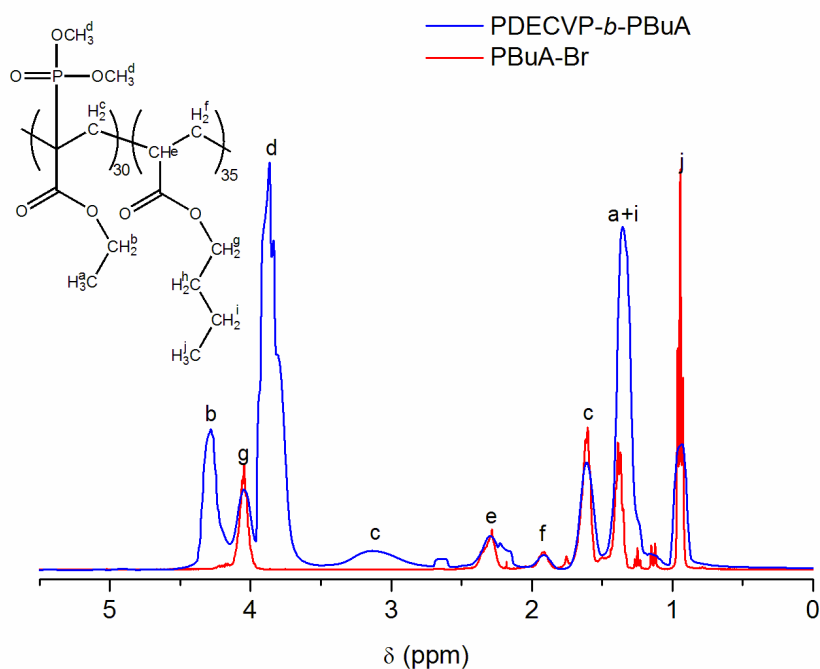
Figure 4.1. ^{1}H NMR spectra of PBuA-b- PDECVP diblock copolymer and PBuA-Br macroinitiator in CDCl$_3$.
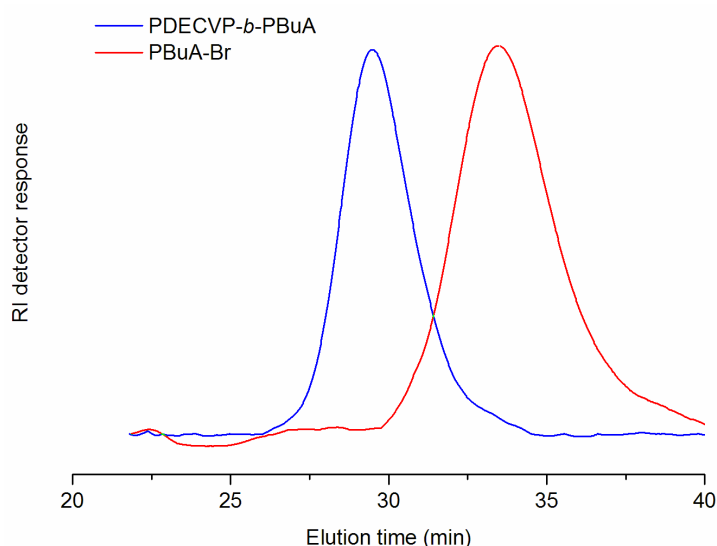
Figure 4.2. GPC traces of PBuA-b- PDECVP diblock copolymer and PBuA-Br macroinitiator in DMF at room temperature using poly(styrene) standards.

The sylilation of $-P(O)(OCH_3)_2$ functional groups in the intermediate step for the conversion of poly(dimethyl(1-ethoxycarbonyl)vinyl phosphate) (PDECVP) into poly (1-ethoxycarbonil)vinylphosphonic diacid) (PECVPD) was confirmed by ^{1}H NMR as shown in Figure 4.3, which shows the disappearance of $-P(O)(OCH_3)_2$ signal at ca. 3.8 ppm, whereas typical chemical shift of sylilated residues appeared at low field. The addition of methanol to the silytaded product induced the methanolysis. A slightly yellow powder was obtained after solvent evaporation and washing with ethyl ether. ^{1}H NMR of the resulting compound confirmed complete converse on of $-P(O)(OCH_3)_2$ groups into $-P(O)(OH)_2$ diacid groups (see Figure 4.4).

Table 4.2. Characteristics of the PBuA$_{35}$-b- PDECVP$_{30}$ diblock copolymer.

M_n (target)[a] (g/mol)	Mn(theo)[b] (g/mol)	M_n (GPC)[d] (g/mol)	M_w/M_n
26,900	11,900	14,300	1.16

[a] At quantitative monomer conversion.
[b] Calculated based on the conversion (33%) estimated by ^{1}H NMR in CDCl$_3$ using mesitylene as internal reference.
[c] Determined by GPC measurements in pure DMF at 25°C with poly(styrene) standards.
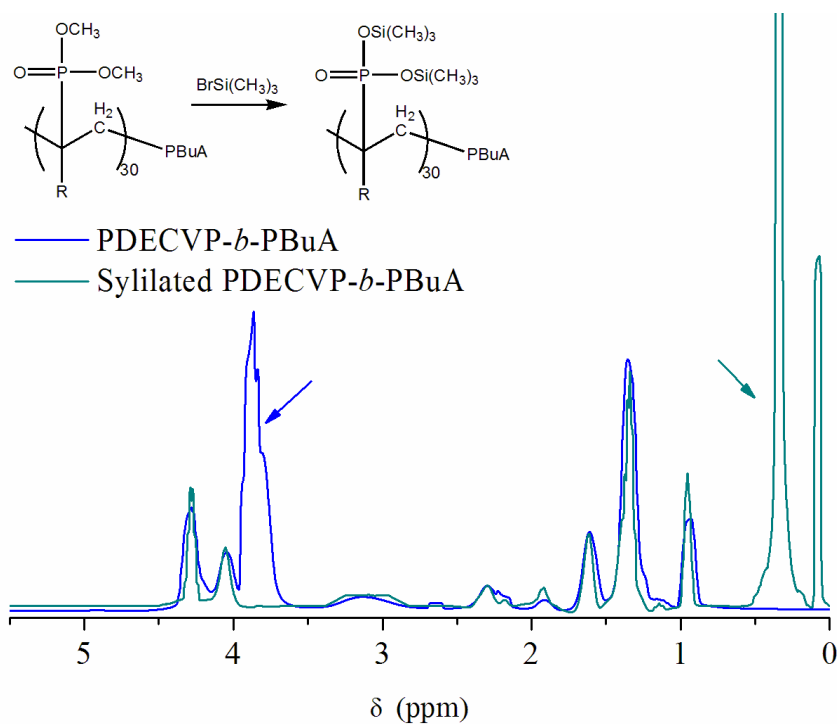
Figure 4.3. ^{1}H NMR spectra of PBuA-b- PDECV Pand sylilated PDECVP-*b*-PBuA in CDCl$_3$.
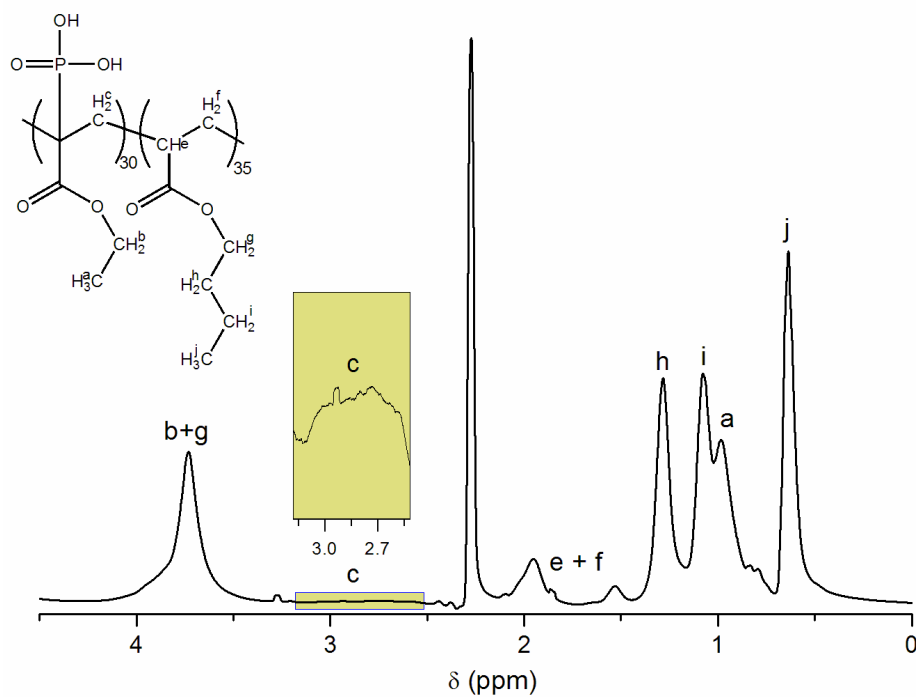
Figure 4.4. ^{1}H NMR spectra of PBuA-b- PDECVP in DMSO-*d$_6$*.

4.2. Polyelectrolyte behavior of PBuA$_{35}$-*b*- PDECVP$_{30}$

The PECVPD polymer is formed by monomer units having at the same time two pendant groups with opposite solubility properties. While the ethyl side groups are typically hydrophobic and hence insoluble in water, the presence of an equal number of highly hydrophilic phosphate moieties along the chain ultimately confers temperature-responsiveness to system. It has been observed that PDECVP dissolves molecularly in water at low temperature, but switches from hydrophilic to hydrophobic at a given critical solubility temperature (CST) upon heating.[118] The characteristic CST of PDECVP depends on both C_p and M_n, decreasing with the increase of such parameters. It was observed, for example, that the CST of a M_n = 14 900 g/mol sample decreases from 85 to 77°C as the C_p increases from 5.0 to 20.0 mg/mL.[118]

Therefore, at ambient temperature the PBuA$_{35}$-*b*-PECVPD$_{30}$ diblock copolymer consists of two segments of opposite water solubility; water being a solvent thermodynamically good for PECVPD but poor solvent for PBuA. As a result, PBuA$_{35}$-*b*-PECVPD$_{30}$ chains self-assemble upon contact with aqueous environment into spherical micellar aggregates, whose structures comprise a hydrophobic PBuA core and a hydrophilic PECVPD corona bearing negatively charged phosphate moieties (Scheme 4.2). The CMC of this system was found to be 0.002 mg/mL in water (no added salt), as determined by fluorescence spectroscopy using pyrene as probe (Figure 4.5). This value is fairly comparable with those reported in the literature for poly(butyl acrylate)$_{90}$-*b*-poly(acrylic acid)$_{100}$ (PBuA$_{90}$-*b*-PAA$_{100}$) and poly(*t*-butyl styrene)$_{26}$-*b*-poly(sodium styrene sulfonate)$_{413}$ (PtBS$_{26}$-*b*-PSSNa$_{413}$) SPB systems.[75, 119] Interestingly, the relative intensities of the first (F_1 at 372 nm) and the third (F_3 at 383 nm) bands in the pyrene emission spectrum at C_p >> CMC suggested that the polarity of the hydrophobic microenvironment (core)[108] of PBuA$_{35}$-*b*-PECVPD$_{30}$ micelles (F_3/F_1 = 0.85) is even slightly lower than for the PBuA$_{90}$-*b*-PAA$_{100}$ micelles (F_3/F_1 = 0.71) with longer hydrophobic segments.
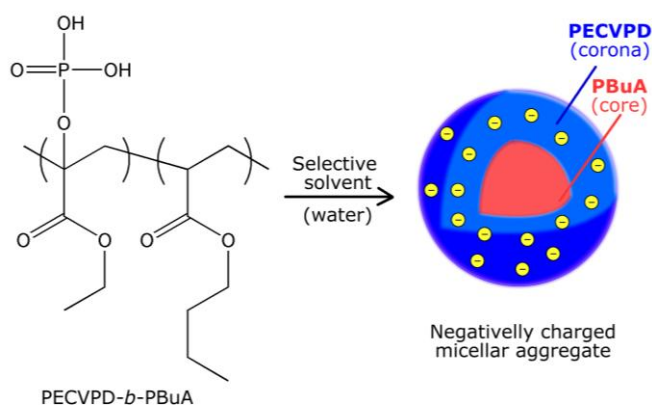
Scheme 4.2. Chemical structure and self-assembly behavior in aqueous media of the $PBuA_{35}$-*b*-$PECVPD_{30}$ diblock copolymer (M_n = 11 900 g/mol, M_w/M_n = 1.16, volume fraction of the PBuA hydrophobic segment ϕ_{PBuA} = 0.43).
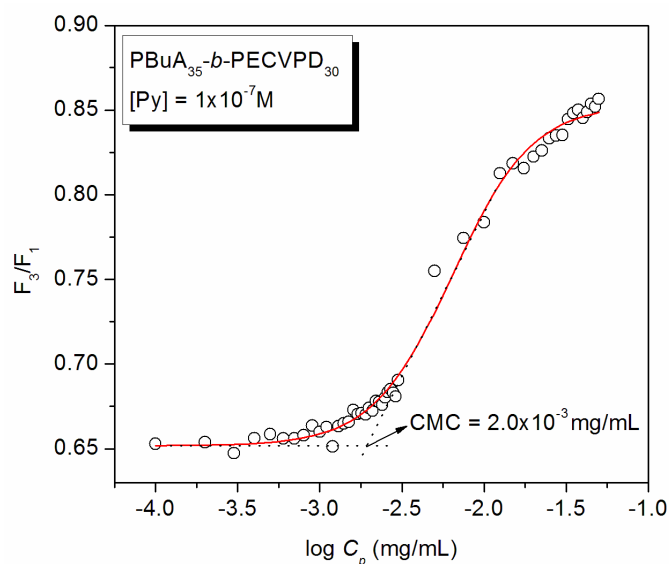
Figure 4.5. F_3/F_1 intensity ratios derived from pyrene emission spectra for PBuA-*b*-PECVPD copolymer solutions as a function of C_p, λ_{exc} = 335 nm.

The phosphonic diacid groups at the micelle corona exhibit two ionizable protons with distinct acid dissociation constants (K_a), as also observed for other substituted phosphate compounds containing labile protons. The pK_a (= -log(K_a)) for the first dissociation process is very low (pK_{a1} ~ 2.0 − 3.0), whereas the second deprotonation occurs at nearly neutral pH

conditions (pK_{a2} ~ 5.0 – 7.0). Therefore, the titration of PBuA$_{35}$-b-PECVPD$_{30}$ solutions can be modelled as follows

$$\text{H}_2\text{P} \underset{}{\overset{K_{a1}}{\rightleftharpoons}} \text{HP}^- + \text{H}^+ \underset{}{\overset{K_{a2}}{\rightleftharpoons}} \text{P}^{2-} + 2\text{H}^+$$

(eq. 4.1)
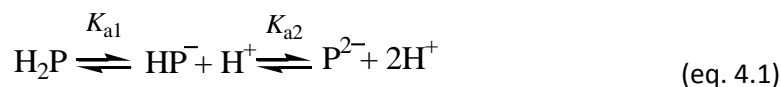
where H$^+$ is the proton (or hydronium ion), H$_2$P denotes the uncharged (protonated) block copolymer, and HP$^-$ and P^{2-} represent the corresponding chains formed by monomers with one or two negative charges each, respectively.

Potentiometric measurements were performed in order to gain insight into the pH effect on the effective number of charges on the micellar corona. The results (Figure 4.6) revealed that the first dissociation process takes place at pH < 3, being therefore not detectable in the titration curve (i.e., pK_{a1} < 3.0). Starting from pH = 3.0, the addition of small aliquots of NaOH increases the solution pH until a slightly pronounced buffering region is reached (shoulder), during which the added NaOH is consumed by the titration of the second proton on the ECVPD repeat units. Further addition of base merely elevates the solution pH. The estimated average pK_{a2} was 6.5. On basis of these results, the diagram of species distribution (Figure 4.7), and ultimately the variation in the total number of charges at the micelle corona, as a function of the solution pH can be calculated (Figure 4.8). At pH ≥ 4 at least one permanent negative charge is constantly present on each monomer unit of the PECVPD chain (HP$^-$ species), while at pH > 5 the fraction of fully ionized phosphate moieties (P^{2-} species) increases, so that at pH = 7.8 more than 95% of maximum deprotonation extent (dissociation degree) is attained. It is worth noting that such an information is of great relevance for the diblock copolymer nanoparticles herein investigated as far as it precisely defines the experimental conditions where variations in the effective micellar charge occur, for instance doubling from pH = 4.0 to 8.0. Besides, it allows the calculation of the actual number of negative charges per micelle provided that the aggregation number (N_{agg}) is known (see below).
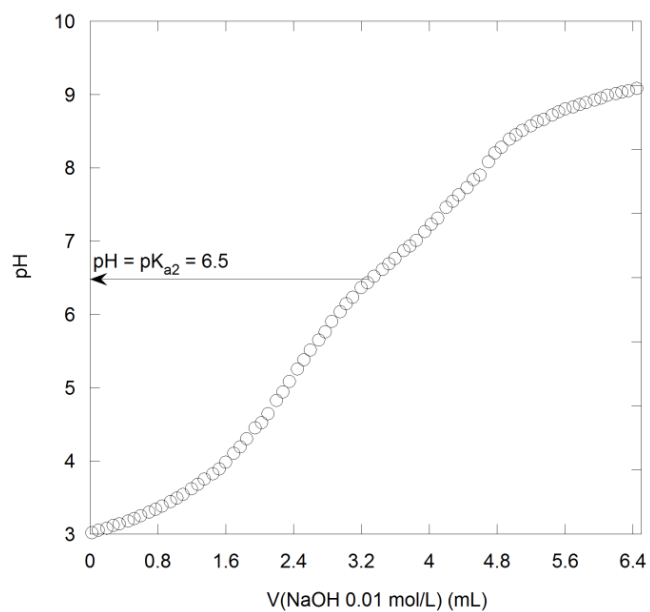
Figure 4.6. Potentiometric acid-base titration curves for 1.0 mg/mL PBuA-*b*-PECVPD copolymer solutions ($V_{aliquot}$ = 5.0 mL)
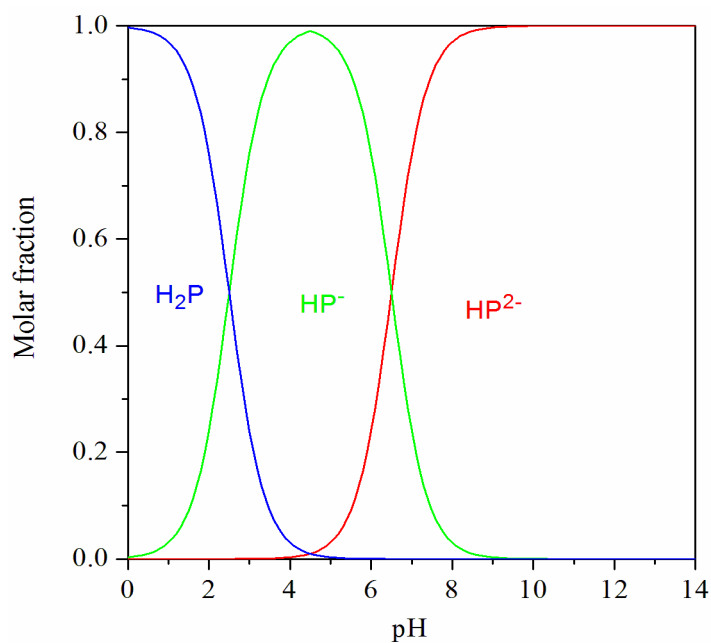
Figure 4.7. Diagram of species distribution as a function of the solution pH for a H_2P ionizable polymer with pK_{a1} = 2.5 and pK_{a2} = 6.5.
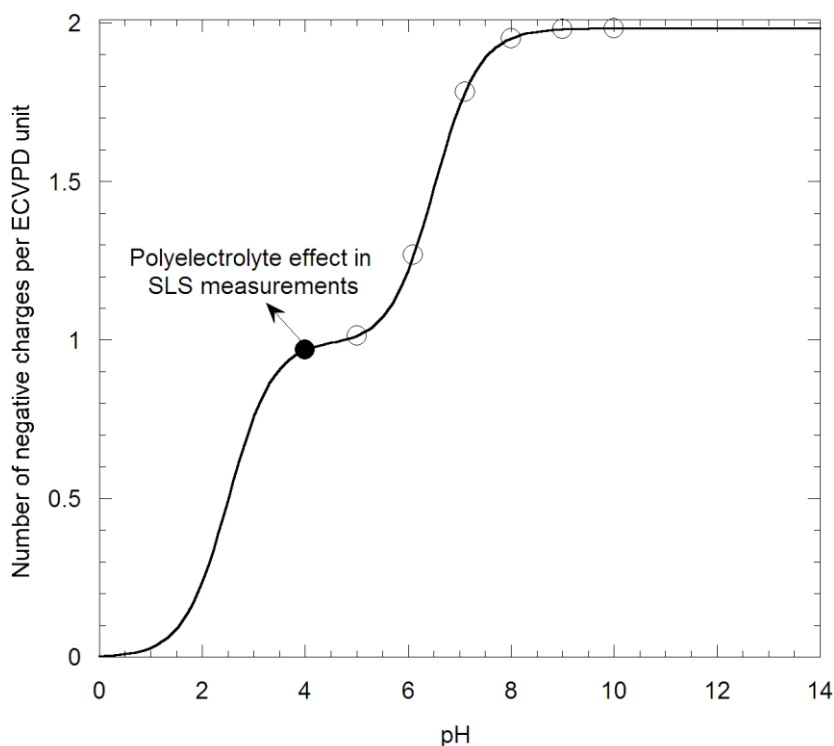
Figure 4.8. Number of negative charges per ECVPD monomer unit as a function of the solution pH. The circles correspond to pH conditions at which the systems were investigated.

Light Scattering

Figure 4.9 shows the variation of $KC_p/I(q)$ as a function of q^2 for 0.5 mg/mL micellar solutions containing different amounts of NaCl salt (C_s = 0 − 100 mM), as indicated. The characteristic solution pH measured for this sample was ~ 4.0, not being significantly influenced by C_s. Therefore, under these experimental conditions each monomer of the PECVPD chains has one permanent negative charge (Figure 4.8), and the particles dispersity is about μ_2/Γ^2 = 0.15 − 0.25, as estimated by cumulants analysis of $C(q,t)$ auto-correlation functions by DLS. In Figure 4.9, a steep negative slope was observed in absence of salt, indicating strong interparticle correlations. As C_s increased up to C_s ≤ 0.8 mM, the slope decreased progressively, then became positive for C_s > 2.0 mM, and finally remained increasing

slightly as C_s continued to increase. A virtually constant slope was evidenced for $C_s > 10 - 20$ mM. At this point, the electrostatic interactions (repulsions) within the micelle corona are presumably shielded by salt ions,[59, 77] so that further addition of salt practically did not affect the micelle structure. Such polyelectrolyte behavior was also confirmed by an abrupt increase in the scattered light intensity (I_{sc}) as a function of C_s (see below), in spite of the fact that micelle dimensions (corona thickness) decreased in presence of salt. The increase in I_{sc} reflected the higher mobility of scattering objects upon screening of electrostatic repulsions by counter-ions.[59, 65, 76, 77]

Negative slopes in $KC_p/I(q)$ vs q^2 curves were previously observed for linear polyelectrolytes in light scattering experiments.[77, 120] However, the results in Figure 4.9 are considered the first reported evidence for polyelectrolyte block copolymer micellar systems.
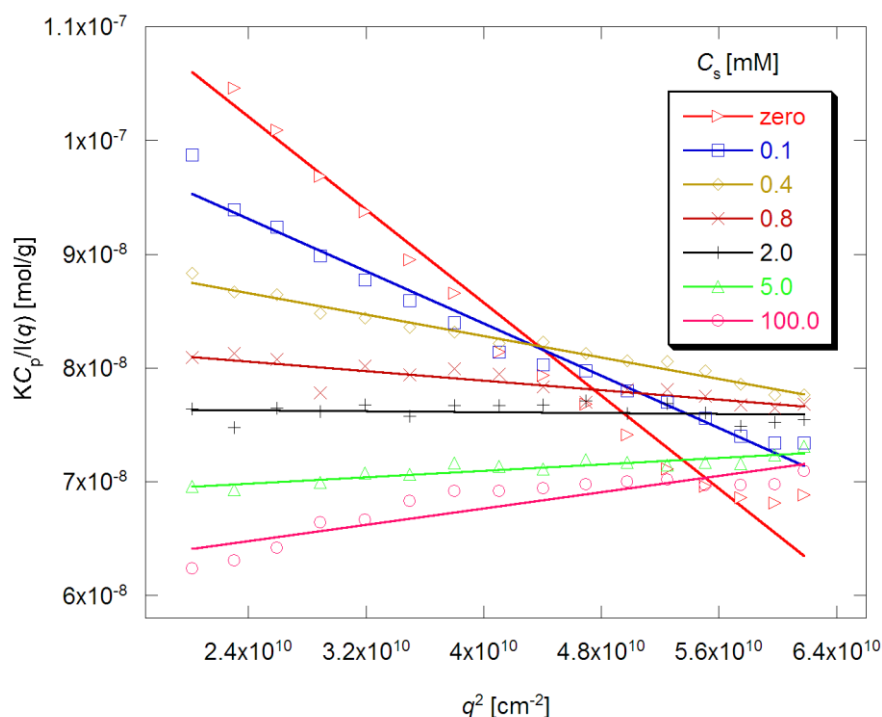
Figure 4.9. $KC_p/I(C_p,q)$ vs q^2 curves for 0.5 mg/mL PBuA$_{35}$-*b*-PECVPD$_{30}$ micellar solutions containing different amounts of NaCl salt.

Figure 4.10 describes the variation of the intercept $KC_p/I(q=0)$ as a function of C_s (i.e., the values of $KC_p/I(q)$ at $q = 0$ found from linear extrapolation of data in Figure 2, and the increase in the scattered light intensity (I_{sc}) as a function of C_s. It is worth noting that $KC_p/I(q=0) \cong 1/M_w$ $+ 2A_2C_p$ at $q = 0$ (classical Zimm equation). When the latter relation is applied to the PBuA$_{35}$-b-PECVPD$_{30}$ micellar system herein investigated, the left hand side term $1/M_w$ is a constant value as long as after micellization the M_w the micelles ($M_{w,mic}$) is not affect by changes in the ionic strength (see discussion below on SAXS data). Therefore, the decrease in $KC_p/I(q=0)$ observed in Figure 4.10 essentially reflects the decrease in the second virial coefficient (A_2) and in the radius of gyration (R_g).[77, 121] At high salt concentrations, A_2 is reduced by approximately half its initial value. It is possible, therefore, to distinguish the electrostatic portion of the A_2-value from the limiting A_2-value of residual highly screened (or "neutral") micelles. The overall profiles of $KC_p/I(q=0)$ vs C_s curves for PBuA$_{35}$-b-PECVPD$_{30}$ micelles and linear sodium hyaluronate are reasonably comparable.[77]
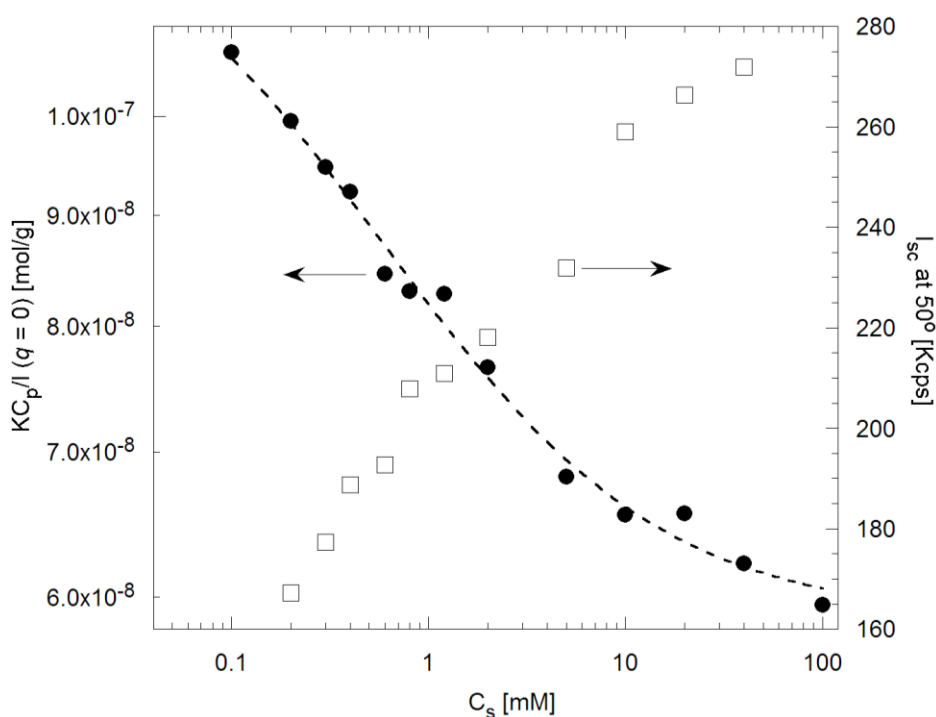
Figure 4.10. $KC_p/I(C_p,q=0)$ as a function of C_s for 0.5 mg/mL PBuA$_{35}$-b-PECVPD$_{30}$ micellar solutions.

The conformation and interactions of polyelectrolyte chains are strongly influenced by the addition of salt. In the case of SPBs such effects are particularly pronounced as long as the charged chains at the corona are more closely packed. Two regimes with characteristic brush thickness (corona width (W)) behavior can be distinguished for SPBs depending on the ratio between intrinsic brush counter-ion concentration ($C_{s,intr}$) and the added salt concentration (C_s).[69] In the so-called osmotic brush regime ($C_{s,intr} > C_s$) the changes in C_s have no effect on W, whereas in the salted regime ($C_{s,intr} < C_s$) W usually decreases with the increase in C_s, and this according to a $W \sim C_s^{-\beta}$ scaling law. Korobko et al.[122] have contemplated that the gradual contraction of charged micelles scales as $W \sim C_s^{-1/5}$, whereas other authors reported that a $W \sim C_s^{-1/3}$ dependence should be expected.[65, 69, 123, 124] Experimentally, β-values varying from 0.11 to 0.18 have been found for SPBs so far.[124]

The variation of the apparent hydrodynamic radius (R_H^{app}) as a function of C_s for 0.5 mg/mL micellar solutions is shown in Figure 4.11, where $R_H^{app} = W + R_c$ with R_c being the micelle core radius which is not influenced by the ionic strength (see hereinafter). Therefore, the variation in R_H^{app} as a function of C_s is ascribed to changes in W. In line with findings presented above, the results in Figure 4.11 also demonstrate that small amounts of salt provoke major changes in the macromolecular chain organization at the micelle corona, as judged from the rapid decreased in R_H^{app} from 57 to 41 nm as C_s increased from 0.1 to 1.0 mM. Further addition of salt did not influence the system. For 0.1 mM $\leq C_s \leq$ 1.0 mM, a $W \sim C_s^{-0.21}$ dependence is observed in Figure 4.11. This finding is in slightly better agreement with the expected value as compared to earlier reports on, for example, PS-based lattices with polyelectrolyte brushes at the surface ($W \sim C_s^{-0.17}$),[123] and block copolymer micelles made of poly(ethylethylene)$_{144}$-*b*-poly(styrene sulfonic acid)$_{136}$ (PEE$_{144}$-*b*-PSSH$_{136}$, $W \sim C_s^{-0.13}$)[75] and PtBS$_{27}$-*b*-PSSNa$_{757}$ ($W \sim C_s^{-0.11}$).[125]

For PBuA35-b-PECVPD30, the contour lengths of PBuA and PECVPD blocks would be about 8.8 and 7.5 nm, respectively, given the monomer contour length of 0.25 nm. So, the maximum length of the copolymer chain would be 16.3 nm. The favorable formation of larger-than-expected micelles is related to the chemical structure of segments forming the copolymer. Even though the PECVPD block is indeed soluble in water, the chemical similarity of pendant ester groups in both blocks (note: PECVPD has one ethyl ester and one phosphonic diacid pendant group in each repeat unit; PBuA has one pendant butyl ester group, see Scheme 4.2) may favor interactions, with consequent increase in the compatibility between the corona- and

the core-forming blocks (i.e., decrease in the Flory-Huggins interaction parameter (χ)), meanwhile still allowing the self-assembly. Combination of DLS & SLS shows a R_g/R_H ratio = 0.73, which is characteristic of spherical micelles. These experiments have been performed in the presence of salt (C_s = 50 mM), and are in perfect agreement with microscopy results (see below). The R_g cannot be estimated at C_s = zero (negative slope of $KC_p/I(q)$ vs q curves, Figure 4.9).
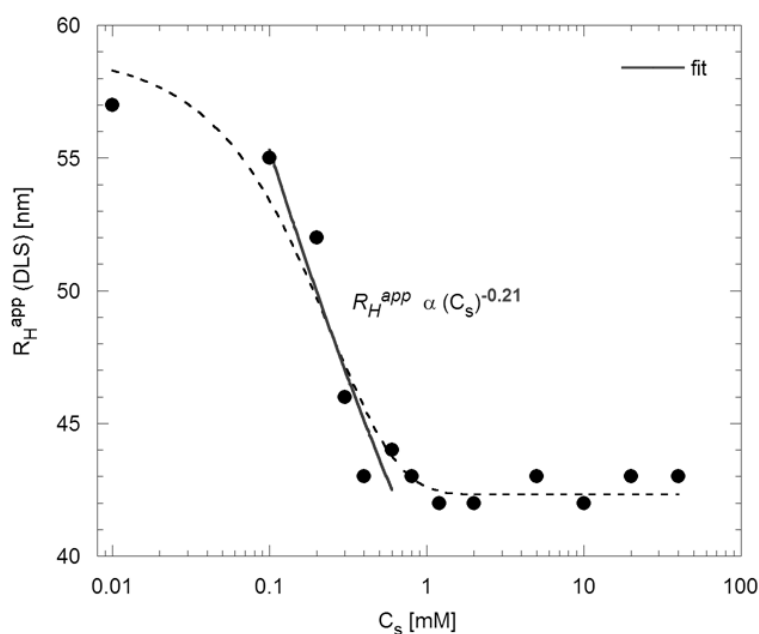
Figure 4.11. Apparent hydrodynamic radius (R_H^{app}) of PBuA$_{35}$-*b*-PECVPD$_{30}$ micelles as a function of C_s.

As outlined above, the density of negative charges at the micelle corona and consequently the scattering properties of the system depend on the solution pH and the ionic strength. The variation of the total scattered light intensity (I_{sc}) at 90° scattering angle and the number of charges on each ECVPD monomeric unit as a function of the pH are shown in Figure 4.12. The results reveal the existence of three different regimes in the I_{sc} vs pH plot, as indicated. Initially, (a) the I_{sc} decreases steeply by almost half its initial value as the pH is increased from 4.0 to 6.5 via addition of NaOH. Then, (b) a small decrease is also observed within the pH = 6.5 − 8.0 range. Finally, (c) the I_{sc} slightly increases for 8.0 < pH < 10.0 solutions.

The overall profile in Figure 4.12 reflects the increase in the negative charge density at the micellar corona due to the second deprotonation process of phosphonic diacid groups. The

enhanced interparticle electrostatic repulsions reduce the mobility of scattering particles, consequently lowering I_{sc} as well (regimes (a) and (b)). At pH $\geq$ 8.0 (regime (**c**)) the degree of acid dissociation is nearly quantitative (> 97%, Figure 1), and the influence of further addition of a strong base (NaOH) is similar to the salt effect (i.e., I_{sc} increases due to higher mobility of scattering objects upon screening of electrostatic repulsions by counter-ions). The data in Figure 4.12 also reveal an interesting feature regarding the transition from regimes (a) to (c). The interception of the linear fittings in those respective regions coincides at pH ~ pK_{a2}, a point at which the second deprotonation extent is 50%. To the best of our knowledge, such an observation has not been reported yet for weakly dissociating polymer brushes. Most likely, this behavior results from the balance of two opposing forces: the generation of charges at the micellar corona whose effect (I_{sc} decrease) is more pronounced in beginning of the process (i.e., at very low added NaOH concentrations; C_{NaOH} ~ 2 mM at pH = 6.5), and the inevitable increase in the ionic strength (I_{sc} increase) due to the addition of ionic species (Na$^+_{(aq)}$ and OH$^-_{(aq)}$; the latter is partially consumed during the neutralization reaction).
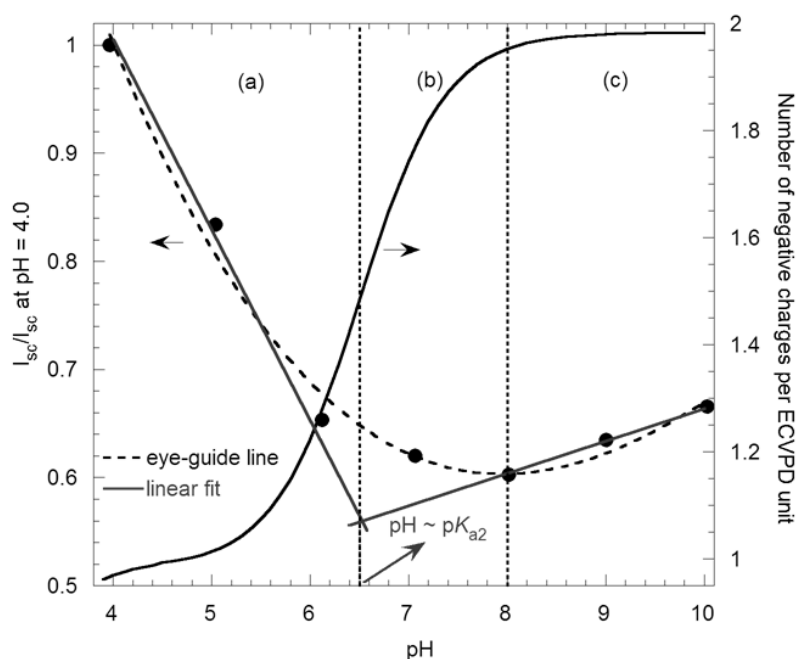
Figure 4.12. Variation of the total scattered light intensity (I_{sc}) as a function of the solution pH for 0.5 mg/mL PBuA$_{35}$-*b*-PECVPD$_{30}$ micelles.

Small Angle X-ray Scattering

The morphology and the interactions of negatively charged PBuA$_{35}$-*b*-PECVPD$_{30}$ micelles were investigated by small angle x-ray scattering (SAXS) experiments carried out at different polymer concentrations (C_p = 0.5 – 20 mg/mL) and added salt contents (C_s = 0 – 200 mM). Figure 6 shows a typical SAXS intensity profiles obtained at different C_p without added salt (C_s = zero), as indicated. At a glimpse, different structural levels can be qualitatively observed: in the high-*q* region the complex internal structure of the micelle is manifested, which provides the micelle core size ($R_c \approx$ 21nm); for C_p > 2.5 mg/mL at intermediate *q,* a correlation peak due to micelle-micelle interactions can be observed at $q = q^*$; furthermore, in the low-*q* region permanent clusters give rise to the upturn in all the scattering patterns.

At high charge and minimal screening conditions, the polyelectrolyte chains remain almost fully stretched and they interdigitate.[122, 126] Meanwhile, C_p was found to have practically no influence on the micellar dimensions, as judged from the high-*q* SAXS data shown in Figure 4.13. Indeed, the *I(q)* minima at q ~ 0.2 nm^{-1}, which are related to the characteristic form factor and size of spherical scattering objects, practically do not shift within the C_p = 1.0 – 20.0 mg/mL range.
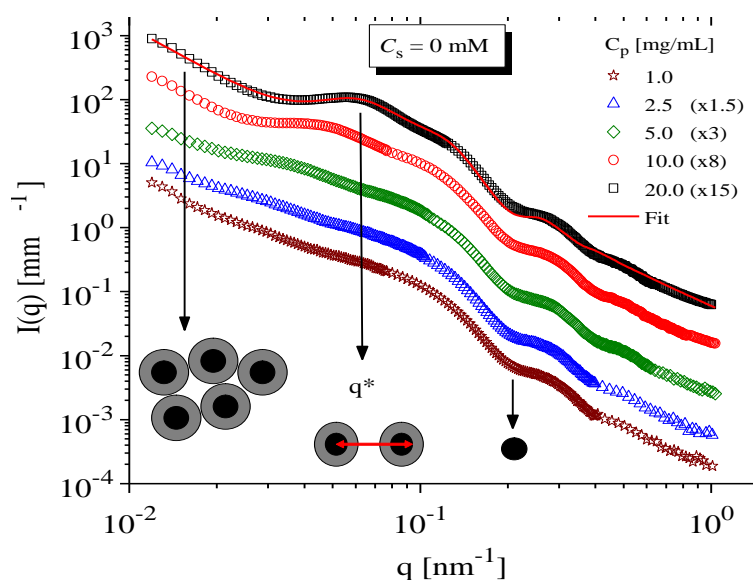
Figure 4.13. SAXS intensity profiles for PBuA$_{35}$-*b*-PECVPD$_{30}$ solutions at different copolymer concentrations (C_p) in absence of salt. A cartoon showing the different structures observed in

solution is also reported. The solid line indicates best fit to eq (2.34) for C_p=20 mg/mL. For clarity, the SAXS patterns are rescaled by the factor indicated in the legend.

For C_p< 2.5 mg/mL, the SAXS intensity profiles can be fitted using eq. (2.27) (2.29) and (2.34) assuming $S(q) \approx 1$. Figure 4.14 shows the experimental SAXS data and fitting results (continuous lines) for spherical PBuA$_{35}$-b-PECVPD$_{30}$ micellar nanoparticles at C_p = 1.0 mg/mL in absence and in presence of C_s = 100 mM. In both cases, good agreement between experimental data and fitted curves is obtained. The resulting fit parameters revealed that changes in the ionic strength after micellization do not influence the core radius (R_c), which is essentially the same ($R_c \sim$ 21 nm) in absence of added salt (C_s = zero) and at high salt concentrations (C_s = 100 mM). Lack of significant changes in the micellar form factor upon addition of salt also revealed that the corona is nearly contrast matched with the solvent. The addition of salt causes a decrease in the aggregates (clusters) size from R_g = 277 nm at C_s = zero down to R_g = 239 nm at C_s = 100 mM, as a result of electrostatic charge screening by counter-ions leading to less stretched (because of repulsive Coulomb forces) corona-forming segments. The limited q-range of the data excludes a precise determination of the radius of gyration of the clusters R_g, and their fractal dimension d_f.
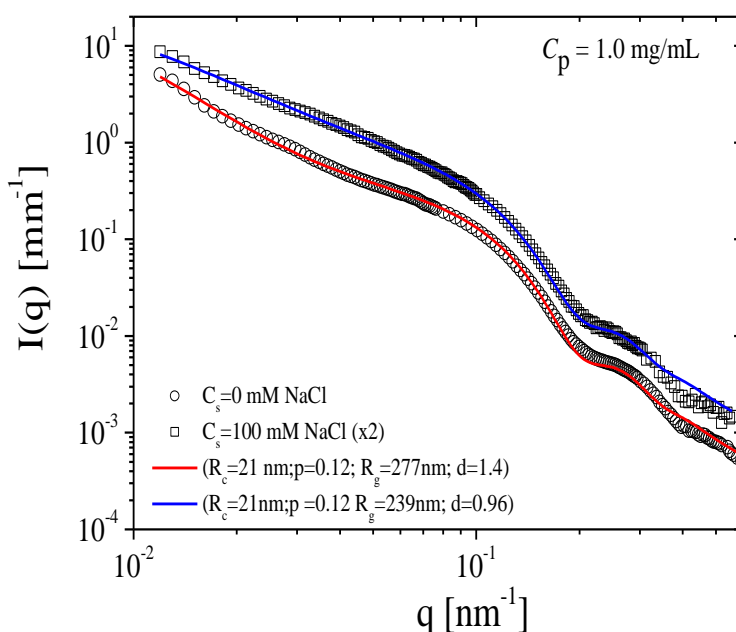
Figure 4.14. SAXS intensity profiles fitted using a polydisperse core-shell model (continuous lines) for spherical PBuA$_{35}$-b-PECVPD$_{30}$ micellar nanoparticles at C_p = 1.0 mg/mL in absence (open

circles) and in presence of salt C_s = 100 mM (open squares). The parameters of the fits are also reported. For clarity, the data in presence of salt are rescaled by the factor indicated in the legend.

In Figure 4.15 the comparison between the two extreme conditions (minimal and high screening) is shown for C_p=20 mg/mL (above c*). The fits to eq. 2.34 show a decrease of the effective diameter σ (which takes into account the contribution of hard core, the impenetrable shell and the range of electrostatic interactions) from σ = 95 nm down to σ = *58* nm as consequence of the changes in the corona size and electrostatic interaction range with the addition of salt. The position of the minimum in the scattering patterns (q ~ 0.2 nm^{-1}) suggests that no changes are observed in the core size upon addition of salt. This result strongly suggests that N_{agg} is not affected by C_s. Moreover, it is very interesting to relate the changes in the effective volume fraction (from 0.17 to 0.04 as salt content increases from 0 up to 100 mM NaCl) with the decrease of R_H, reported in Figure 4.11 as a function of salt concentration. Knowing that $\varphi = N_p V$, we can attribute the changes in the effective volume fraction to partly the shrinking of the corona upon addition of salt [the value of 4.3 for the ratio between the volume fractions in absence and presence of salt as compared to the ratio between the effective hydrodynamic volumes, i.e. $(R_{H, Cs=0}/R_{H, Cs = 100\ mM})^3$ ~ 2.6]. The remaining part can be attributed to the change in electrostatic interactions. Therefore, SAXS analyses correlate well with the DLS results, in spite of the fact that the salt effect seems to be more pronounced in the latter case.
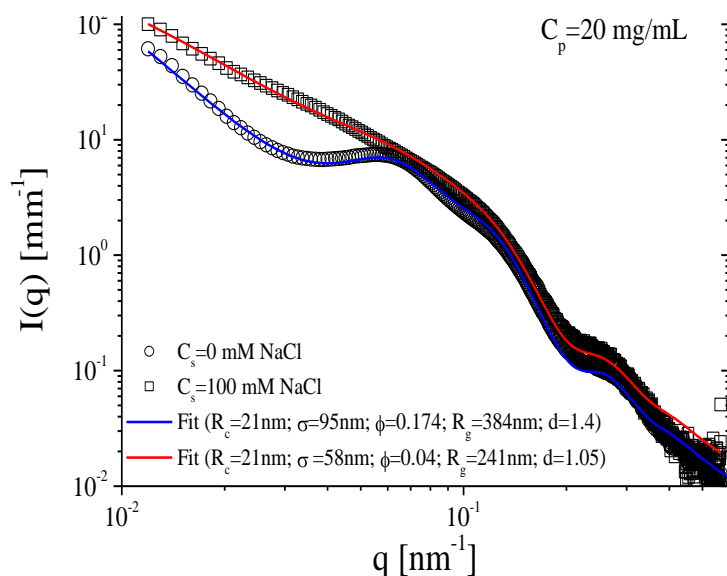
Figure 4.15. SAXS intensity profiles for PBuA$_{35}$-*b*-PECVPD$_{30}$ solutions at C_p = 20.0 mg/mL in absence (open squares) and in presence of salt C_s = 100 mM (open circles). The best fits to eq. 2.34 are also shown. In the legend, the parameters of the fits are reported.

Cryo-TEM experiments

Cryo transmission electron microscopy analysis was performed on selected micellar solutions in order to verify the morphology of self-assembled structures. This technique is capable of imaging nanostructures in thin films of vitrified aqueous solutions, thus ideally preserving the sample characteristics in solution. The Cryo-TEM images of PBuA$_{35}$-*b*-PECVPD$_{30}$ micelles in absence and in presence of added salt shown in Figure 4.16 confirm the spherical shape of the micelles obtained by SAXS (see also TEM micrograph in Figure 4.17, and low magnification cryoTEM micrographs in Figure 4.18). Because of the low contrast as in SAXS of the diffuse corona in water, only the core is seen in both cases, as previously reported for PBuA-*b*-PAA micelles[127] and PSS/PS lattices.[128] It is straightforwardly verified that the characteristic R_c is not affect by the ionic strength (R_c-TEM $\cong$ 20 nm in Figure 4.16a and 4.16b), being entirely in agreement with findings discussed above (Figure 4.14). Micrographs taken in presence of salt (Figure 4.16b) systematically revealed the presence of small dark points. Such an effect was previously observed by other authors,[69, 127, 129] and is attributed to the salt-

induced shrinking of corona chains into a few compact strands. Consequently, higher electron scattering areas (darker spots) are seen.
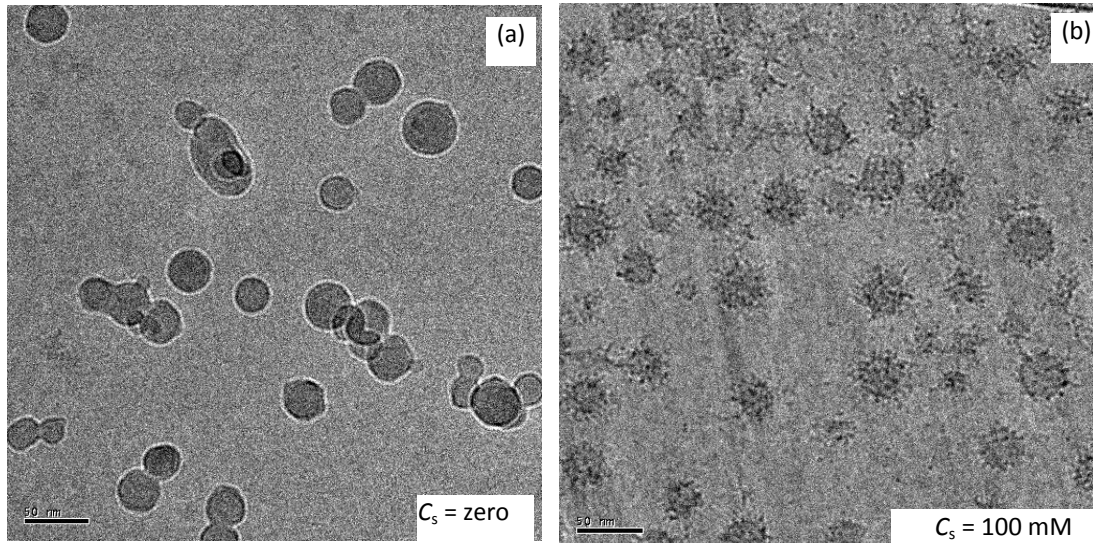
Figure 4.16. Cryo-TEM images of PBuA$_{35}$-*b*-PECVPD$_{30}$ micelles in absence (a) and in presence of salt C_s = 100 mM (b). The scale bar is 50 nm.
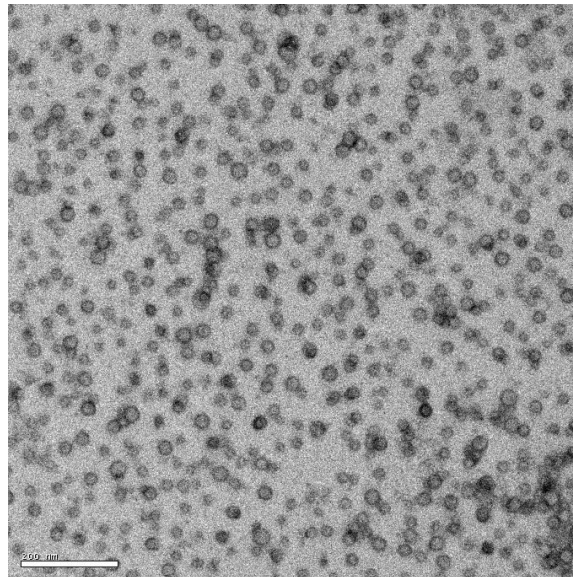
Figure 4.17. TEM micrograph of 0.5 mg/mL PBuA-b-PECVPD micelles in absence of added salt, and negatively stained with 2% sodium phosphotungstate solution at pH 7.4. (Scale bar = 200 nm).
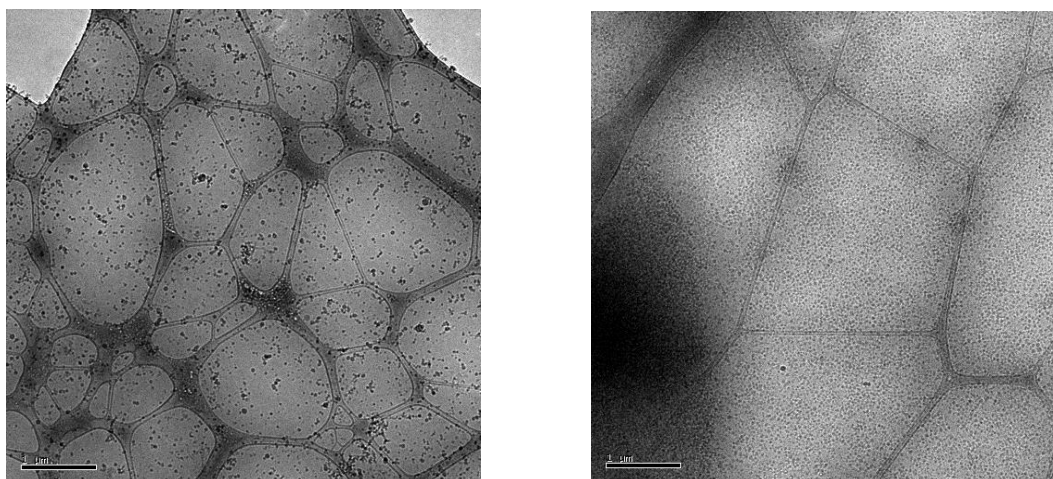
Figure 4.18. Cryo-TEM images of PBuA-*b*-PECVPD micelles at low magnification in absence (left) and in presence of salt C_s = 100 mmol/L (right).

4.3.   Annexin-A5 binding onto PBuA$_{35}$-b- PDECVP$_{30}$ micelles

As observed in DLS experiments summarized in Figure 4.19(I), the self-assembly of PECVPD-*b*-PBuA copolymer in pure water (no added salt) originated two distinct relaxation times of well-defined spherical nano-objects (also identified in cryo-TEM (Figure 4.19(IIA)) and TEM micrographs (Figure 4.20)), whose apparent hydrodynamic diameters ($2R_H^{app}$) were 8 and 110 nm (curve A). Upon salt addition (either NaCl or CaCl$_2$) (curve B), one single relaxation relaxation time was observed corresponding to a size of $2R_H$ = 78 nm. Such a decrease was also confirmed by cryo-TEM (Figures 4.19(IIB)). The addition of 1.3 mg/mL Annexin-A5 in a buffer solution (20 mM Tris-HCl, pH 8.0, 0.02% NaN$_3$, ~200 mM NaCl) to a 0.5 mg/mL PECVPD$_{30}$-*b*-PBuA$_{35}$ micellar solution in presence of 50 mmol/L NaCl did not provoke noticeable changes in both particle size and distribution profile (curve C). Under these experimental conditions, negatively charged phosphate groups are exposed at the corona/solvent (water) interface, with no detectable interaction with the protein.

Binding of Annexin-A5 onto PECVPD-b-PBuA micellar aggregates was achieved by adding 2.0 mmol/L CaCl2 (close to physiological content) (curve D), thus originating (bio)functionalized polymer-based assemblies, as demonstrated by DLS (Figure 4.19.I), cryo-TEM (Figure 4.19.II) and Quartz Crystal Microbalance with Dissipation monitoring (QCM-D) (Figure 4.23) experiments. According to DLS results, this phenomenon caused a 40-nm increase in the mean diameter-value (from 78 nm – curve B/C – to 120 nm – curve D). Such a large size increase was

further confirmed by cryo-TEM images (Figures 4.19.IID)), and suggested the migration of Annexin-A5 into the micelle corona, in a process favored by the existence of phosphate groups along the micelle corona. The protein binding efficiency determined by SLS after separation of unbound protein by ultracentrifugation was higher than 85% (Figures 4.21 and 4.22). The accessibility of pendant phosphonic diacid moieties in the polymer backbone is almost quantitative, as judged by potentiometric acid-base titration curves (Figure 4.20). This behavior was quite different when compared to Annexin-A5/liposome systems, for which the size-shift due to protein surface binding was virtually equivalent to a protein monolayer thickness (2x4 nm), owing to the fact that liposomes exhibit phosphate moieties exposed at their periphery (Scheme 3.1). The slow relaxation mode in curve D was attributed to large aggregates in solution, possibly induced by protein interaction connecting different particles, since Annexin-A5 has multiple potential Ca^{2+} binding sites.[5a]

The addition of EGTA (a Ca^{2+}-selective chelating agent) to solutions containing Annexin-A5/micelle assemblies resulted in a clear decrease in the size (curve E in Figures 4.19(I)) as a result of Annexin-A5 release from the micelle.

The Annexin-A5 binding efficiency onto PECVPD-*b*-PBuA micellar nanoparticles was estimated by elastic light scattering in dilute regime after separation of unbound protein by ultracentrifugation. Figure 4.21 shows selected results illustrating effect of centrifugation parameters (speed and temperature) on the sedimentation process. It has been observed that protein-decorated nanoparticles still remain in solution when centrifuged at 13,200 rpm and 25 °C during 15 min (curve B), as judged from the distribution of relaxation times A(t) obtained by DLS for the supernatant. However, a huge decrease in the scattered intensity occurred (see values inset), suggesting partial sedimentation. On the other hand, when submitted to centrifugation at 75,000 rpm and 4 °C during 15 min, protein-decorated particles sediment completely, and only a single relaxation process is observed for the supernatant (curve C). The corresponding R_H values are characteristic of unbound Annexin-A5 protein ($2R_H = 5.0 - 6.0$ nm). This observation is in total agreement with previous experiments (not shown) presenting no sedimentation in pure Annexin-A5 solutions under the same experimental conditions. Thus, unbound protein and protein-decorated nano-particles could be separated as illustrated in curves C and D.
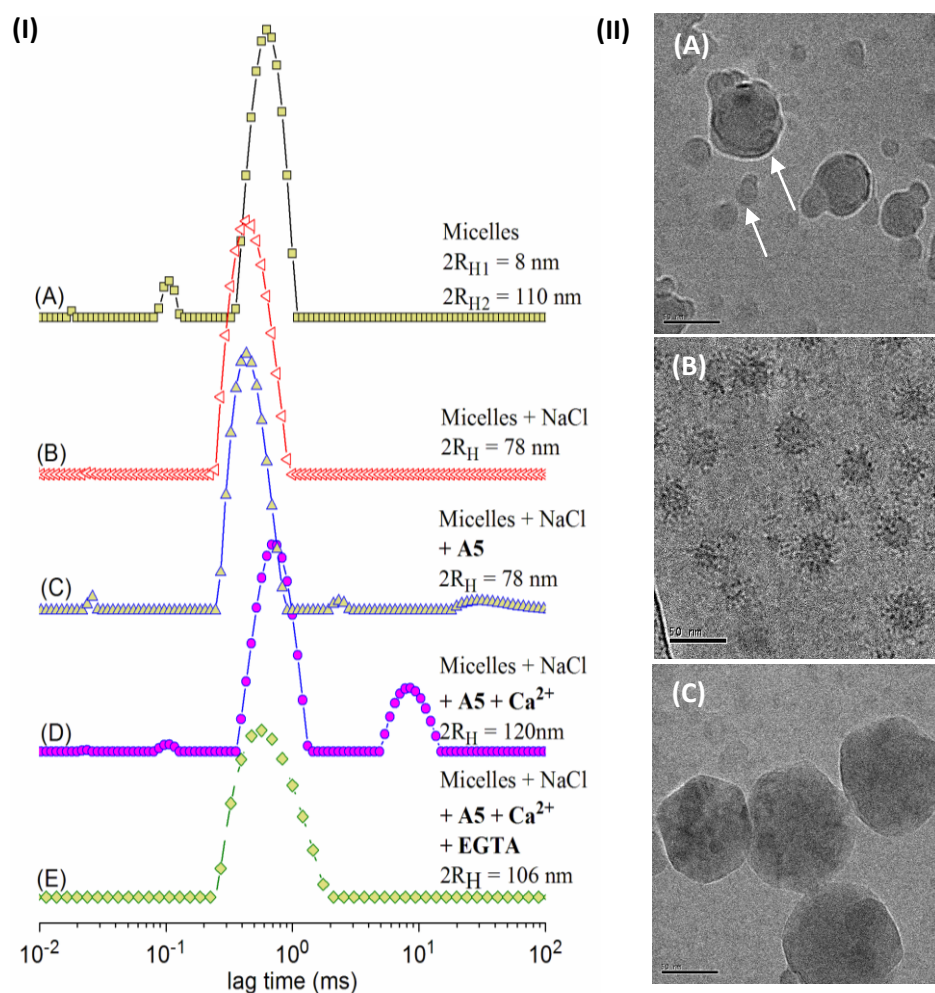
Figure 4.19. (I) Distribution of relaxation times A(t) obtained using CONTIN analysis of autocorrelation functions C(q,t) (DLS) recorded during preparation steps of protein (Annexin-A5)-decorated diblock copolymer micellar aggregates. In all cases, the relaxation frequency ($\Gamma = \tau$-1) is q2-dependent (q is the wavevector) (II) Cryo-TEM images corresponding to solutions A, B and D in Scheme 4.3 and Figure 4.19(I) (scale bar: 50 nm).
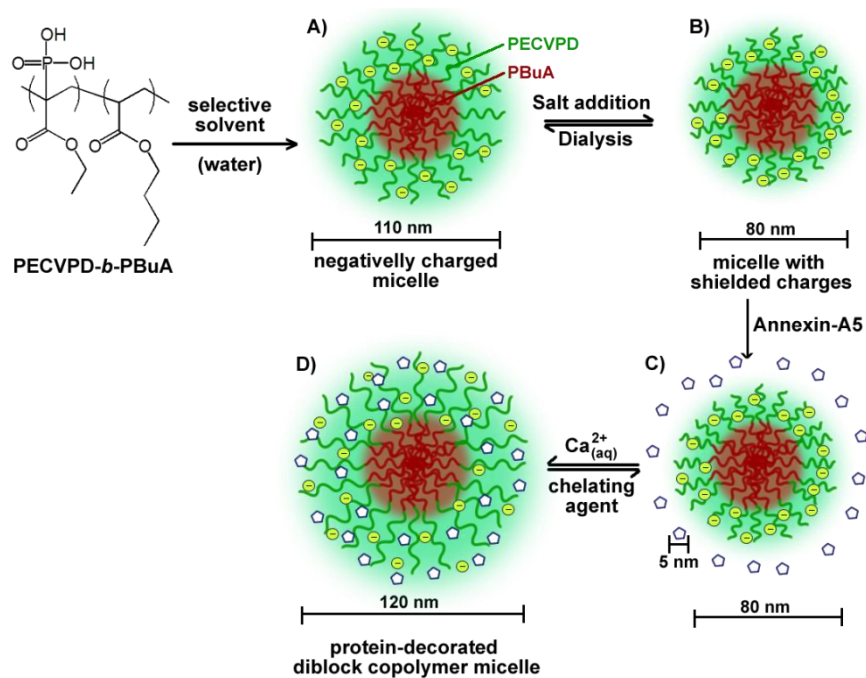
Scheme 4.3. Successive steps during the formation of PECVPD-*b*-PBuA micellar aggregates in water, and their protein decoration.
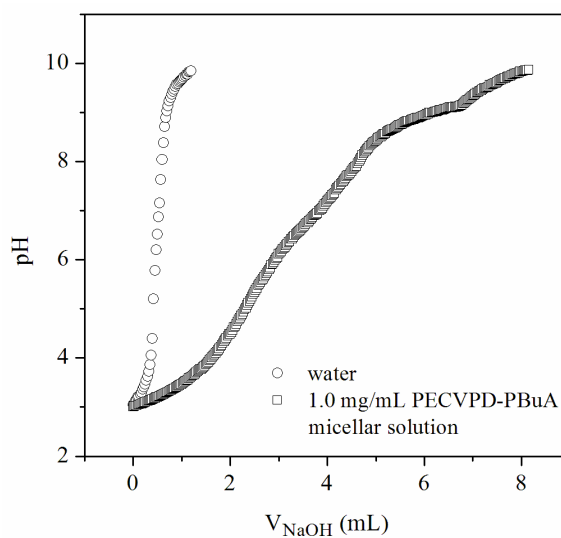
Figure 4.20. Potentiometric acid-base titration curves for a 5.0 mL aliquot of 1.0 mg/mL PECVPD$_{30}$-*b*-PBuA$_{35}$ micellar solution in water (titrant was 0.01 mol/L NaOH). For the sake of comparison, titration of the solvent (water) is also shown. This experiment indicated that the number of added NaOH equivalents added up to the titration end-point is close to the total amount of ionizable phosphate groups in solution.

We elected to take advantage of such a behavior to estimate the protein concentration in the supernatant recovered after ultracentrifugation at 75,000 rpm and 4 ^{o}C during 15 min. The method of choice in the present work was elastic light scattering. In the dilute regime, the total average light scattered intensity varies linearly with respect to the concentration, as depicted in Figure 4.22 where variation of the normalized intensity $I_{sc}^{N}(\theta = 90)$ is plotted against [Annexin-A5]. The amount of Annexin-A5 remaining in the supernatant was thus estimated using this analytical curve. By employing this procedure, the protein binding efficiency was higher than 85% in 0.5 mg/mL PECVPD-*b*-PBuA micellar solution in presence of 50 mmol/L NaCl, 1.3 mg/mL Annexin-A5 and 2.0 mmol/L CaCl$_2$.
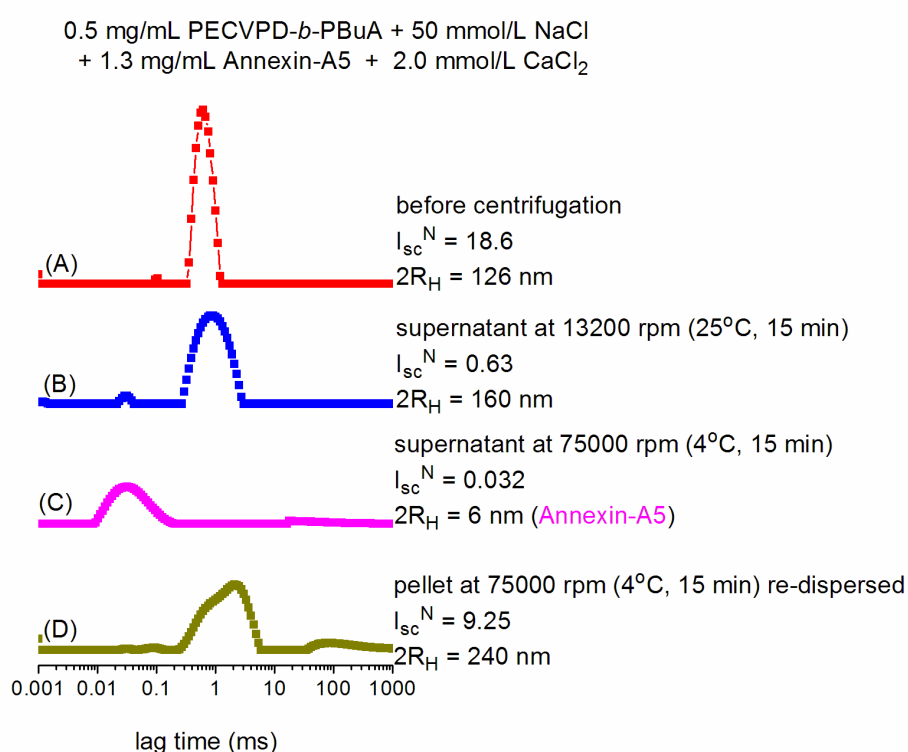
Figure 4.21. Distribution of relaxation times at 90° scattering angle obtained for protein-decorated solutions before (A) and after centrifugation under different conditions (C, B) and for a re-dispersed pellet (D).
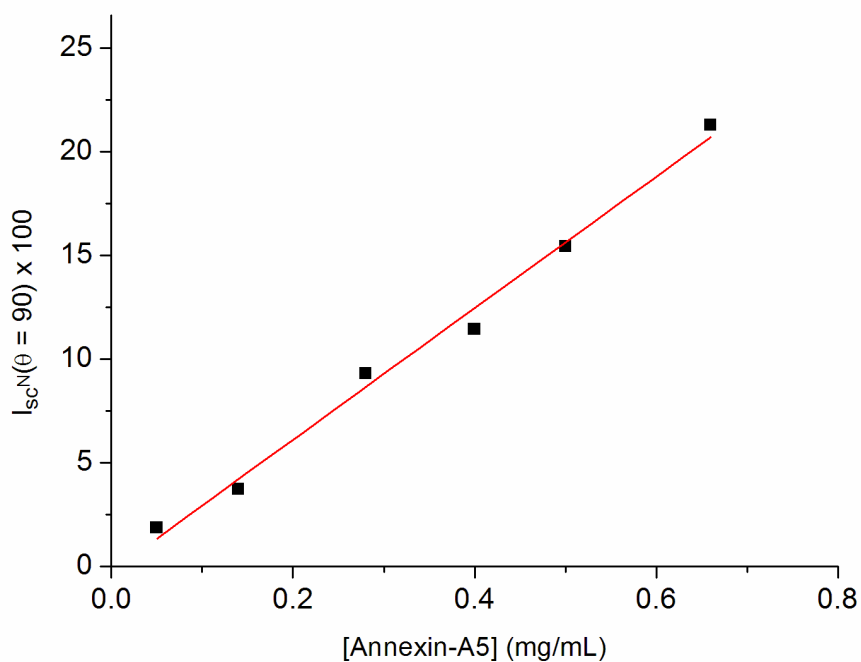
Figure 4.22. Analytical curve of Annexin-A5 in aqueous solution containing 50 mmol/L NaCl and 2.0 mmol/L $CaCl_2$ as measured by elastic light scattering.

Similarly, QCM-D measurements revealed variations in the resonance frequency and dissipation values upon addition of PECVPD-*b*-PBuA micellar solution to a monolayer of chemically engineered "double" Annexin-A5 molecules (Figure 4.23(C)). The same behavior could be evidenced when Annexin-A5 was added to a layer of deposited micelles (Figure 4.23(D)). These assembled objects were stable, and not affected by rinses. As for DLS, disassembly occurred when a chelating agent was added (Figure 4.23(E)).
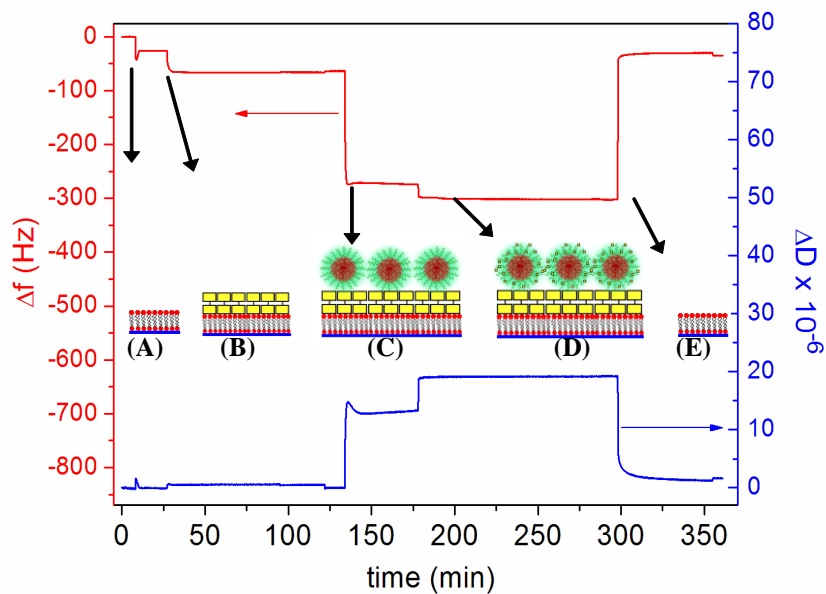
Figure 4.23. QCM-D data showing the formation of Annexin-A5/PECVPD-*b*-PBuA complexes, as follows: (A) deposition of a lipid bilayer, (B) deposition of A5 dimers; (C) after addition of PECVPD$_{30}$-*b*-PBuA$_{35}$ micellar solution; (D) further addition of Annexin-A5, (E) after addition of EGTA. Solutions B-D contained 2.0 mmol/L CaCl$_2$

Chapter 5

PS-*b*-P(PEMA-co-HEMA)

micelles decorated with Annexin-A5

5.1.   Copolymer Synthesis and Characterization

In a series of preliminary studies, we have addressed the ATRP of 2-phospatethyl methacrylate (PEMA) monomer in aqueous media at pH = 7.0 using Cu/bpy catalyst and the hydrophilic initiator 1-*O*-(2'-Bromo-2'-methylpropionoyl)-2,3-glycerol. The results indicated that polymerization practically did not proceed. Alternatively, the use of silyl-protected PEMA monomer – obtained from its reaction with hexamethyldisilazane (HMDS) – allowed polymerization to occur up to conversions as high as 80%, and originated good first-order kinetic plots (ln $[M]_0/[M]$ *vs.* time). However, upon exposure to air, the reaction mixture rapidly gelified forming an insoluble material in most of the solvents. Essentially the same observations were described recently by Suzuki *et al.*[130], who polymerized PEMA by reversible addition-fragmentation chain transfer (RAFT).

Another approach to phosphorus-containing polymers is simple phosphorylation of hydroxylated polymeric chains. In such a case, macromolecules with precise composition, architecture and narrow molecular weight distribution – all important features to obtain well-defined nano-assemblies – can be used as precursors, therefore allowing the preparation of phosphorylated derivatives with similar dimensions. On this basis, phosphorous-containing amphiphilic block copolymers showing ability to self-assemble into nano-objects capable of binding to Annexin-A5 proteins were synthesized as illustrated in Scheme 5.1

Firstly, polystyrene (PS) macroinitiators (**1**) were synthesized by ATRP of styrene in bulk at 100°C initiated by α-bromoisobutyryl bromide in presence of Cu/PMDETA catalyst, as previously described elsewhere by Matyjaszewski *et al.* [131]. Polymers with narrow molecular weight distributions ($M_w/M_n \leq 1.06$) were obtained as listed Table 4.1. These PS samples were subsequently used to initiate the ATRP of hydroxylated monomers in polar organic solvents.

Two distinct monomers have been tested in this work, namely 2-hydroxyethyl methacrylate (HEMA) and glycerol monomethacrylate (G2MA). HEMA has been chosen because of its single pendant hydroxyl group, which is suitable for later phosphorylation reactions, as well as the existence of documented data on its polymerization in organic media [132], where PS is equally soluble. In fact, HEMA (and G2MA) cannot be polymerized by anionic and group transfer

Therefore, PS-*b*-PHEMA amphiphilic diblock copolymers (**2**) were synthesized in MEK/1-propanol 70/30 (v/v) at 50°C using Cu/bpy catalyst, as illustrated in Scheme 5.1. Under these experimental conditions, well-defined diblock copolymers were obtained, and their

macromolecular characteristics are summarized in Table 5.2. The initiation efficiency of this system was, however, not quantitative provided that unreacted PS chains were persistently detected by GPC analyses of crude samples (Figure 5.1). Such behavior was observed previously, for example, for the ATRP of butyl acrylate (BuA) initiated by PS, but in those cases efficiency could be improved by adjusting the activator/deactivator concentrations. In the present work, little effect on the initiation efficiency was observed by varying CuBr (activator) and/or CuBr$_2$ (deactivator) concentrations, even though the ratio between PS-*b*-PHEMA and PS peaks was improved (data not shown). Instead, PS-*b*-PHEMA diblocks free of unreacted PS chains were successfully obtained by selective precipitation from acetone into heptane at room temperature. Under these circumstances, short chains of PS homopolymer remain soluble in the medium, whereas PS-*b*-PHEMA precipitates as a white solid. Indeed, after repeating this procedure for three times, no signal of PS was observed, as evidenced in Figure 5.1.
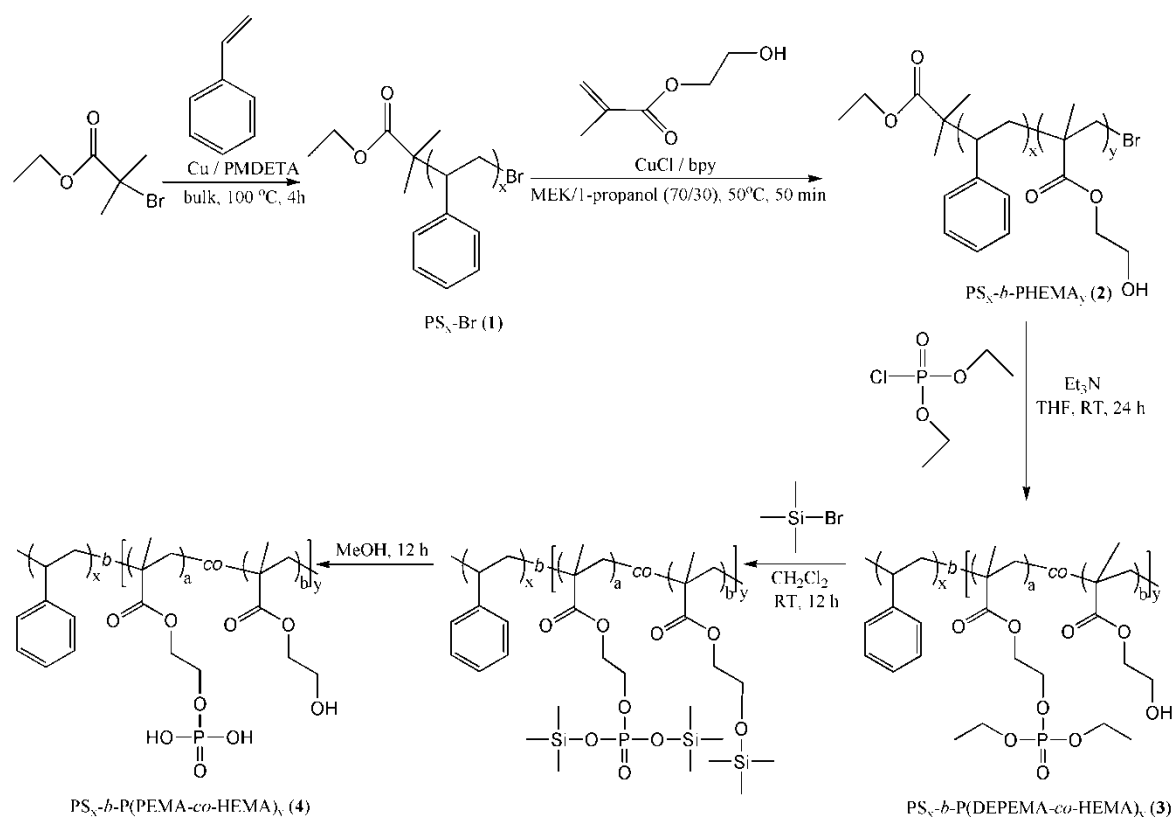
Schme 5.1. Synthesis phosphorylated amphiphilic PS-*b*-P(PEMA-*co*-HEMA) copolymers.

Table 5.1. Molecular characteristics of PS-Br macroinitiators prepared by ATRP[a].

Macroinitiator	time (h)	Conv. (%)	M_n (target)[b] g/mol	M_n (theo)[c] g/mol	M_n (GPC)[d] g/mol	M_w/M_n[d]
PS$_{30}$-Br	4.0	60	5,400	3,300	3,000	1.05
PS$_{55}$-Br	6.0	70	7,500	5,300	5,700	1.06

[a] Conditions: bulk polymerization at 100°C; [S]/[EBriBu]/[CuBr]/[bpy] = 50/1.0/0.5/0.5 or 70/1.0/0.5/0.5.
[b] At quantitative monomer conversion.
[c] Calculated based on the conversion estimated by ^{1}H NMR in CDCl$_3$.
[d] Determined by GPC measurements in DMF with PS standards.
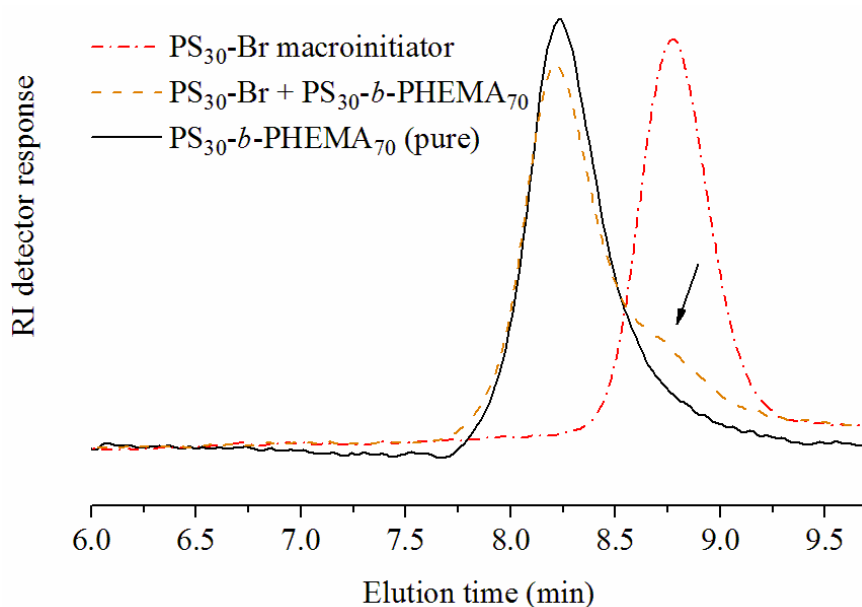
Figure 5.1. GPC traces of the PS$_{30}$-Br macroinitiator, the resulting products of PS chain extension by ATRP of HEMA before selective precipitation, and purified PS$_{30}$-b-PHEMA$_{70}$ diblock copolymer.

Table 5.2 shows narrow molecular weight distributions ($M_w/M_n \leq 1.15$) for PS-*b*-PHEMA diblocks, which are the precursors of the phosphorylated polymers. This is indeed a very important characteristic of such samples, particularly because they are to the used as bottom-up building blocks to prepared self-assembled structures, and the polydispersity is known to potentially affect not only the size but also the morphology of the nano-objects. The number average molecular weight (M_n) calculated from ^{1}H NMR (M_n(NMR)) or determined by DMF GPC (M_n(GPC)) analysis are noticeably higher than the expected values (M_n(theo)). The overestimated M_n(GPC)-values are attributed to the differences in hydrodynamic volumes

between PS-*b*-PHEMA diblocks and PS homopolymer standards used in the calibration of GPC apparatus. Hence, M_n(NMR)-values were taken to interpret the results hereafter, being calculated from

$$Mn(NMR) = \left[\frac{DP(PS)_{GPC}}{\frac{A(2.4 - 1.2\,ppm) - 2H(HEMA)}{3H(S)}} \right] x\,FW(HEMA) + \left[DP(PS)\,x\,FW(S) \right] \qquad \text{(eq. 5.1)}$$

where *DP*(PS)$_{GPC}$ is the degree of polymerization of PS block extracted from GPC measurements (PS standards), A(2.4 − 1.2 ppm) is the integral area between the indicated chemical shifts when A(4.2 − 3.4 ppm) = 4.00 (4H of ethyl group of HEMA), *FW*(HEMA) and *FW*(S) are the formula weight of HEMA and Styrene monomers, respectively. The regions of interest are indicated clearly in Figure 5.2, which shows the assinged NMR spectra of PS macroinitiator (A), PS-*b*-PHEMA copolymer before (B) and after (C) phosphorylation using diethyl chlorophostate (D).

Table 5.2. Characteristics of PS-*b*-PHEMA diblock copolymer precursors prepared by ATRP.

PS$_x$-*b*-PHEMA$_y$ x-y	time (min)	Conv. (%)	M_n (target)[a] g/mol	M_n (theo)[b] g/mol	M_n (NMR)[c] g/mol	M_n (GPC)[d] g/mol	ϕ_{PS}[e]	M_w/M_n[d]
30-70	50	70	8,300	6,700	12,200	34,800	0.26	1.15
55-145	120	88	16,200	14,900	24,600	50,000	0.23	1.14

[a] At quantitative monomer conversion assuming complete chain extension.
[b] Calculated based on the conversion estimated by ^{1}H NMR in DMSO-d_6.
[c] Determined by ^{1}H NMR measurements in DMSO-d_6 using the ratio between methacrylic (PHEMA) and polymer backbone (PS + PHEMA) protons (eqn. 5.1).
[d] Determined by GPC measurements in 1.0 g/L LiBr DMF at 60°C with PS standards.
[e] Volume fraction of PS in the resulting polymer, assuming that the densities are equal to 1.0 g/mL.
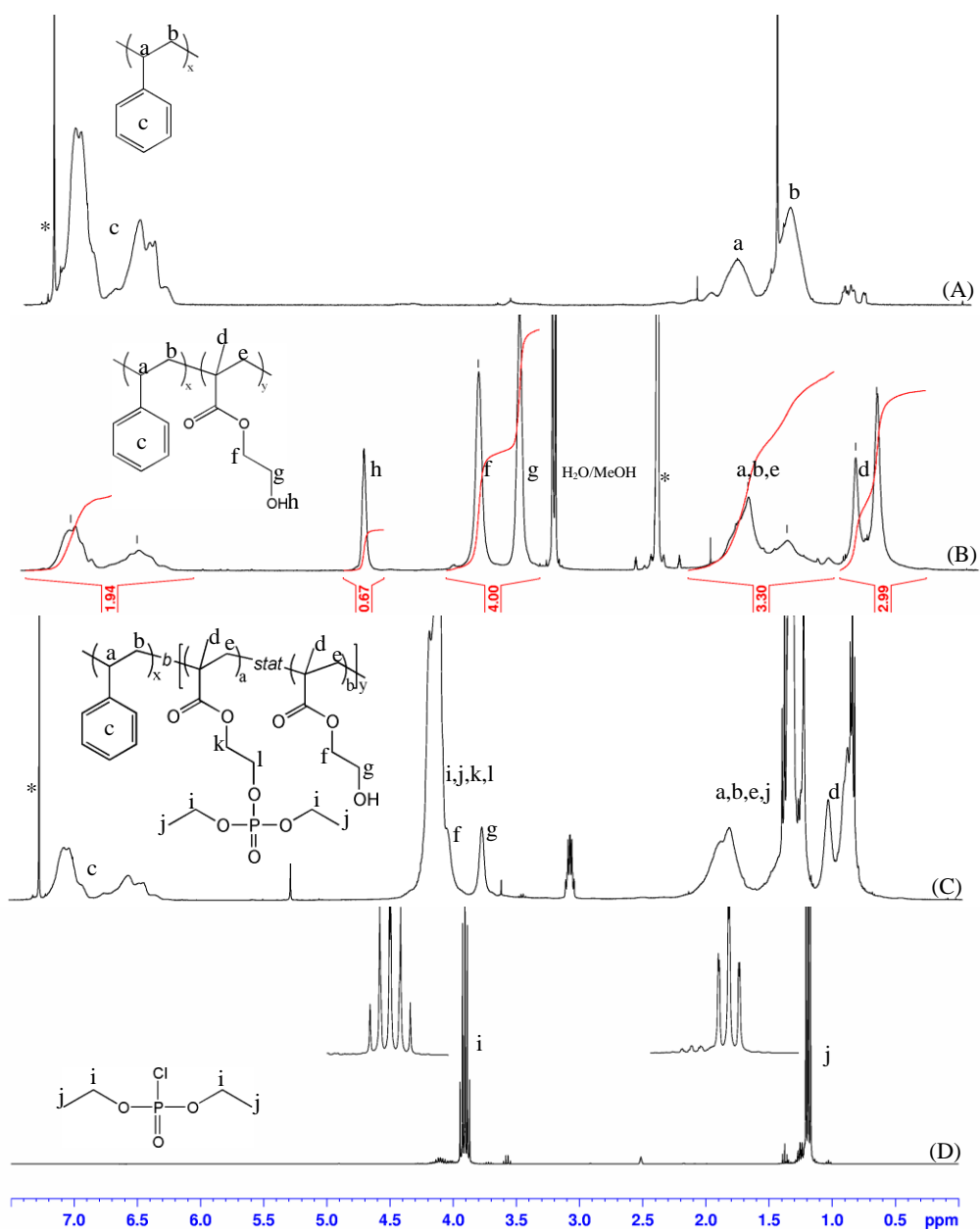
Figure 5.2. Assigned ^{1}H NMR spectra for PS in CDCl$_3$ (A), PS-*b*-PHEMA in DMSO-*d*$_6$ (B), PS-*b*-P(DEPEMA-*co*-HEMA) in DMSO-*d*$_6$ (C) and diethyl chlorophosphate in CDCl$_3$ (D).

In the next step, phosphorylation of PS-b-PHEMA was achieved using diethyl chlorophosphate in presence of Et$_3$N in THF (see Scheme 5.1). The onset of such reaction was evidenced by the formation of a solid precipitate (Et$_3$N$^+$Cl$^-$) soon after the dropwise addition of the organophosphate reagent. After purification and isolation of products, ^{1}H NMR (Figure 5.2(C)) and ^{31}P NMR (not shown) analysis clearly indicated the incorporation of the –P(O)(CH$_3$CH$_2$)$_2$ moiety (Figure 5.2(D)). Moreover, GPC traces recorded before and after the

phosphorylating reaction visibly demonstrated an increase in the molecular weight due the incorporation of $-P(O)(CH_3CH_2)_2$ in the polymer chain (Figure 5.3).
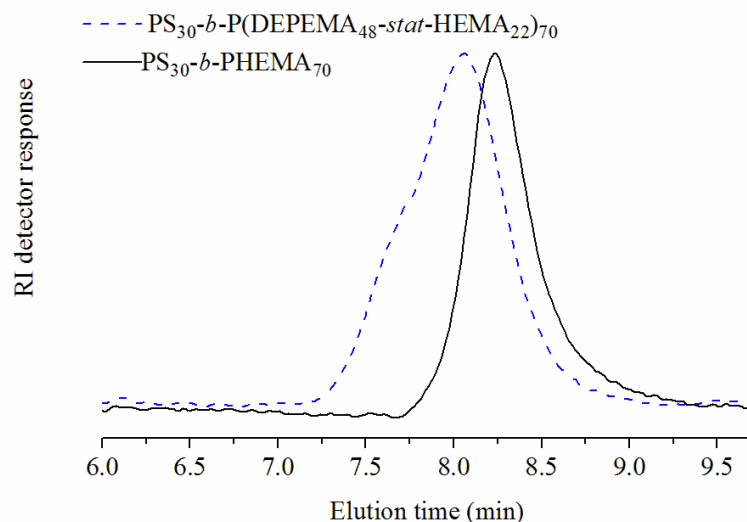
Figure 5.3. GPC traces of PS_{30}-*b*-$PHEMA_{70}$ and PS_{30}-*b*-$P(DEPEMA_{48}$-*co*-$HEMA_{22})_{70}$ copolymers.

The degree of substitution of $-OH$ groups by $-P(O)(CH_3CH_2)_2$ (DS_{phosph}) in the resulting PS-*b*-P(DEPEMA-*co*-HEMA) polymer (3) was estimated from ^1H NMR spectra on the basis of signals relative to protons *g* (2H) and *i,j,k,l* (8H) (see Figure 5.2(C)) applying the following relation

$$DS_{phosph} = \frac{\left(\dfrac{A(4.5-3.9\,ppm)-A(3.9-3.4\,ppm)}{8H}\right)}{\left(\dfrac{A(4.5-3.9\,ppm)-A(3.9-3.4\,ppm)}{8H} + \dfrac{A(3.9-3.4\,ppm)}{2H}\right)} x100 \qquad \text{(eq. 5.2)}$$

The DS_{phosph} was dictated by the number of added equivalents of the limiting reagent (diethyl chlorophosphate), as summarized in Table 5.3. Although quantitative conversions were not observed ($DS_{phoph} \leq 83\%$), different DS_{phoph} were achieved using the same precursor through this rather simple modification procedure, hence allowing the preparation of amphiphilic macromolecules with variable number of protein binding sites (phosphate groups). For example, entry 4 in Table 5.3 contains nearly 5 times more phosphorylated units (120 DEPEMA units) than entry 3 (25 DEPEMA units). The hydrolysis of $-P(O)(CH_3CH_2)_2$ groups into ionisable $-P(O)(OH)_2$ phosphonic diacid was carried out in a two-steps protocol using trimethylsilyl halides (either chloride or bromide), which are powerful silylating agents that allows smooth cleavage of phosphoric alkyl esters (see Scheme 5.1), as previously described by Zhu et al [133]. The

sylilation of –P(O)(OCH$_3$CH$_2$)$_2$ functional groups in this intermediate step was easily confirmed by 1H NMR, which showed the disappearance of –P(O)(OCH$_3$CH$_2$)$_2$ signal at ca. 4.3 – 4.0 ppm, whereas typical chemical shift of sylilated residues appeared at low field. Rapid hydrolysis to produce the phosphonic diacid form in presence of methanol, thus yielding the resulting PS-*b*-P(PEMA-co-HEMA) polymer (4) (Scheme 5.1).

Table 5.3. Characteristics of PS-*b*-P(PEMA-*co*-HEMA) copolymers prepared by phosphorylation of PS-*b*-PHEMA precursors.

Entry	PS$_x$-*b*-P(PEMA$_a$-*co*-HEMA$_b$)$_y$	Targeted	Achieved
	x-(a-b)y	DS_{phosp} (%)	DS_{phosp}[a] (%)
1	30-(15-55)70	50	**22**
2	30-(48-22)70	100	**69**
3	55-(25-120)145	50	**17**
4	55-(120-25)145	100	**83**

[a] Calculated by ^{1}H NMR in DMSO-d_6 on basis of signals relative to protons *g* (2H) and *i,j,k,l* (8H) (see Figure 5.2(C)) applying equation 5.2.

5.2. Self-assembly and Polyelectrolyte behavior of PS-*b*-P(PEMA-co-HEMA)

The PS-b-P(PEMA-co-HEMA) copolymers are amphiphilic macromolecules that exhibit self-organizing ability when adequately manipulated in presence of selective solvents. Micelles made from the samples listed in Table 5.3 can be prepared using the so-called indirect dissolution method. In such a case, the polymer is firstly dissolved in a water-miscible organic solvent such as acetone, and micellization is subsequently induced by slow addition of water (selective solvent for P(PEMA-co-HEMA) block) or, instead, an aqueous solutions such as Tris buffer at pH = 8.0. Therefore, in aqueous media these nano-objects are formed with a hydrophobic PS core and a hydrophilic P(PEMA-co-HEMA) corona bearing negatively charged

phosphate moieties (Scheme 5.2), which are potential binding sites for Annexin-A5. As mentioned above, the number of phosphate moieties depended on DS_{phop}.
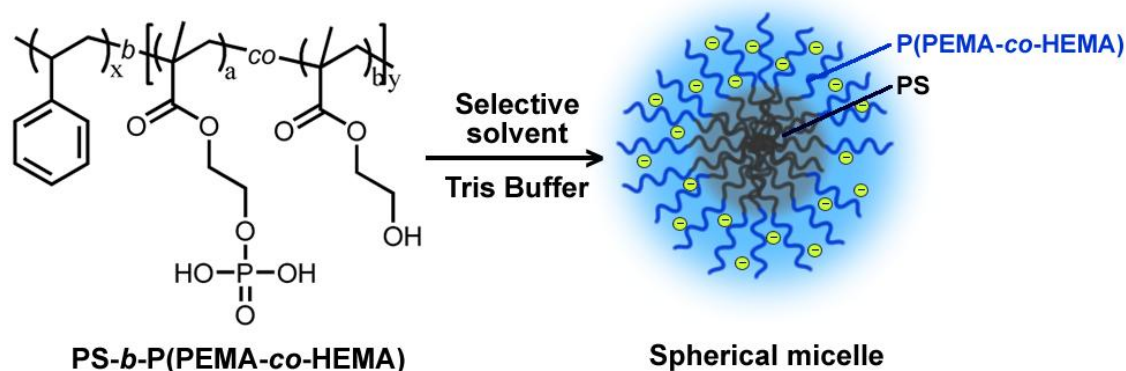
Scheme 5.2. Aqueous solution behavior of PS-*b*-P(PEMA-co-HEMA) copolymers.

Light Scattering

Figure 5.4 shows typical autocorrelation functions *C(q,t)* measured at different scattering angles and distributions of the relaxation times *A(t)* at 90° as revealed by CONTIN analysis for 1.0 mg/mL PS_{30}-*b*-$P(PEMA_{48}$-co-$HEMA_{22})_{70}$ (A) and PS_{55}-*b*-$P(PEMA_{120}$-co-$HEMA_{20})_{145}$ (B) solutions in Tris buffer at pH = 8.0. The insets in Figure 5.4 depict the typical q^2-dependence of the relaxation frequency (Γ) for diffusive scattering particles.[95] The nano-objects originated from PS-*b*-P(PEMA-co-HEMA) copolymers exhibited narrow distributions of relaxation times, with a fast mode corresponding to the diffusive motion of individual micelles. The slow mode (small amplitude) was most likely associated with the existence of a minor amount of dynamical aggregates in solution.

The hydrodynamic diameter ($2R_H$) of PS-*b*-P(PEMA-co-HEMA) micelles depended on the molecular dimensions of unimers (individual chains), in good agreement with data reported elsewhere.[99, 134] The DLS results resumed in Table 5.4 show that upon increasing the degree of polymerization (DP_n) of the core- and corona-forming blocks from, respectively, 33

and 70 up to 55 and 145, the size increased from $2R_H \cong 14 - 18$ nm to $2R_H \cong 20 - 50$ nm, thus implying a huge augmentation in the micellar volume (roughly from 11×10^3 nm^3 to 52×10^4 nm^3). From a drug delivery point of view, these differences may have significant implications on the loading efficiency, drug release profile, partition coefficient and bioavailability and biodistribution of the carrier system.[45, 134, 135] The variation of the degree of phosphorylation (DS_{phosp}), which strongly dictates the solubility properties of the hydrophilic block, seemed to affect the micellar size in a more complex behavior as deduced from Table 5.4. For shorter copolymer chains (Table 5.4, entries 1 and 2), a slight increase in $2R_H$-values took place upon increasing DS_{phosp}. Meanwhile, the opposite trend was observed for longer copolymer chains due to reasons discussed below.

Similarly to PBuA-*b*-PECVPD system, micelles formed by PS-*b*-P(PEMA-co-HEMA) also have negatively charged groups at the corona and, therefore, ionic strength effects in the light scattering behavior are anticipated. These effects were studied following essentially the same procedure as described in the previous chapter.

In this part of the study, micelles were prepared as described above, and then the solution was dialyzed against milli-Q water in order to remove any salt present in the system. Figure 5.5 shows the variation of $KC_p/I(q)$ as a function of q^2 for 1.0 mg/mL PS$_{55}$-*b*-P(PEMA$_{120}$-co-HEMA$_{25}$)$_{145}$ micellar solutions containing different amounts of added NaCl salt ($C_s = 0 - 100$ mmol/L), as indicated. This sample was chosen for polyelectrolyte studies because it presents the highest amount of phosphated groups, being presumably more sensitive to charged species in solution (salts). As for the PBuA-*b*-PECVPD case, a negative slope was observed in absence of salt, indicating strong interparticle correlations. As C_s increased up to $C_s \leq 0.2$ mmol/L, the slope decreased progressively, then became positive for $C_s > 0.5$ mmol/L, and finally remained increasing slightly as C_s continued to increase. A virtually constant slope was evidenced for $C_s > 10$ mmol/L. At this point, the electrostatic interactions (repulsions) within the micelle corona are presumably shielded by added salt ions,[59, 77] so that further addition of salt practically did not affect the micelle structure. Therefore, when prepared in buffer (20 mM Tris-HCl, pH 8.0, 0.02% NaN$_3$, ~200 mM NaCl; this buffer is typically used in the preparation and manipulation of Annexin-A5), the salt concentration already present in the system is more than enough to shield all the electrostatic interactions at the micelle corona. Such polyelectrolyte behavior was also confirmed by an abrupt increase in the total scattered light intensity (I_{sc}) as a

function of C_s (Figure 5.6), hence reflecting the higher mobility of scattering objects upon screening of electrostatic repulsions by counter-ions.[59, 65, 76, 77]

Figure 5.7 describes the variation of the intercept $KC_p/I(q=0)$ as a function of C_s (i.e., the values of $KC_p/I(q)$ at $q = 0$ found from linear extrapolation of data in Figure 5.6). As discussed for the PBuA$_{35}$-b-PECVPD$_{30}$ micelles, the decrease in $KC_p/I(q=0)$ observed in Figure 5.7 essentially reflects the decrease in the second virial coefficient (A_2), and in the radius of gyration (R_g).[77, 121] However in this case, at high salt concentrations, A_2 is reduced by approximately 1/3 its initial value.

Table 5.4. Molecular and self-assembly characteristics of PS-b-P(PEMA-co-HEMA) copolymers prepared by phosphorylation of PS-b-PHEMA precursors.

Entry	PS$_x$-b-P(PEMA$_a$-co-HEMA$_b$)$_y$ x-(a-b)y	Number of Phosphate groups	Mw Polymer (g/mol)	ϕ^a Hydrophobic	Mw Micelles^b (g/mol)	N_{agg}^c	$2R_H$
1	30-(15-55)70	15	13424	0.23	3.4x10^6	253.2	14
2	30-(48-22)70	48	16064	0.19	2.3x10^6	143.1	18
3	55-(25-120)145	25	26578	0.21	2.2x10^7	827.7	50
4	55-(120-25)145	120	34178	0.16	1.73x10^6	50.61	20

[a] Volume fraction of the PS hydrophobic segment considering the polymer density equal to 1.0 g/mL.

[b] Micellar molecular weight estimated by SLS using dn/dC = 0.13 mL/g.

[c] Aggregation number calculated from the relation $N_{agg} = M_{w,mic}/M_{w,unimers}$.
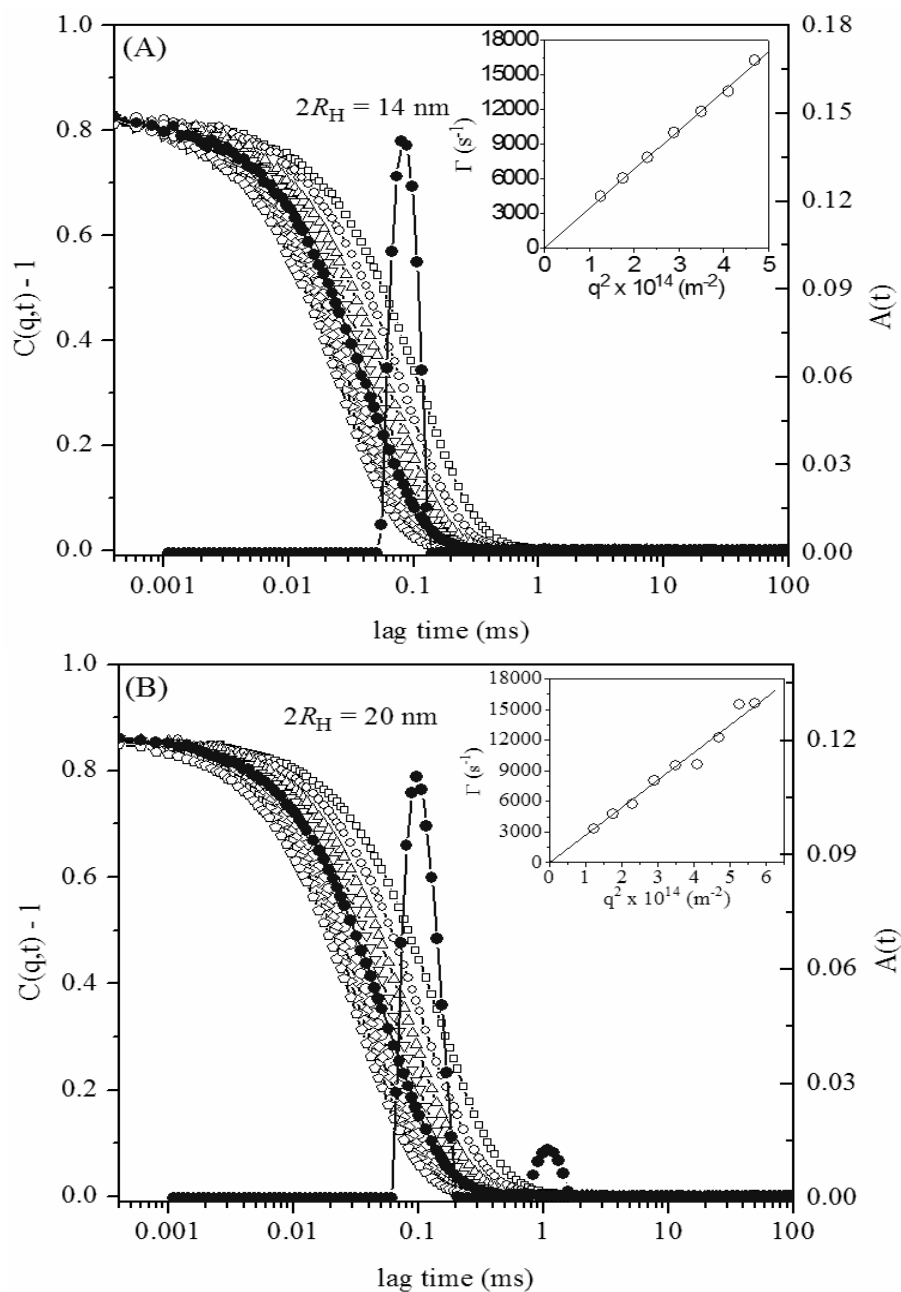
Figure 5.4. Autocorrelation functions *C(q,t)* and distributions of the relaxation times *A(t)* at scattering angle of 90° for 1.0 mg/mL PS_{30}-*b*-$P(PEMA_{48}$-co-$HEMA_{22})_{70}$ (A) and PS_{55}-*b*-$P(PEMA_{120}$-co-$HEMA_{20})_{145}$ (B) micellar solutions in Tris buffer at pH = 8.0.
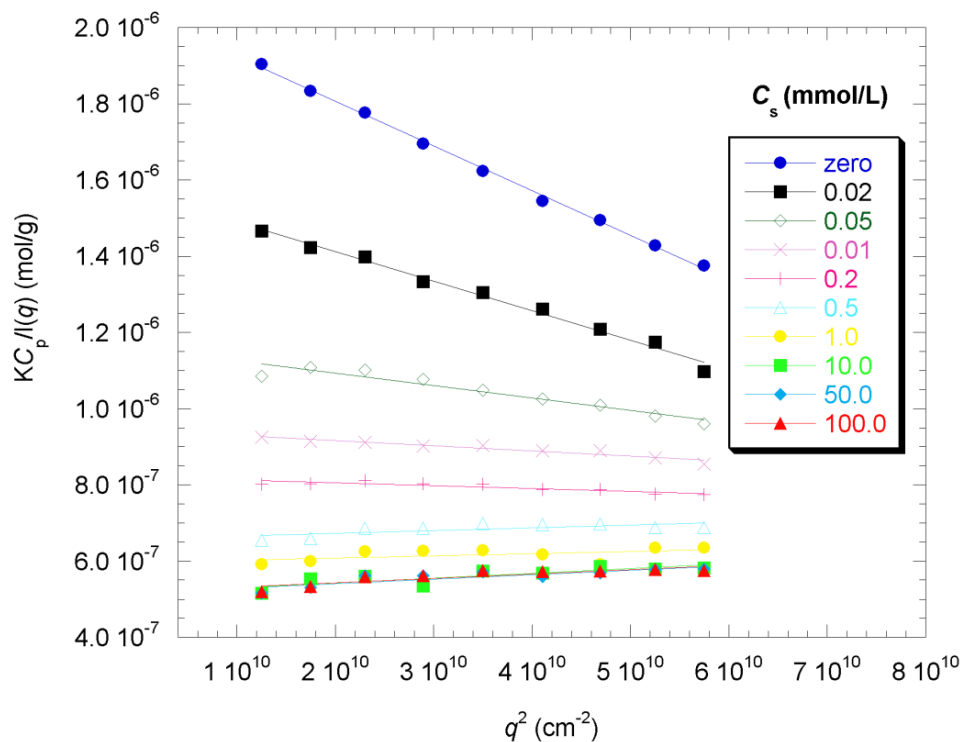
Figure 5.6. $KC_p/I(C_p,q)$ vs q^2 curves for 1.0 mg/mL PS$_{55}$-*b*-P(PEMA$_{120}$-co-HEMA$_{25}$)$_{145}$ micellar solutions containing different amounts of added NaCl salt.
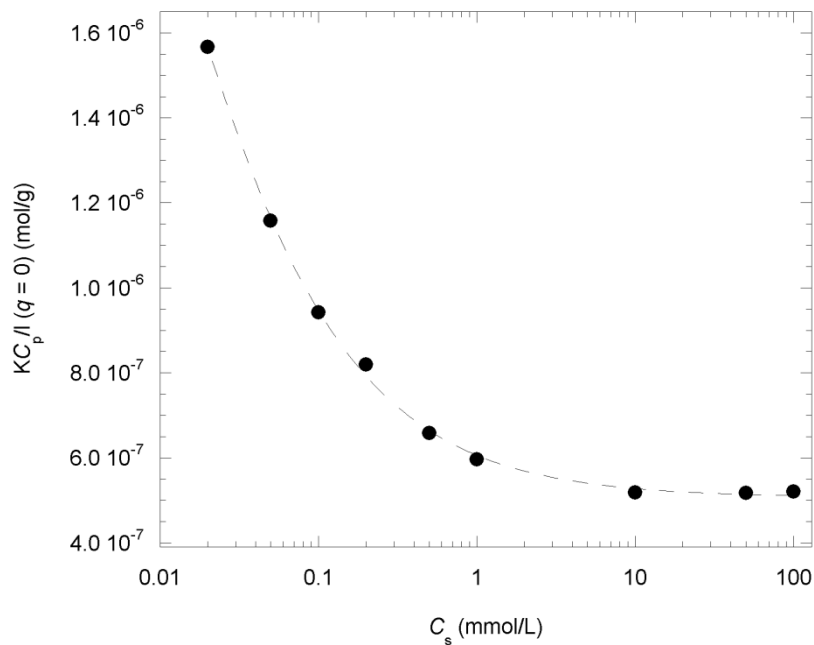
Figure 5.7. Variation in the total scattered light intensity at 50° scattering angle as a function of C_s.
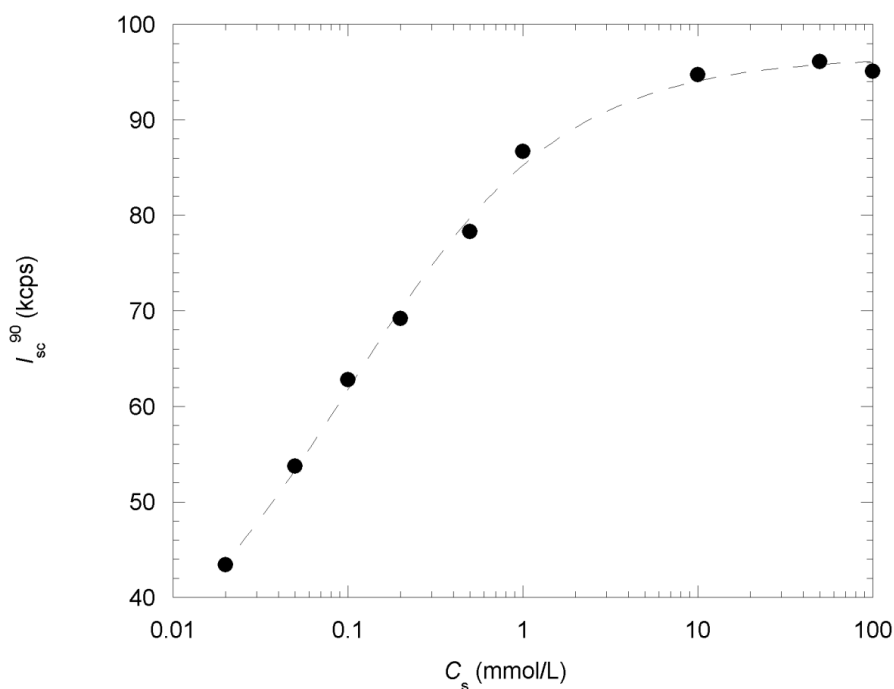
Figure 5.8. $KC_p/I(C_p,q=0)$ as a function of C_s for 0.5 mg/mL PBuA$_{35}$-b-PECVPD$_{30}$ micellar solutions.

The DLS results obtained for this system are illustrated in Figure 5.9, in which the variation of apparent hydrodynamic radius (R_H^{app}) as a function of the salt concentration (C_s) for 1.0 mg/mL micellar solutions is given. A very interesting behavior was observed in the present case; the $2R_H$-values increased from 9 nm up to 16 nm with Cs in the range zero(no added salt) < C_s < 1.0 mmol/L. Such an observation has been reported in a previous work by Matejicek et al.[136] According to these authors, this is an unusual behavior which is normally very difficult to detect in micellar polyelectrolyte systems. The addition of small amount of salt to very diluted copolymer solutions promotes further dissociation of phosphate groups due to well-known effects of background electrolytes on the acid dissociation constants (Ka increases with C_s).[137] An insufficient screening of the electrostatic repulsion between newly ionized groups causes expansion of micellar shells due to electrostatic repulsions. The transition from osmotic brush regime to salted brush regime was however not observed in salt concentration range investigated in this work.
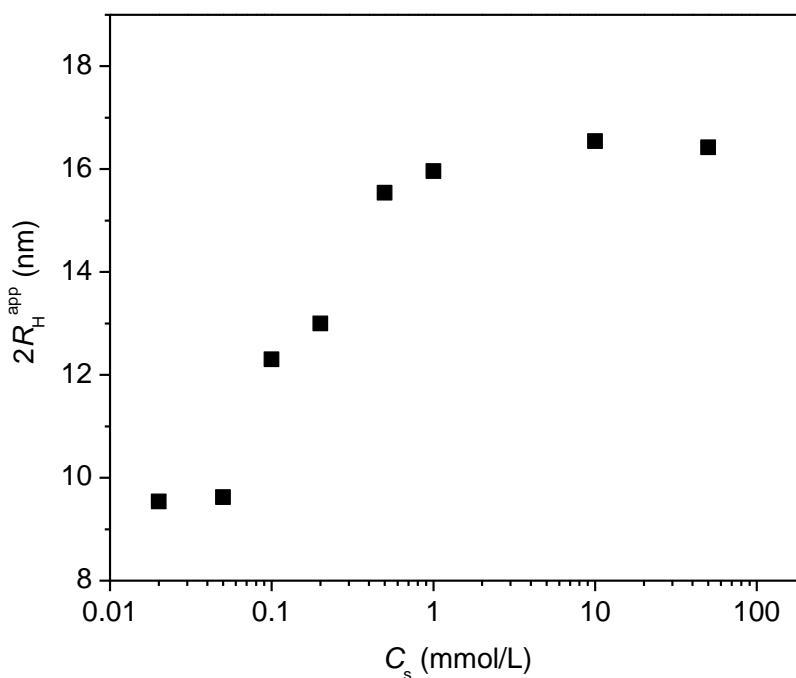
Figure 5.9. Variation in the hydrodynamic diameter ($2R_H$) as a function of salt concentration (C_s).

TEM

The spherical micellar morphology and the low polydispersity of the particles was corroborated by TEM experiments, as illustrated in Figure 5.10, which shows a typical TEM micrograph of negatively stained PS_{30}-*b*-$P(PEMA_{48}$-co-$HEMA_{22})_{70}$ micelles. The size determined from TEM imaging ($2R$ = 10 nm) is slightly smaller than that determined by DLS measurements ($2R_H$ = 14 nm), due to reasons already discussed above.
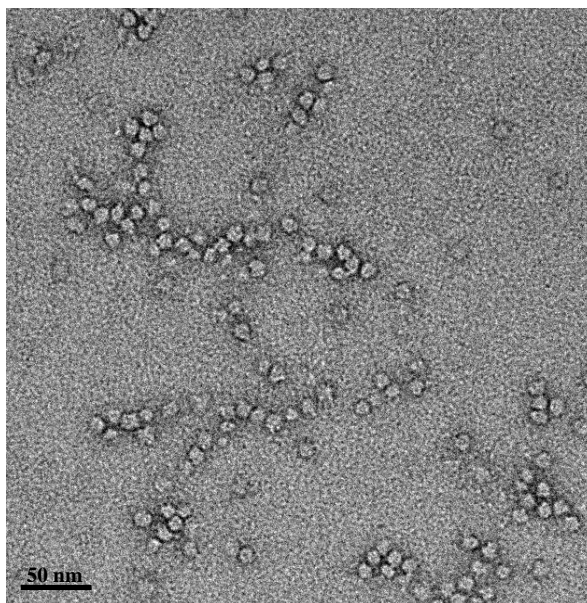
Figure 5.10. TEM image of negatively stained PS_{30}-b-P($PEMA_{48}$-co-$HEMA_{22}$)$_{70}$ self-assemblies. Scale bar: 50 nm.

5.3. Annexin-A5 binding onto PS-b-P(PEMA-co-HEMA) micelles

The protein binding ability of PS-b-P(PEMA-co-HEMA) micelles was investiaged by light scattering, QCM-D, and PAGE measurements. Similarly to small unilamellar vesicles (SUV) formed by phospholipids (*Chapter 3*), and micellar nanoparticles with ((1-ethoxycarbonyl)vinylphosphonic diacid) (PECVPD) corona-forming blocks (*Chapter 4*), binding of Annexin-A5 proteins to the hydrophilic P(PEMA-co-HEMA) shell of PS-b-P(PEMA-co-HEMA) micelles can be achieved by adding 2.0 mmol/L $CaCl_2$ to solutions containing micelles and free Annexin-A5 (Scheme 5.3). Such a binding phenomenon provokes a marked increase in the average diameter of the nanoparticles. For example, the characteristic $2R_H$ = 14 nm of PS_{30}-b-P($PEMA_{48}$-co-$HEMA_{22}$)$_{70}$ micelles increase up to $2R_H$ = 30 nm (see Figure 5.11(A)) upon protein decoration. Such a large augmentation suggests the migration of Annexin-A5 into the micelle corona, in a process favored by the existence of phosphate groups along the micelle corona. In parallel to the size increase, a huge increase in the total light scattered intensity also occurred, as illustrated in Figure 5.11(B), due to the increase in the mass and/or density of the scattering

particles. The Annexin-A5 binding process to micelles (and other phosphorylated molecules) is reversible upon the addition of specific Ca^{2+}-chelating agents. One notes, however, that the effect of adding Ca^{2+} to bind the Annexin-A5 protein on the micelle surface favors at the same time the formation of large aggregates (slow mode, see inset in Figure 5.11(A)).
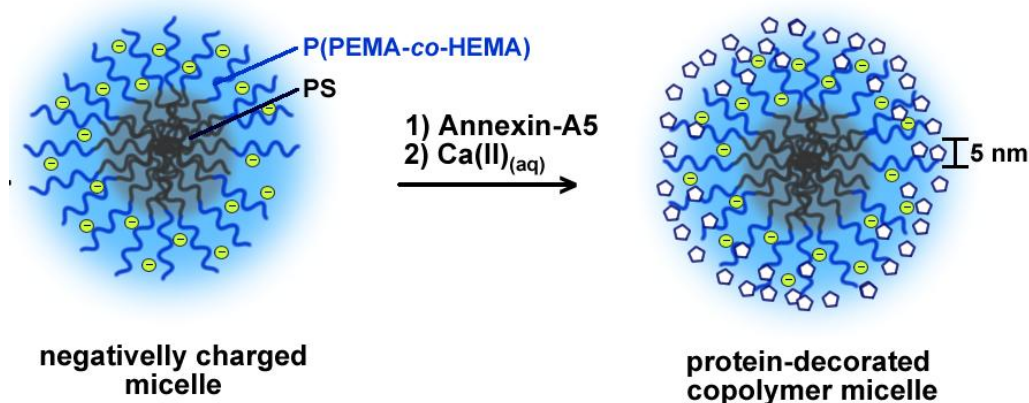
Scheme 5.3. Annexin-A5 protein decoration of micelles originated from their self-assembly.

The ability of Annexin-A5 proteins to bind to block copolymer micelles having phosphonic diacid groups at their hydrophilic coronas has been corroborated, therefore, using different systems: PS-b-P(PEMA-co-HEMA) and PBuA-b-PECVPD. These are important observations indeed, as long as Annexin-A5 protein presents potential applications non-invasive in vivo imaging of pathologic areas and targeted micelle-mediated drug delivery. Moreover, the fact that amphiphilic block copolymer generally exhibit nano-phase separation in bulk, copolymer with such characteristics may find interesting applications also in the controlled fabrication of biochips, provided that Annexin-A5 proteins could be precisely positioned at the phosphate-enriched phase.
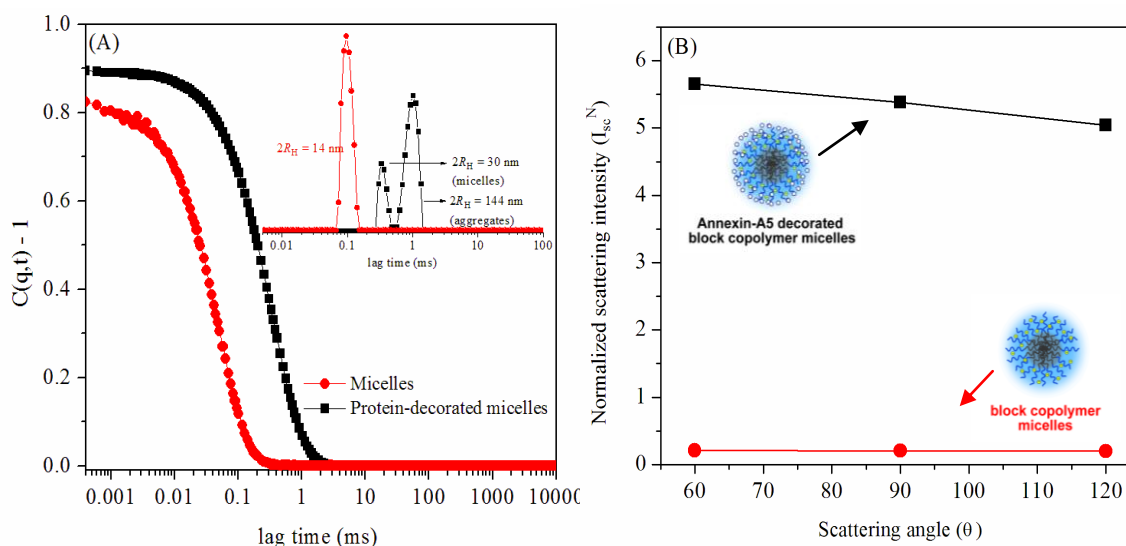
Figure 5.11. Dependence of autocorrelation functions C(q,t) and distributions of the relaxation times A(t) at scattering angle of 90° on the Annexin-A5 binding to PS_{30}-b-$P(PEMA_{48}$-co-$HEMA_{22})_{70}$ micelles in presence of $CaCl_2$ **(A)**, and variation in the normalized light scattering intensity upon Annexin-A5 binding onto micelles at three different scattering angles **(B)**.

Complementarily to light scattering techniques, QCM-D, a surface sensitive technique, has also confirmed the ability of the designed and synthesized block copolymer systems to bind the Annexin-A5 protein. Figure 5.12 exemplifies the response recorded when micelles formed by PS-b-P(PEMA-co-HEMA) were placed in contact with a monolayer of Annexin-A5 dimer in presence of calcium cations. It is important to note that before the addition of block copolymer micelles two other preliminary steps are necessary in order to build up the assemblies: the first step (pink arrow) corresponds to the addition of a SUV solution which forms a lipid bilayer, and the second one (arrow in green) consists in the deposition of a monolayer of chemically engineered "double" Annexin-A5 molecules (i.e.: one molecule is bound to the lipid bilayer while the other remains exposed to the surface; see also cartoons in Figure 4.23 for steps A and B). After the addition of block copolymers micelles (blue arrows), changes in frequency and dissipation were observed as a consequence of micelles binding to the protein layer. Rinsing with a buffer solution containing calcium ions did not change the properties of the system, indicating the formation of stable and specific interactions. Meanwhile, the addition of an EGTA solution (chelating agent) released the calcium-dependent surface-bound nano-objects (polymeric nanostructures and the protein layer), as judged by the residual frequency value

which corresponded to the initial value measured for the formation of a lipid bilayer. The addition of such a chelating agent confirms, therefore, the reversibility of the process.

As summarized in Table 5.5, changes in frequency and dissipation depended on the micellar characteristics. The frequency shift, which is related to the adsorbed mass, seemed to depend on N_{agg}, while changes in dissipation were apparently related with the micellar size. As expected, micelles having a high N_{agg} (higher molar mass) provoked important changes in frequency (up to $\Delta F \sim 84$ Hz for $N_{agg} = 828$; Table 5.5, entry 3), while micelles having smaller N_{agg} ($N_{agg} \sim 50$) promoted only a slight change in the frequency ($\Delta F \sim 10$ Hz). It is important to notice that the ΔF values determined were not used to calculate the mass of polymer bound as they will probably overestimate these values due to the presence coupled water. As for the dissipation parameter, an increase in the nanostructure size (higher R_H-values) led to the formation of less compact micelle-based layers (higher dissipation).
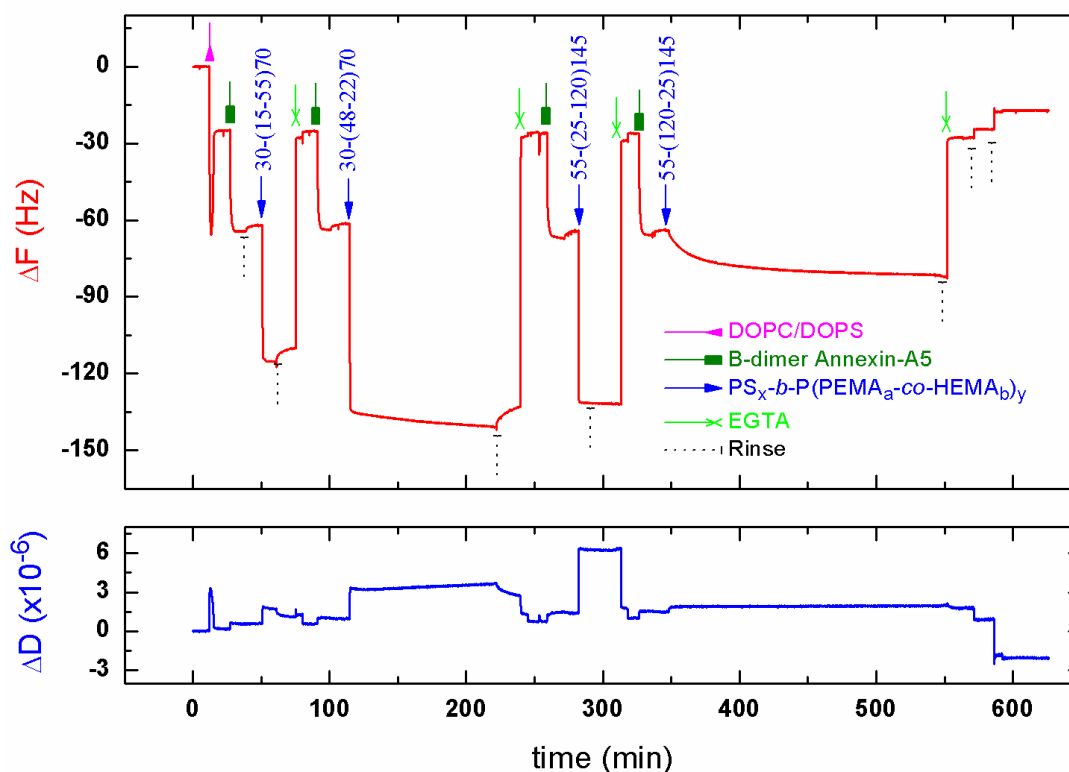
Figure 5.12. QCM-D data showing the formation of Annexin-A5/PS-*b*-P(PEMA-co-HEMA) assemblies on to lipid bilayers, as indicated. All added polymer solutions contained the same amount of polymer (Cp = 1.0 mg/mL).

Table 5.5. QCM-D data (frequency ΔF and dissipation ΔD) related to the formation of Annexin-A5/PS-*b*-P(PEMA-co-HEMA) assemblies and, some characteristics of the polymeric structures.

Entry	PS$_x$-*b*-P(PEMA$_a$-*co*-HEMA$_b$)$_y$ x-(a-b)y	ΔF (Hz)	ΔD (x 1.10^{-6})	Mw Micelles[b] (g/mol)	N_{agg}[c]	$2R_H$	Phosphate density in surface (x 10^4 mol/cm^2)
1	30-(15-55)70	55	2.2	3.4x10^6	253	14	18.1
2	30-(48-22)70	76	2.0	2.3x10^6	143	18	29.4
3	55-(25-120)145	84	7.1	2.2x10^7	828	50	1.2
4	55-(120-25)145	10	3.8	1.7x10^6	51	20	27.9

In order to determine the amount of polymeric micelles needed to saturate the protein layer (i.e.: to obtain a fully covered surface), the influence of the polymer concentrations (for a constant volume of added solution) on the QCM-D data was determined for a selected system (PS$_{30}$-*b*-P(PEMA$_{48}$-co-HEMA$_{22}$)$_{70}$ – entry 1 in Table 5.5). Figure 5.13 shows the variation of ΔF as a function of C_p, where a steeply increase in ΔF was observed as C_p increased up to 20 μg/mL. For more concentrated solutions ($C_p \geq 20$ μg/mL), a plateau was detected in which ΔF remained approximately constant at 55Hz as C_p increased. These results suggested, therefore, that the concentration normally used in QCM-D experiments ($C_p = 1000$ μg/mL = 1.0 mg/mL) is well above the amount required to saturate the protein layer.

The deposition of block copolymer micelles produces a micelle-covered surface, onto which further hierarchical assembly can be induced by addition of Annexin-A5. The results corresponding to such experiments are shown in Figure 5.14. After the addition of Annexin-A5 protein (pink arrow at ~ 200 min) there occurred an increase in ΔF due to protein binding. After rinsing with buffer solution, though, a slight decrease in ΔF took place due to the release of non-specifically bounded proteins. The amount of protein bound to the surface in this second protein deposition step depended on the density of phosphate groups at the micellar corona (see discussion below).
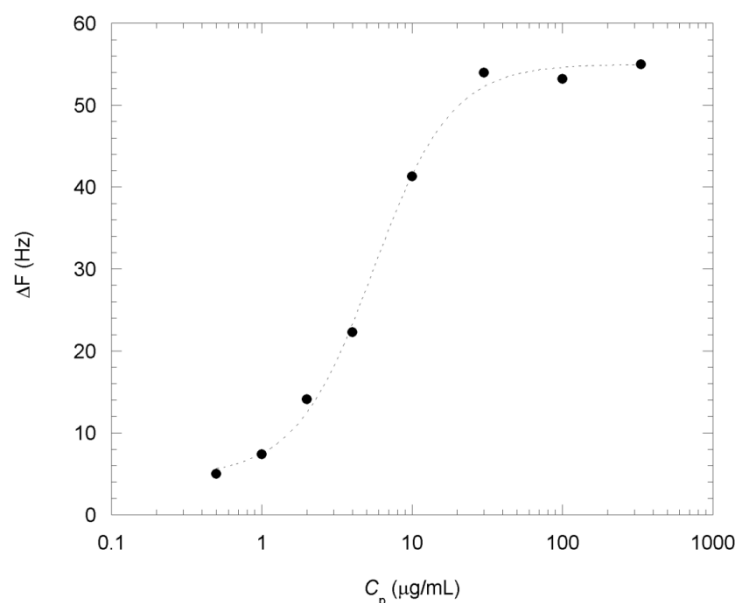
Figure 5.13. Variation of the frequency (ΔF) measured by QCM-D as a function of the polymer concentration (C_p) added on to lipid bilayer for the PS$_{30}$-*b*-P(PEMA$_{15}$-co-HEMA$_{55}$)$_{70}$ system.

It was possible to establish a relation between the amount (ΔF) of micelles and protein bound (Figure 5.15). As the ΔF due to the polymer deposition increase, the amount (ΔF) of protein binding on to such block-copolymer micelles also increases until a saturation point is reached. For the studied system, PS$_{30}$-*b*-P(PEMA$_{15}$-co-HEMA$_{55}$)$_{70}$, the maximum amount of protein bound to the micelles was equivalent to ΔF = 5 Hz for the deposited 55Hz of micelles.
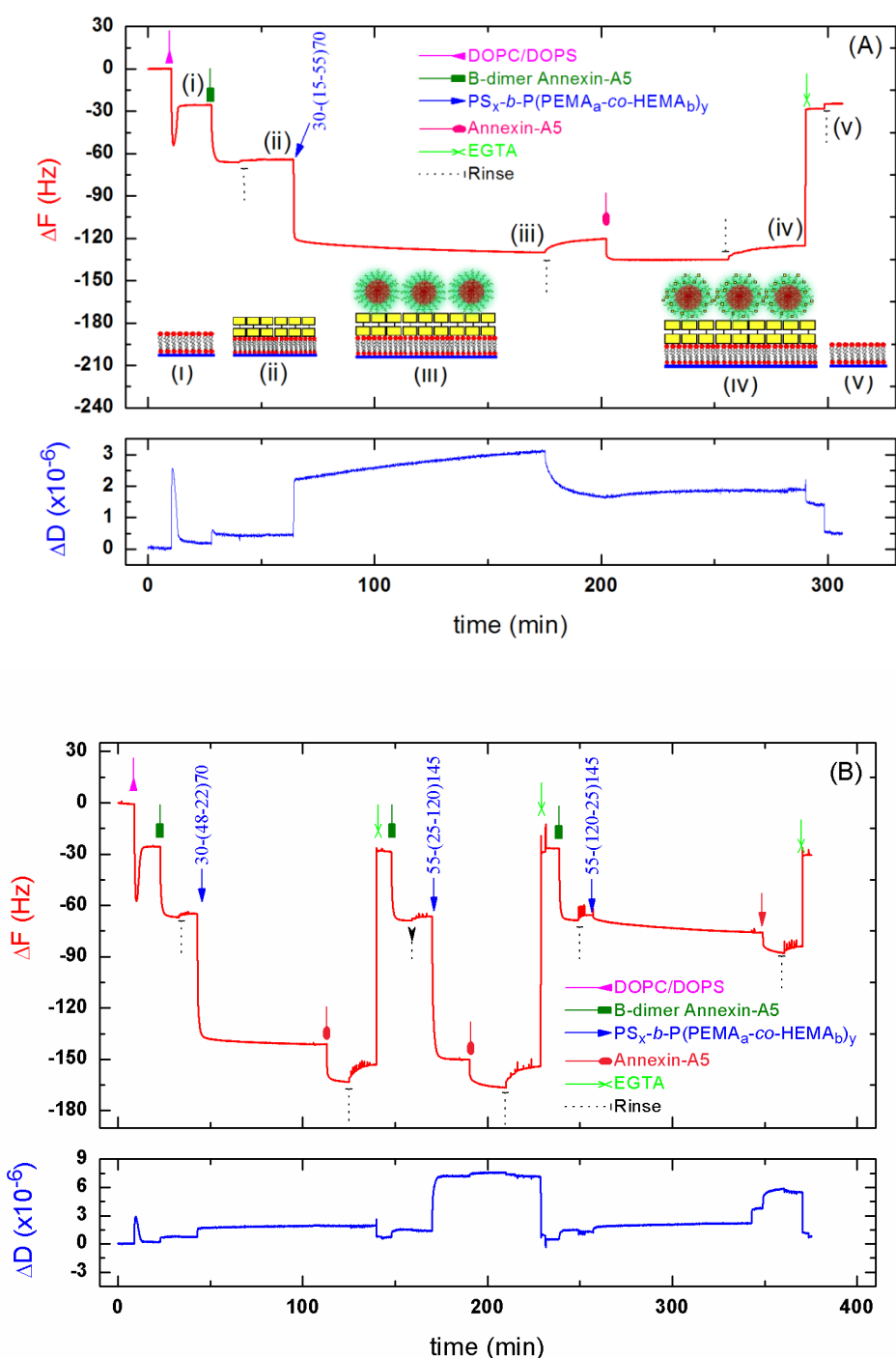
Figure 5.14. QCM-D data showing the formation of supra-molecular Annexin-A5/PS-*b*-P(PEMA-co-HEMA)/Annexin-A5 assemblies onto lipid bilayers for PS$_{30}$-*b*-P(PEMA$_{15}$-co-HEMA$_{55}$)$_{70}$ (A) and, PS$_{30}$-*b*-P(PEMA$_{48}$-co-HEMA$_{22}$)$_{70}$, PS$_{55}$-*b*-P(PEMA$_{25}$-co-HEMA$_{120}$)$_{145}$ and PS$_{55}$-*b*-P(PEMA$_{120}$-co-HEMA$_{25}$)$_{70}$ as indicated (B). C_p = 1.0 mg/mL in all experiments.
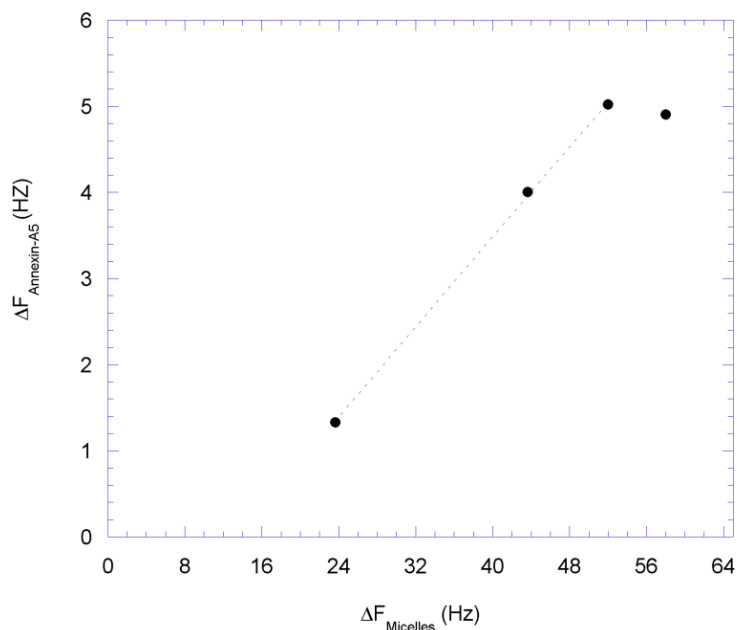
Figure 5.15. Variation of the frequency (ΔF) due to Annexin-A5 bind on to block-copolymer micelles as a function of the ΔF corresponding to the added block-copolymer micelles.

In parallel with QCM-D, non denaturating PAGE experiments were carried out in order to quantify the amount of Annexin-A5 bound with PS-*b*-P(PEMA-co-HEMA) micelles. The obtained results are illustrated in Figure 5.16 for PS$_{30}$-*b*-P(PEMA$_{15}$-co-HEMA$_{55}$)$_{70}$. Experiments were done for all synthesized block copolymer (entries 1-4 in Table 5.5) in presence and in absence of calcium cations, using different amounts of block copolymer micelles and a constant amount of Annexin-A5. In addition to protein-polymer assemblies, solutions containing either, protein or micelles, were analyzed as a control of the objects displacement. As judge by the results, block copolymer micelles and polymer-protein assemblies were stopped at the top of the gel, while the Annexin-A5 moves toward the bottom of the gel. As expected, the binding of Annexin-A5 on to polymer micelles did not occur in absence of Ca^{2+} no matter how much polymer micelles were used (Figure 5.16(B)). However, in presence of calcium (Figure 5.16(A)) an increase in the amount of polymer decreased the amount of protein able to move toward the bottom. For 3 μg of polymer no more protein is able to moves due to polymer binding.
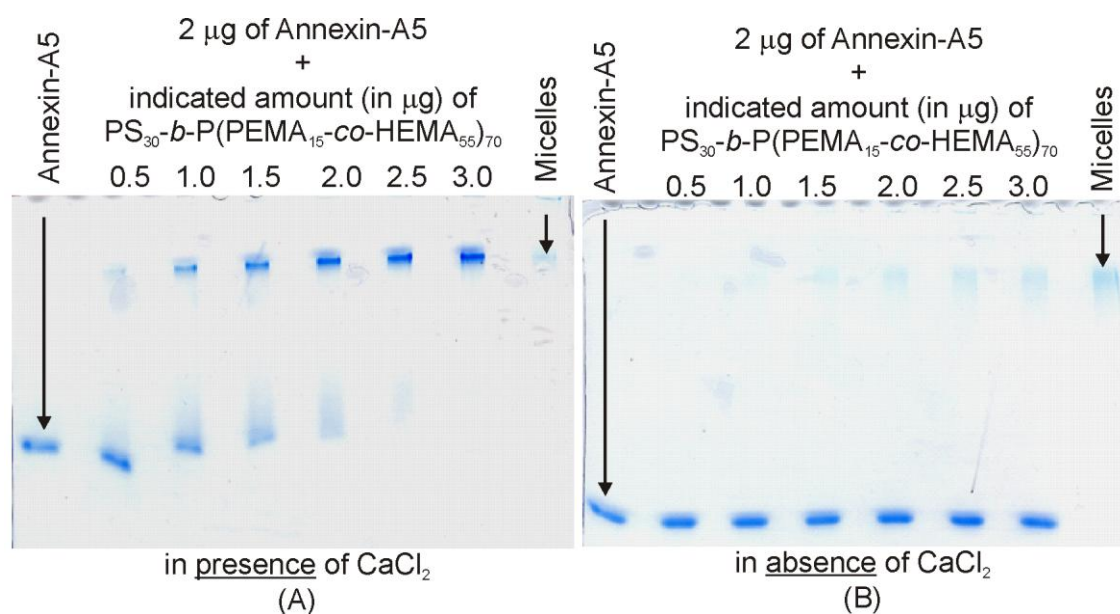
Figure 5.16. PAGE results obtained for the Annexin-A5 protein, the PS_{30}-*b*-P(PEMA$_{15}$-co-HEMA$_{55}$)$_{70}$ micelles and a mixture of both in presence (A), and in absence (B) of Ca^{2+}. For mixtures different amounts of block copolymer micelles were used in presence of the same amount of protein, as indicated.

Figure 5.17 summarizes the results obtained by QCM-D for the deposition of Annexin-A5 onto a micelle-covered surface and PAGE for all block copolymer systems. The results are plotted against the phosphate groups density at the micellar surface, which was calculated using the light scattering data (R_H, $M_{w,micelles}$). Judging by the results obtained using both techniques, the amount of protein bound onto such polymer micelles increases as the phosphate density increase. The more phosphate groups are present at the surface, the more sites are able to bind the protein. For PS_{55}-*b*-P(PEMA$_{25}$-co-HEMA$_{120}$)$_{145}$ no binding could be evidenced by PAGE probably due to the low density of phosphate groups or even due to solubility problems in the medium, as judged by the low volume fraction of the hydrophilic PEMA segment.
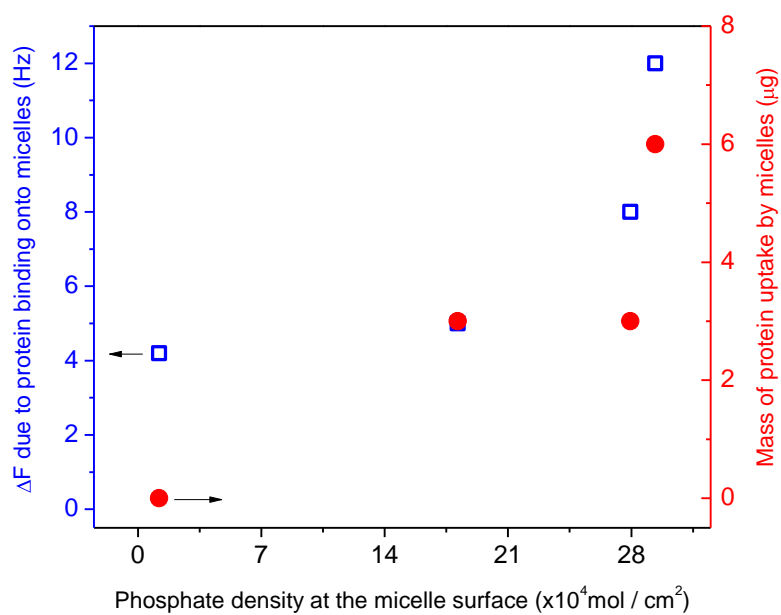
Figure 5.17. Frequency shift, ΔF (open squares), measured by QCM-D and mass determined by PAGE (circles) obtained for the Annexin-A5 binding onto PS_x-*b*-P(PEMA$_a$-co-HEMA$_b$)$_y$ micelles as a function of the phosphate density at the micelle corona.

Conclusions and Outlook (English)

Well-defined PS-*b*-P(PEMA-*stat*-HEMA) and PBuA-*b*-PECVPD copolymers could be synthesized by ATRP. Such phosphorylated macromolecules self-assemble in water to originate narrowly distributed spherical micelles with hydrophobic core and hydrophilic corona bearing negatively charged phosphate moieties (binding sites for Annexin-A5 proteins).

The polyelectrolyte behavior of block copolymer micelles was evidenced mainly by scattering techniques (DLS, SLS and X-ray). Interesting pH-, salt- and concentration-dependent polyelectrolyte features of this system in aqueous media is conferred by the hydrophilic phosphate corona bearing negatively charged phosphonic diacid groups [$-P(O)(OH)_2$] with two distinct acid dissociation constants. The results clearly revealed that neither salt addition (Cs = $0 - 100$ mM) nor polymer concentration (C_p = $0.5 - 20$ mg/mL) affect the micelle core size. The analysis of the SAXS data shed a light on the micellar interactions and morphology in absence and presence of added salt to the solution. A shrinking of the corona was observed upon addition of salt for PBuA-*b*-PECVPD, while un increase in the R_H was observed for PS-*b*-P(PEMA-co-HEMA). The size of the core was invariant over the whole range of concentrations and salt content investigated. Moreover, the micelle corona thickness was significantly influenced by ionic strength and pH, with light scattering measurements demonstrating the existence of different regimes in the I_{sc} vs pH plots. Such a behavior was due to the increase in the negative charge density at the micellar corona as a consequence of deprotonation process of phosphonic diacid groups. Cryo-TEM images confirmed the spherical size of the aggregates.

The protein binding ability of both block copolymers systems was demonstrated in presence of Ca^{2+} ions by LS measurements, QCM-D and PAGE. LS experiments revealed a remarkable increase in the average diameter of the nanoparticles due to their protein decoration. Concomitantly, a huge increase in the total light scattered intensity also occurred in response to the increase in the mass and/or density of the scattering particles. The binding process is reversible upon the addition of specific Ca^{2+}-chelating agents. For PS-*b*-P(PEMA-*stat*-HEMA), the QCM-D and PAGE results revealed a dependency of protein binding on the phosphate group density at the corona. As the density of phosphate groups able to bind such protein increase, the amount of bound protein also increase.

Finally, the herein discussed approach can be considered as an easy access to the preparation of Annexin-A5 protein binding micelles, meanwhile offering precise control over micellar dimensions and properties such as the phosphate moieties at the micelle periphery.

As of this moment, the perspectives for future studies are associated mainly with the studies of block copolymers with the ability to form vesicular structures in solution to better correlate with SUVs formed by phospholipids. We are also looking forward to evaluating the response of block copolymer able to bind chemically to the Annexin-A5 protein.

The microphase separation in bulk of the aforementioned systems still remains unexplored. Preliminary experiments carried out using small angle x-rays scattering (SAXS, ESRF) have confirmed the formation of nano-organized structures and the protein binding ability.

Conclusions et Perpectives (Français)

Dans ce travail de thèse, différents systèmes amphiphiles à base des copolymères à blocs (PS-*b*-P(PEMA-*stat*-HEMA) et PBuA-*b*-PECVPD) ont été synthétisés par ATRP. En présence de solvants sélectifs, ces copolymères à blocs portant des groupements phosphates en bout des chaines, ont donné lieu à des micelles sphériques bien définies comprenant un noyau hydrophobe et une couronne hydrophile. Celle-ci contenait des fonctions phosphate, lesquels sont responsables des interactions avec l'Annexine-A5.

Le comportement polyéletrolyte des nanoparticules de PS-*b*-P(PEMA-*stat*-HEMA) et PBuA-*b*-PECVPD a été confirmé par les techniques de diffusion de rayonnement (DLS, SLS et rayon-X). La présence des groupements [–P(O)(OH)$_2$] présentant deux constantes de dissociation induisent des propriétés sensibles au pH, à la concentration de tels polymères et à la concentration de NaCl dans le milieu. Les résultats obtenus ont montré que la taille des noyaux des micelles n'est pas affectée par la concentration de sel (Cs = 0 – 100 mM) et de copolymère (C_p = 0.5 – 20 mg/mL), contrairement à la couronne micellaire. Une forte diminution dans la taille de la couronne des micelles formées de PBuA-*b*-PECVPD a, en effet, été observée après addition de NaCl. Pour les micelles à base de PS-*b*-P(PEMA-co-HEMA), une augmentation de leur rayon hydrodynamique a été observe après addition de sel. Selon les résultats obtenus par diffusion de la lumière, les courbes I_{sc} vs pH présentent deux domaines distincts. Ce comportement est attribué à l'augmentation du nombre des charges négatives dans la couronne micellaire en fonction de la dissociation des groupements diacides phosphoniques. Les images obtenues par Cryo-TEM ont corroboré les morphologies sphériques des nano-objets.

L'interaction entre les nanoparticules et la protéine Annexine-A5 en présence de ions Ca^{2+} a été confirmée par LS, QCM-D et PAGE. En général, une augmentation significative du diamètre des objets a été détectée par LS après décoration par la protéine. De plus, une importante augmentation de l'intensité de lumière diffusée à été observé en réponse au changement de la masse/densité des particules (présence de protéine à la surface). Cette liaison est reversée par l'adition d'un agent complexant (EGTA) spécifique des ions Ca^{2+}. Pour le système PS-*b*-P(PEMA-*stat*-HEMA), les analyses de QCM-D et PAGE ont révélé que les propriétés des assemblages dépendent de la densité des groupes phosphate dans la couronne. En augmentant la quantité de fonctions capable de se lier à l'Annexine-A5, le nombre de protéines liées à la surface augmente.

Finalement, le présent travail de thèse a démontré qu'il est possible de préparer de manière assez simple des nanostructures à base des copolymères à bloc qui peuvent se lier à l'Annexine-A5. Les propriétés de ses systèmes sont contrôlables à partir des dimensions et fonctionnalités des unimères.

Les perspectives de ce travail sont centrées sur i) le développement (synthèse et auto-assemblage) des structures qui donneront lieu à des nanoparticules creuses en solution telles que des vésicules, ii) l'étude de l'auto-assemblage en masse de ces systèmes en vue de la préparation de bio-puces où l'Annexine-A5 pourra être précisément positionnée dans certaines nano-phases.

Experimental Part

The present section describes the experimental procedures for the synthesis, characterization and manipulation of block copolymers herein investigated. It also includes the protocol used to prepare the phospholipids vesicles and the equipments and setups applied during this work.

Chemicals

Triethylamine (Et3N, (C2H5)3N, 99%, Acros) and THF (J.T.Baker) were distilled over BaO and Na/benzophenone, respectively. Toluene (J.T.Baker) were distilled over polystyryllithium. Other solvents were of the highest available purity and used without any further purification.

The lipids dioleoylphosphatidylcholine (DOPC) and dioleoylphosphatidylserine (DOPS) were purchased from Avanti Polar Lipids (AL).

All other solvents and chemicals were of the highest purity available from Aldrich, and were used without any further purification.

Synthesis of the PECVPD-*B*-PBuA diblock copolymer

Synthesis of bromo-terminated poly(n-butyl acrylate) (PBuA) macroinitiator

Butyl acrylate (BuA) monomer (20 mL, 140 mmol), ethyl α-bromoisobutyrate (EBriBu) initiator (0.29 mL, 2.0 mmol), PMDETA ligand (0.84 mL, 4.0 mmol) were charged to 100 mL dry Schlenk tube along with toluene (20 mL) as the solvent (50% v/v) and mesitylene (1.0 mL) as internal 1H NMR standard. The tube was sealed with a rubber septum and subjected to three freeze-pump-thaw cycles. This solution was then cannulated under nitrogen into another Schlenk tube, previously evacuated and filled with nitrogen, containing Cu(I)Br (0.29 g, 2.0 mmol) and a magnetic stirrer. The solution was then immediately immersed in an oil bath at 70°C to start the polymerization. The polymerization was stopped after 75 min. (59% conversion as judged by ^{1}H NMR) by cooling down to room temperature and opening the flask to air. The mixture was then dissolved in 10 mL of THF and passed through basic alumina column to remove the used ATRP

catalyst. The final pure product was obtained after precipitating in a MeOH/H_2O 70/30 (v/v) mixture at -50°C and drying under vacuum.

Dimethyl(1-ethoxycarbonyl)vinyl phosphate monomer synthesis.

Dimethyl(1-ethoxycarbonyl)vinyl phosphate (DECVP) was synthesized as described by Barton et al.[117]. Trimethyl phosphite (9.9 g, 0.08 mol) was added dropwise to a stirred solution of ethyl bromopyruvate (15.5 g, 0.08 mol) at 0 °C under nitrogen. The reaction mixture was subsequently allowed to warm to room temperature under stirring for 1 h, and then at 50 °C for 1 h. The product was isolated by reduced pressure distillation at 98-102 °C, (60% yield). 1H NMR (CDCl3) δ (ppm): 1.12 (t, 3H), 3.66 (d, 6H), 4.06 (q, 2H), 5.39 (t, 1H), 5.75 (t, 1H). 13C NMR (CDCl3) δ (ppm): 13.7, 54.8, 61.6, 110.6, 143.5, 161.2.

Synthesis of PDECVP-b-PBuA diblock copolymer.

In a typical procedure, PBuA-Br macroinitiator (0.97 g, 0.22 mmol), DECVP monomer (4.84 g, 22 mmol), HMTETA ligand (0.059 mL, 0.22 mmol), and 2-butanone (5.0 mL) were charged to a dry 100 mL Schlenk flask. After three freeze-pump-thaw cycles carried out to remove dissolved oxygen, the solution was cannulated under nitrogen into another Schlenk tube, previously evacuated and filled with nitrogen, containing Cu(I)Br (0.03 g, 0.22 mmol) and a magnetic stirrer. The mixture was stirred and immersed in an oil bath at 70 ^{o}C. Under these experimental conditions, the conversion of DECVP monomer progressed up to 33% after 4 h, and no further chain extension was observed for longer reaction times. Presumably, this phenomenon is due to premature termination[118]. After 4h the reaction was stopped by cooling at room temperature and opening the flask to air. The mixture was then dissolved in 10 mL of acetone and passed through neutral alumina column in order to remove the spent ATRP catalyst. The final pure product was obtained after precipitation in cold *n*-hexane.

Conversion of poly(dimethyl(1-ethoxycarbonyl)vinyl phosphate) (PDECVP) into poly (1- ethoxycarbonil)vinylphosphonic diacid) (PECVPD)

PDEVCP-b-PBuA (1.5 g, 8.0 mmol phosphate groups) was dissolved in 15 mL of CH_2Cl_2 placed in a 50 mL round-bottom flask. Subsequently, 6.2 mL (37.8 mmol) of $BrSi(CH_3)_3$ was added dropwise, and the mixture was stirred at room temperature for 16 h, and solvents were removed under dynamic vacuum. In the next step, an excess of methanol (15 mL) was added to the silytaded product to induce methanolysis. The solution mixture was stirred at room temperature for 12 h, and the solvent was then evaporated. A slightly yellow powder was obtained after washing with ethyl ether. 1H NMR of the resulting compound confirmed complete conversion of –P(O)(OCH3)2 groups into –P(O)(OH)2 diacid groups.

Synthesis of the PS-b-P(PEMA-co-HEMA) diblock copolymer

Synthesis of PS macroinitiators

Styrene monomer (20 mL, 174 mmol), EBriBu initiator (0.51 mL, 3.5 mmol), and PMDETA ligand (0.36 mL, 1.7 mmol) were put into a 100 mL dry Schlenk tube. The tube was sealed with a rubber septum and subjected to three freeze-pump-thaw cycles in order to remove dissolved oxygen. This mixture was then cannulated under nitrogen into another Schlenk tube, previously evacuated and filled with nitrogen, containing Cu(I)Br (0.25 g, 1.7 mmol) and a magnetic stirrer. The tube was then immediately immersed in an oil bath at 100 ^{o}C to start the polymerization. The polymerization was stopped after a given period of time by cooling down to room temperature and opening the flask to air. The mixture was then dissolved in 100 mL of THF and passed through neutral alumina column to remove the used ATRP catalyst. The final pure product was isolated after precipitation (three times) in MeOH and dried under vacuum.

Synthesis of PS-b-PHEMA block copolymer

In a typical ATRP procedure, HEMA monomer (2.0 mL, 16.5 mmol) and a mixture of methyl ethyl ketone (MEK)/1-propanol (70/30 v/v) as solvent (4.0 mL) were put in a dry 100 mL Schlenk flask. The tube was sealed with a rubber septum and subjected to three freeze-pump-thaw cycles, then the solution was cannulated under nitrogen into another Schlenk tube, previously evacuated and filled with nitrogen, containing Cu(I)Cl (0.04 g, 0.41 mmol), PS_{30}-Br macroinitiator (1.26 g, 0.41 mmol), bpy ligand (0.13 g, 0.82 mmol), and a magnetic stirrer. The reaction mixture became immediately dark brown and progressively more viscous, indicating the onset of polymerization. After 50 min at 50°C, ^{1}H NMR analysis indicated that 70% of HEMA had been polymerized. The reaction was then stopped by opening the flask to air and adding 50 mL of an aerated MEK/1-propanol (70/30 v/v) mixture. The mixture was subsequently passed through a neutral alumina column in order to remove the spent ATRP catalyst. The final white product was obtained after selective precipitation in heptane, whereupon the unreacted PS macroinitiator was eliminated. It is interesting to note that even though heptane is a bad solvent for PS, low molecular weight PS chains remain solubilised in the medium while the diblock precipitates (see below).

Phosphorylation of PS-b-PHEMA

PS-*b*-PHEMA (0.50 g, 2.87 mmol of hydroxyl groups) was dissolved in 5.0 mL of dry THF placed in a 50 mL round-bottom flask. Subsequently, Et_3N (0.40 mL, 2.87 mmol) was added to this solution followed by dropwise addition of diethyl chlorophosphate (0.41 mL, 2.87 mmol). After 24 h under stirring at room temperature, the mixture was filtered to remove solid by-products ($Et_3N^+Cl^-$) and, volatiles were evaporated under vacuum. The resulting solids were re-dissolved in acetone and precipitated in 70 mL of heptane. The substitution degree of hydroxyl moieties in the final polystyrene-*b*-poly(2-hydroxyethyl methacrylate-*co*-diethyl phosphatethyl methacrylate) PS-*b*-P(DEPEMA-*co*-HEMA) polymer could be easily controlled by adjusting the reaction stoichiometry.

Conversion of PS-*b*-P(DEPEMA-co-HEMA) into PS-*b*-P(PEMA-co-HEMA)

PS-*b*-P(DEPEMA-*co*-HEMA) (0.5 g, 2.60 mmol of phosphate ester groups) was dissolved in 5 mL of CH_2Cl_2 placed in a 50 mL round-bottom flask. Subsequently, 1.37 mL (10.4 mmol) of $BrSi(CH_3)_3$ was added dropwise, and the mixture was stirred at room temperature overnight. Next, volatiles were removed under dynamic vacuum. The sylilation of $-P(O)(OCH_3CH_2)_2$ functional groups in this intermediate step was confirmed by ^{1}H NMR analysis, which showed the disappearance of $-P(O)(OCH_3CH_2)_2$ signal at 4.3 – 4.0 ppm, whereas typical chemical shift of sylilated residues appeared at low field [118, 138]. In the next step, 10 mL of MeOH/THF (50/50 v/v) was added to the silytaded product to induce methanolysis. The solution mixture was stirred at room temperature for 12 h, and the solvent was then evaporated. A slightly yellow powder was obtained after washing with ethyl ether. ^{1}H NMR of the resulting compound confirmed complete conversion of $-P(O)(OCH_3CH_2)_2$ groups into $-P(O)(OH)_2$ diacid groups.

Molecular Characteristics of Initiators and Polymers

Gel Permeation Chromatography (GPC)

Unless otherwise indicated, number average molar mass (M_n) and molar mass distribution (M_w/M_n) values were determined by GPC either in THF at a flow rate of 1.0 mL/min using a PLgel 5 μm Mixed-C column on a Jasco apparatus equipped with a refractive index detector or in DMF containing 1.0 g/L LiBr at a flow rate of 1.0 mL/min using a series of two PLgel 5 μm Mixed-C columns, equally on Jasco equipment. Calibration was performed using a series of near-monodisperse polystyrene (PS) standards in both cases.

Nuclear Magnetic Resonance spectroscopy (NMR)

400 MHz ^{1}H and 100 MHz ^{13}C NMR spectra were acquired using an Avance DPX 400 spectrometer. The solvent used for the analyses depended on the polymer solubility properties, and is indicated for each particular case.

Preparation of the Small unilamellar vesicles

A lipid mixture containing 80% DOPC and 20% DOPS was dissolved in chloroform. To form Small Unilamellar Vesicles (SUVs), lipids were dried under vacuum for 30 min, and then homogenized by five cycles of freeze-thawing before being resuspended in a buffer solution at a final concentration of 5.0 mg/ml and sonicated with a tip-sonicator ((Misonix, NY) operating in a pulsed mode at 30% duty cycle for 30 min with refrigeration, followed by centrifugation in an Eppendorf centrifuge (10 min at 16,000 g) to remove titanium particles. SUV suspensions were stored at 4 °C under nitrogen.

Physical Chemical Properties of Nanosized Assemblies

Static and Dynamic Light Scattering (SDLS)

SDLS measurements were performed using an ALV laser goniometer, which consists of a 22 mW HeNe linear polarized laser operating at a wavelength of 632.8 nm and an ALV-5000/EPP multiple τ digital correlator with 125 ns initial sampling time. The copolymer solutions were maintained at a constant temperature of 25.0 ± 0.1 °C in all experiments. The accessible scattering angles range from 15° to 150°. The solutions were placed in 10 mm diameter glass cells. The minimum sample volume required for DLS experiments was 1 mL. Data were collected using ALV Correlator Control software and the counting time varied for each sample from 300 to 900 s.

Transmission Electron Microscopy (TEM)

TEM images were recorded using a CM 120 Philips microscope operating at 120 kV, and equipped with a 2k x 2k USC1000-SSCCD Gatan camera. To prepare the TEM samples, 5 μL of an aqueous solution of block copolymer micelles was dropped onto a carbon-coated copper grid, which was rendered hydrophilic by UV/ozone treatment. Excess micelle solution was gently removed using absorbent paper. Samples were then negatively stained by adding a 5 μL droplet of 2% sodium phosphotungstate solution at pH 7.4 or 1% uranyl acetate solution at pH 3.95, and the excess solution was again removed prior to drying under ambient conditions.

Cryo-Transmission Electron Microscopy (Cryo-TEM).

A Leica CPC quench-freezing device was used to prepare cryo-TEM specimens. Drops of sample were deposited on holey carbon films. After blotting the excess of liquid with a filter paper, the grids were immediately plunged into liquid ethane cooled to -170 ^{o}C with liquid nitrogen. The grids were mounted on a Gatan 626 cryoholder, transferred into the microscope, and kept at a temperature of about -175 ^{o}C. EM was performed with a Tecnai-F20 FEI-transmission electron microscope, operating at 200 kV. Low-dose images were recorded at a nominal magnification of 50,000x with a 2k x 2k USC1000 slow-scan CCD camera.

Potentiometric Titration

Systems exhibiting pH-dependency were studied by potentiometry. Copolymer solutions at pH = 3.0 were prepared as previously described above. Potentiometric titrations curves were obtained by monitoring the pH increase as a function of added 0.010 mol/L NaOH (increments of 0.025 mL in a 5.0 mL aliquot of 1.0 mg/mL diblock copolymer-containing solution). The pH measurements were performed using a Mettler Toledo pH-meter coupled to an InLab 423 combined pH electrode, and titration curves in the pH range of 3 to 10 were recorded.

Fluorescence analysis

Fluorescence analysis was used for dipyridamole quantification in PMPC-b-PDPA micelles. The loading efficiency was determined using the standard addition analytical method, which is suitable to avoid any possible matrix effects on the quantum yield of DIP fluorescence. Drug-loaded micelles were dissolved in citric acid/sodium citrate buffer at pH = 3.0 to induce dissociation and to ensure a constant fluorescence quantum yield of DIP in aqueous solution. The fluorescence emission intensity at 490 nm (λ_{exc} = 415 nm) was measured as a function of known added aliquots (25, 50, 75, 100, 150, 200 μL) of 3.8 x 10^{-3} mol dm^{-3} DIP. Linear fitting of experimental points generated straight lines, from which the 'negative volume' of added DIP corresponding to zero fluorescence intensity was obtained, and accordingly the amount of DIP present in the original copolymer solution was calculated.

PolyAcrylamide Gel Electrophoresis (PAGE)

PAGE was performed in 1.0 mm thick slab gels. Separating gels contained 8% acrylamide and 0.05% bis-acrylamide in 400 mM Tris (pH 8.8). Before deposition on the gel, the samples (20 or 40 μL maximal volume) were mixed with 5 μL of a solution containing Bromophenol blue in 30% glycerol. The migration buffer was 25 mM Tris, 192 mM glycine (pH 8.3). For block copolymer micelles, experiments were carried in the absence of SDS and, in absence and presence of Ca^{2+}. Gels were stained with Coomassie brilliant blue according to standard procedures.

Quartz Crystal microbalance with dissipation monitoring (QCM-D)

QCM-D measurements were performed with a Q-SENSE D300 system equipped with an Axial Flow Chamber (QAFC 301) (Q-SENSE AB, Gothenburg, Sweden). Briefly, upon interaction of (soft) matter with the surface of a sensor crystal, changes in the resonance frequency, *F*, related to attached mass (including coupled water), and in the dissipation, *D*, related to frictional (viscous) losses in the adlayer are measured with a time resolution of better than 1 s. Measurements in liquid environment were performed at a working temperature of 24 °C in exchange mode. Resonance frequency and dissipation were measured at several harmonics (15, 25, 35 MHz) simultaneously. If not stated otherwise, (i) changes in dissipation and normalized frequency ($\Delta F_{norm} = \Delta F_n/n$, with n being the overtone number) are presented and (ii) adsorbed masses, Δm, are calculated according to the Sauerbrey equation, $\Delta m = -C \times \Delta F_{norm}$, with $-C = 17.7$ ng.cm^{-2}.Hz^{-1}.

Small Angle X-Ray Scattering (SAXS)

SAXS measurements were performed at the high brilliance beam line ID02, European Synchrotron Radiation Facility (ESRF), Grenoble, France.[139] A combination of different sample-to-detector distances was used in order to explore a wide *q*-range, spanning from 0.01 nm^{-1} up to 1 nm^{-1}, for a λ of 0.1 nm, assuming $n \approx 1$ for SAXS.

The SAXS detector was an X-ray image intensifier lens coupled to a fast-readout CCD camera (FReLoN) placed in an evacuated flight tube. Solutions were loaded in a temperature controlled vacuum flow-through cell (diameter ~2 mm), in order to reduce the background for

low scattering liquid samples. In addition to the lower background, the sample and solvent scattering can be measured at the same place allowing very reliable subtraction.

References

1. Bérat, R.; Rémy-Zolghadry, M.; Gounou, C.; Manigand, C.; Tan, S.; Saltó, C.; Arenas, E.; L., B.; Brisson, A. R., Peptide-presenting 2D protein matrix on supported lipid bilayers: an efficient platform for cell adhesion. *Biointerphases* **2007,** 2, (4), 165-172.

2. Brisson, A. R. A device for binding a targeting entity to a bait entity and detection methods using the same. WO 2005/114192, 2005.

3. Förster, S.; Plantenberg, T., From self-organizing polymers to nanohybrid and biomaterials. *Angew. Chem., Int. Ed.* **2002,** 41, (5), 688-714.

4. Bucknall, D. G.; Anderson, H. L., Polymers get organized. *Science* **2003,** 302, 1904-1905.

5. Lasic, D. D., Novel applications of liposomes. *Trends in Biotechnology* **1998,** 16, (7), 307-321.

6. Santos, N. C.; Castanho, M. A. R. B., Lipossomas: a bala mágica acertou? *Química Nova* **2002,** 25, (6b), 1181-1185.

7. Forssen, E.; Willis, M., Ligand-targeted liposomes. *Advanced Drug Delivery Reviews* **1998,** 29, (3), 249-271.

8. Graff, A.; Benito, S. M.; Verbert, C.; Meier, W., *Polymer Nanocontainers*. WILEY-VCH: Weinheim, GE, 2004; p 454.

9. Lasic, D. D.; Templeton, N. S., Liposomes in gene therapy. *Adv. Drug Deliv. Rev.* **1996,** 20 221-266.

10. Gerke, V.; Moss, S. E., Annexins: From structure to function. *Physiol. Rev.* **2002,** 82, (2), 331-371.

11. Sopkova-de Oliveira Santos, J.; Fischer, S.; Guilbert, C.; Lewit-Bentley, A.; Smith, J. C., Pathway for Large-Scale Conformational Change in Annexin V. *Biochemistry* **2000,** 39, (46), 14065-14074.

12. Richter, R. P.; Lai-Kee-Him, J.; Brisson, A., Supported Lipid Membranes. *Materials Today* **2003,** November, 32-37.

13. Reutelingsperger, C. P. M.; Dumont, E.; Thimister, P. W.; van Genderen, H.; Kenis, H.; van de Eijnde, S.; Heidendal, G.; Hofstra, L., Visualization of cell death in vivo with the annexin A5 imaging protocol. *Journal of Immunological Methods* **2002,** 265, (1-2), 123-132.

14. Manon van Engeland, L. J. W. N. F. C. S. R. B. S. C. P. M. R., Annexin V-Affinity assay: A review on an apoptosis detection system based on phosphatidylserine exposure. *Cytometry* **1998,** 31, (1), 1-9.

15. van Tilborg, G. A. F.; Mulder, W. J. M.; Deckers, N.; Storm, G.; Reutelingsperger, C. P. M.; Strijkers, G. J.; Nicolay, K., Annexin A5-functionalized bimodal lipid-based contrast agents for the detection of apoptosis. *Bioconjugate Chemistry* **2006,** 17, (3), 741-749.

16. Hadjichristidis, N.; Pitsikalis, M.; Iatrou, H., Synthesis of block copolymers. *Adv. Polym. Sci.* **2005,** 189, 1-124.

17. Taton, D.; Gnanou, Y., Guidelines for Synthesizing Block Copolymers. In *Block Copolymers in Nanoscience*, Lazzari, M.; Liu, G.; Lecommandoux, S., Eds. Wiley-VCH Verlag GmbH & Co.: Darmstadt, 2006; pp 9-35.

18. Bernaerts, K. V.; Du Prez, F. E., Dual/heterofunctional initiators for the combination of mechanistically distinct polymerization techniques. *Prog. Polym. Sci.* **2006,** 31, (8), 671-722.

19. Lazzari, M.; López-Quintela, A., Block copolymers as a tool for nanomaterial fabrication. *Adv. Mater.* **2003,** 15, (19), 1583-1594.

20. Deming, T. J., Methodologies for preparation of synthetic block copolypeptides: materials with future promise in drug delivery. *Adv. Drug Deliver. Rev.* **2002,** 54, (8), 1145-1155.

21. Klok, H.-A.; Lecommandoux, S., Supramolecular materials via block copolymer self-assembly. *Adv. Mater.* **2001,** 13, (16), 1217-1229.

22. Fontanille, M.; Gnanou, Y., *Chimie et Physico-Chimie des Polymères*. Dunod: Paris, 2002.

23. Matyjaszewski, K.; Davis, T. P., *Handbook of Radical Polymerization*. Wiley-Interscience: New York, 2002.

24. Riess, G., Micellization of block copolymers. *Prog. Polym. Sci.* **2003,** 28, (7), 1107-1170.

25. Ladmiral, V.; Melia, E.; Haddleton, D. M., Synthetic glycopolymers: an overview. *Eur. Polym. J.* **2004,** 40, (3), 431-449.

26. Lecolley, F.; Waterson, C.; Carmichael, A. J.; Mantovani, G.; Harrisson, S.; Chappell, H.; Limer, A.; Williams, P.; K., O.; Haddleton, D. M., Synthesis of functional polymers by living radical polymerisation. *J. Mater. Chem.* **2003,** 13, 2689 - 2695.

27. Taton, D.; Gnanou, Y.; Matmour, R.; Angot, S.; Hou, S.; Francis, R.; Lepoittevin, B.; Moinard, D.; Babin, J., Controlled polymerizations as tools for the design of star-like and dendrimer-like polymers. *Polym. Int.* **2006,** 55, (10), 1138-1145.

28. Wang, J. S.; Matyjaszewski, K., Controlled/"living" radical polymerization. atom transfer radical polymerization in the presence of transition-metal complexes *J. Am. Chem. Soc.* **1995,** 117, 5614.

29. Kato, M.; Kamigaito, M.; Sawamoto, M.; Higashimura, T., Polymerization of methyl methacrylate with the carbon tetrachloride/dichlorotris-(triphenylphosphine)ruthenium(II)/methylaluminum bis(2,6-di-tert-butylphenoxide) initiating system: Possibility of Living Radical Polymerization. *Macromolecules* **1995,** 28, (5), 1721-1723.

30. Xia, J.; Matyjaszewski, K., Atom transfer radical polymerization. *Chem. Rev.* **2001,** 101, 2921-2990.

31. Matyjaszewski, K., Transition metal catalysis in controlled radical polymerization: Atom transfer radical polymerization. *Chem.-Eur. J.* **1999,** 5, (11), 3095-3102.

32. Patten, T. E.; Matyjaszewski, K., Atom transfer radical polymerization and the synthesis of polymeric materials. *Adv. Mater.* **1998,** 10, (12), 901-915.

33. Kamigaito, M.; Ando, T.; Sawamoto, M., Metal-catalyzed living radical polymerization. *Chem. Rev.* **2001,** 101, (12), 3689-3746.

34. Park, C.; Yoon, J.; Thomas, E. L., Enabling nanotechnology with self assembled block copolymer patterns. *Polymer* **2003,** 44, (22), 6725-6760.

35. Matsen, M. W.; Bates, F. S., Unifying Weak- and Strong-Segregation Block Copolymer Theories. *Macromolecules* **1996,** 29, (4), 1091-1098.

36. Bates, F. S.; Fredrickson, G. H., Block copolymers-designer soft materials. *Physics Today* **1999,** 52, (2), 32-38.

37. Abetz, V.; Simon, P. F. W., Phase behavior and morphologies of block copolymers. *Adv. Polym. Sci.* **2005,** 189, 125-212.

38. Bates, F. S.; Fredrickson, G. H., Block copolymer thermodynamics: Theory and experiment. *Annu. Rev. Phys. Chem.* **1990,** 41, 525-557.

39. Leibler, L., Theory of Microphase Separation in Block Copolymers. *Macromolecules* **1980,** 13, (6), 1602-1617.

40. Matsen, M. W., Equilibrium behavior of asymmetric ABA triblock copolymer melts. *Journal of Chemical Physics* **2000,** 113, (13), 5539-5544.

41. Hamley, I. W., *Block Copolymers in Solution: Fundamentals and Applications*. Wiley New York, 2005.

42. Lodge, T. P.; Pudil, B.; Hanley, K. J., The full phase behavior of block copolymers in solvents of varying selectivity. *Macromolecules* **2002,** 35, 4707-4717.

43. Discher, B. M.; Won, Y.-Y.; Ege, D. S.; Lee, J. C.-M.; Bates, F. S.; Discher, D. E.; Hammer, D. A., Polymersomes: Though vesicles made from diblock copolymers. *Science* **1999,** 284, 1143–1146.

44. Discher, B. M.; Hammer, D. A.; Bates, F. S.; Discher, D. E., Polymer vesicles in various media. *Curr. Opin. Colloid Interface Sci.* **2000,** 5, (1-2), 125-131.

45. Allen, C.; Maysinger, D.; Eisenberg, A., Nano-engineering block copolymer aggregates for drug delivery. *Colloid Surf. B-Biointerfaces* **1999,** 16, (1-4), 3-27.

46. Letchford, K.; Burt, H., A review of the formation and classification of amphiphilic block copolymer nanoparticulate structures: micelles, nanospheres, nanocapsules and polymersomes. *European Journal of Pharmaceutics and Biopharmaceutics* **2007,** 65, (3), 259-269.

47. Cameron, N. S.; Corbierre, M. K.; Eisenberg, A., 1998 E.W.R. Steacie Award Lecture Asymmetric amphiphilic block copolymers in solution: a morphological wonderland. *Canadian Journal Chemistry* **1999,** 77, 1311-1326.

48. Riley, T.; Stolnik, S.; Heald, C. R.; Xiong, C. D.; Garnett, M. C.; Illum, L.; Davis, S. S.; Purkiss, S. C.; Barlow, R. J.; Gellert, P. R., Physicochemical evaluation of nanoparticles assembled from poly(lactic acid)-poly(ethylene glycol) (PLA-PEG) block copolymers as drug delivery vehicles. *Langmuir* **2001,** 17, (11), 3168-3174.

49. Heald, C. R.; Stolnik, S.; Kujawinski, K. S.; De Matteis, C.; Garnett, M. C.; Illum, L.; Davis, S. S.; Purkiss, S. C.; Barlow, R. J.; Gellert, P. R., Poly(lactic acid)-Poly(ethylene oxide) (PLA-PEG) Nanoparticles: NMR Studies of the Central Solidlike PLA Core and the Liquid PEG Corona. *Langmuir* **2002,** 18, (9), 3669-3675.

50. Halperin, A., Polymeric micelles: a star model. *Macromolecules* **1987,** 20, (11), 2943-2946.

51. Forster, S.; Zisenis, M.; Wenz, E.; Antonietti, M., Micellization of strongly segregated block copolymers. *J. Chem. Phys.* **1996,** 104, (24), 9956-9970.

52. Gao, Z. S.; Varshney, S. K.; Wong, S.; Eisenberg, A., Block-Copolymer Crew-Cut Micelles in Water. *Macromolecules* **1994,** 27, (26), 7923-7927.

53. Babin, J. Synthèse et auto-assemblage de copolymères amphiphiles en étoile de type miktoarm. University of Bordeaux I (France), 2006.

54. Astafieva, I.; Khougaz, K.; Eisenberg, A., Micellization in block polyelectrolyte solutions. 2. Fluorescence study of the critical micelle concentration as a function of soluble block length and salt concentration. *Macromolecules* **1995,** 28, (21), 7127-7134.

55. Groenewegen, W.; Egelhaaf, S. U.; Lapp, A.; van der Maarel, J. R. C., Neutron scattering estimates of the effect of charge on the micelle structure in aqueous polyelectrolyte diblock copolymer solutions. *Macromolecules* **2000,** 33, (9), 3283-3293.

56. Zhang, L. F.; Eisenberg, A., Formation of crew-cut aggregates of various morphologies from amphiphilic block copolymers in solution. *Polym. Adv. Technol.* **1998,** 9, (10-11), 677-699.

57. Zhang, L. F.; Shen, H. W.; Eisenberg, A., Phase separation behavior and crew-cut micelle formation of polystyrene-b-poly(acrylic acid) copolymers in solutions. *Macromolecules* **1997,** 30, (4), 1001-1011.

58. Shen, H. W.; Eisenberg, A., Morphological phase diagram for a ternary system of block copolymer PS310-b-PAA(52)/dioxane/H2O. *J. Phys. Chem. B* **1999,** 103, (44), 9473-9487.

59. Borsali, R., In *Handbook of Polyelectrolytes and Their Applications*, Tripathy, S. K.; Kumar, J.; Nalwa, S., Eds. American Scientific Publishers: Los Angeles, 2002; pp 249-265.

60. Borsali, R., Scattering properties of weakly charged polyelectrolytes. *Phys. Chem. Chem. Phys.* **1996,** 100, (6), 836-840.

61. Borsali, R., Scattering properties of multicomponent polymer solutions: Polyelectrolytes, homopolymer mixtures and diblock copolymer. *Macromol. Chem. Phys.* **1996,** 197, (12), 3947-3994.

62. Zupancich, J. A.; Bates, F. S.; Hillmyer, M. A., Aqueous dispersions of poly(ethylene oxide)-b-poly(gamma-methyl-epsilon-caprolactone) block copolymers *Macromolecules* **2006,** 39, 4286-4288.

63. Geng, Y.; Discher, D. E., Hydrolytic degradation of poly(ethylene oxide)-block-polycaprolactone worm micelles *J. Am. Chem. Soc.* **2005,** 127, 12780-12781.

64. Bae, K. H.; Lee, Y.; Park, T. G., Oil-encapsulating PEO-PPO-PEO/PEG shell cross-linked nanocapsules for target-specific delivery of paclitaxel. *Biomacromolecules* **2007,** 8, (2), 650-656.

65. Ballauff, M.; Borisov, O., Polyelectrolyte brushes. *Current Opinion in Colloid & Interface Science* **2006,** 11, (6), 316-323.

66. Guenoun, P.; Muller, F.; Delsanti, M.; Auvray, L.; Chen, Y. J.; Mays, J. W.; Tirrell, M., Rodlike behavior of polyelectrolyte brushes. *Physical Review Letters* **1998,** 81, (18), 3872-3875.

67. Wittemann, A.; Ballauff, M., Interaction of proteins with linear polyelectrolytes and spherical polyelectrolyte brushes in aqueous solution. *Phys Chem Chem Phys* **2006,** 8, 5269-5275.

68. Zhou, F.; Huck, W. T. S., Surface grafted polymer brushes as ideal building blocks for "smart" surfaces. . *Phys Chem Chem Phys* **2006,** 8, 3815-3823.

69. Förster, S.; Abetz, V.; Müller, A. H. E., Polyelectrolyte block copolymer micelles. *Adv. Polym. Sci.* **2004,** 166, 173-210.

70. Hales, K.; Pochan, D. J., Using polyelectrolyte block copolymers to tune nanostructure assembly. *Current Opinion in Colloid & Interface Science* **2006,** 11, (6), 330-336.

71. Förster, S.; Schmidt, M., *Adv. Polym. Sci.* **1995,** 120, 51-133.

72. Muller, F.; Guenoun, P.; Delsanti, M.; Deme, B.; Auvray, L.; Yang, J.; Mays, J. W., Spherical polyelectrolyte block copolymer micelles: Structural change in presence of monovalent salt. *European Physical Journal E* **2004,** 15, (4), 465-472.

73. Romet-Lemonne, G.; Daillant, J.; Guenoun, P.; Yang, J.; Mays, J. W., Thickness and density profiles of polyelectrolyte brushes: Dependence on grafting density and salt concentration. *Physical Review Letters* **2004,** 93, (14).

74. Roger, M.; Guenoun, P.; Muller, F.; Belloni, L.; Delsanti, M., Monte Carlo simulations of star-branched polyelectrolyte micelles. *European Physical Journal E* **2002,** 9, (4), 313-326.

75. Forster, S.; Hermsdorf, N.; Bottcher, C.; Lindner, P., Structure of Polyelectrolyte Block Copolymer Micelles. *Macromolecules* **2002,** 35, (10), 4096-4105.

76. Norwood, D. P.; Benmouna, M.; Reed, W. F., Static Light Scattering from Mixtures of Polyelectrolytes in Low Ionic Strength Solutions. *Macromolecules* **1996,** 29, (12), 4293-4304.

77. Sorci, G. A.; Reed, W. F., Electrostatically Enhanced Second and Third Virial Coefficients, Viscosity, and Interparticle Correlations for Linear Polyelectrolytes. *Macromolecules* **2002,** 35, (13), 5218-5227.

78. Broz, P.; Benito, S. M.; Saw, C.; Burger, P.; Heider, H.; Pfisterer, M.; Marsch, S.; Meier, W.; Hunziker, P., Cell targeting by a generic receptor-targeted polymer nanocontainer platform. *Journal of Controlled Release* **2005,** 102, (2), 475-488.

79. Glidle, A.; Yasukawa, T.; Hadyoon, C. S.; Anicet, N.; Matsue, T.; Nomura, M.; Cooper, J. M., Analysis of Protein Adsorption and Binding at Biosensor Polymer Interfaces Using X-ray Photon Spectroscopy and Scanning Electrochemical Microscopy. *Anal. Chem.* **2003,** 75, (11), 2559-2570.

80. Vazquez-Dorbatt, V.; Maynard, H. D., Biotinylated Glycopolymers Synthesized by Atom Transfer Radical Polymerization. *Biomacromolecules* **2006,** 7, (8), 2297-2302.

81. Raichur, A. M.; Voros, J.; Textor, M.; Fery, A., Adhesion of Polyelectrolyte Microcapsules through Biotin-Streptavidin Specific Interaction. *Biomacromolecules* **2006,** 7, (8), 2331-2336.

82. Wittemann, A.; Azzam, T.; Eisenberg, A., Biocompatible Polymer Vesicles from Biamphiphilic Triblock Copolymers and Their Interaction with Bovine Serum Albumin. *Langmuir* **2007,** 23, (4), 2224-2230.

83. Anikin, K.; Rocker, C.; Wittemann, A.; Wiedenmann, J.; Ballauff, M.; Nienhaus, G. U., Polyelectrolyte-Mediated Protein Adsorption: Fluorescent Protein Binding to Individual Polyelectrolyte Nanospheres. *J. Phys. Chem. B* **2005,** 109, (12), 5418-5420.

84. Wittemann, A.; Ballauff, M., Adsorption of proteins on spherical polyelectrolyte brushes in

aqueous solution. *Phys. Chem. Chem. Phys.* **2003,** 5, 1671-1677.

85. Jeff Y. Gao, P. L. D., Binding of proteins to copolymers of varying hydrophobicity. *Biopolymers* **1999,** 49, (2), 185-193.

86. Kusumo, A.; Bombalski, L.; Lin, Q.; Matyjaszewski, K.; Schneider, J. W.; Tilton, R. D., High Capacity, Charge-Selective Protein Uptake by Polyelectrolyte Brushes. *Langmuir* **2007,** 23, (8), 4448-4454.

87. Zhu, Y.; Chian, K. S.; Chan-Park, M. B.; Mhaisalkar, P. S.; Ratner, B. D., Protein bonding on biodegradable poly(l-lactide-co-caprolactone) membrane for esophageal tissue engineering. *Biomaterials* **2006,** 27, (1), 68-78.

88. Michel, R.; Pasche, S.; Textor, M.; Castner, D. G., Influence of PEG Architecture on Protein Adsorption and Conformation. *Langmuir* **2005,** 21, (26), 12327-12332.

89. Philipsen, H. J. A., Determination of chemical composition distributions in synthetic polymers. *Journal of Chromatography A* **2004,** 1037, (1-2), 329-350.

90. Trathnigg, B., *Size-Exclusion Chromatography of Polymers*. John Wiley & Sons Ltd.: 2000; p 26.

91. Engelhardt, H.; Mathes, D., High-performance liquid chromatography of proteins using chemically-modified silica supports. *Chromatographia* **1981,** 14, (6), 325-332.

92. W. W. Yau, H. J. S. D. D. B., Calibration and molecular weight calculations in GPC using a new practical method for dispersion correction - GPCV2. *Journal of Applied Polymer Science* **1977,** 21, (7), 1911-1920.

93. Pecora, R.; Berne, B. J., *Dynamic Light Scattering With Applications to Chemistry, Biology and Physics*. Dover Publications, INC: Mineola, NY, 2000.

94. Dalgleish, D. G. H., F. R., Dynamic light scattering: applications to food systems. *Food Research International* **1995,** 28, (3), 181-193.

95. Brown, W., *Dynamic Light Scattering. The Method and Some Applications*. Oxford University Press Inc.: New York, 1993.

96. Provencher, S. W., Inverse problems in polymer characterization: Direct analysis of polydispersity with photon correlation spectroscopy. *Makromol. Chem.* **1979,** 180, 201-209.

97. Koppel, D. E., Analysis of macromolecular polydispersity in intensity correlation spectroscopy: The method of cumulants *J. Chem. Phys.* **1972,** 57, (11), 4814-4820.

98. Pecora, R., Dynamic light scattering measurement of nanometer particles in liquids. *J. Nanopar. Res.* **2000,** 2, 123–130.

99. Mountrichas, G.; Mpiri, M.; Pispas, S., Micelles of star block (PSPI)8 and PSPI diblock copolymers (PS = polystyrene, PI = polyisoprene): Structure and kinetics of micellization. *Macromolecules* **2005,** 38, 940-947.

100. Burchard, W., Static and dynamic light scattering from branched polymers and biopolymers *Adv. Polym. Sci.* **1983,** 48, 1-124.

101. Checot, F.; Brulet, A.; Oberdisse, J.; Gnanou, Y.; Mondain-Monval, O.; Lecommandoux, S., Structure of polypeptide-based diblock copolymers in solution: Stimuli-responsive vesicles and micelles. *Langmuir* **2005,** 21, (10), 4308-4315.

102. Kotlarchyk, M.; Chen, S.-H., *Journal of Chemical Physics* **1983,** 79, 2461-2469.

103. Sztucki, M.; Narayanan, T., *J. Appl. Cryst.* **2007,** 40, s459-s462.

104. Brumberger, H., In *Modern Aspects of Small Angle Scattering*, Kluwer Academic: Dordrecht, 1995.

105. Giacomelli, C.; Schmidt, V.; Borsali, R., Nanocontainers formed by self-assembly of poly(ethylene oxide)-b-poly(glycerol monomethacrylate) – drug conjugates. *Macromolecules* **2007,** 40, 2148-2157.

106. Rodahl, M.; Hook, F.; Krozer, A.; Brzezinski, P.; Kasemo, B., Quartz crystal microbalance setup for frequency and Q-factor measurements in gaseous and liquid environments. *Review of Scientific Instruments* **1995,** 66, (7), 3924-3930.

107. Höök, F. Development of a novel QCM technique for protein adsorption studies. Chalmers University of Technology - Göteborg University, Göteborg, 2001.

108. Kalyanasundaran, K.; Thomas, J. K., Environmental effects on vibronic band intensities in pyrene monomer fluorescence and their application in studies of micellar systems. *J. Am. Chem. Soc.* **1977,** 99, 2039-2044.

109. Soo, P. L.; Luo, L. B.; Maysinger, D.; Eisenberg, A., Incorporation and release of hydrophobic probes in biocompatible polycaprolactone-block-poly(ethylene oxide) micelles: Implications for drug delivery. *Langmuir* **2002,** 18, (25), 9996-10004.

110. Richter, R. P.; Lai Kee Him, J.; Tessier, L.; Tessier, C.; Brisson, A. R., On the kinectics of adsorption and 2D.... *Biophys. J.* **2005,** 89, (November), 3372-3385.

111. Lambert, O.; Gerke, V.; Bader, M. F.; Porte, F.; Brisson, A., Structural analysis of junctions formed between lipid membranes and several annexins by cryo-electron microscopy. *Journal of Molecular Biology* **1997,** 272, (1), 42-55.

112. Reviakine, I.; Bergsma-Schutter, W.; Mazeres-Dubut, C.; Govorukhina, N.; Brisson, A., Surface topography of the p3 and p6 annexin V crystal forms determined by atomic force microscopy. *Journal of Structural Biology* **2000,** 131, (3), 234-239.

113. Richter, R.; Him, J. L. K.; Brisson, A., Supported Lipid Membranes. *Materials Today* **2003,** 6, 32-37.

114. Corsten, M. F.; Hofstra, L.; Narula, J.; Reutelingsperger, C. P. M., Counting Heads in the War against Cancer: Defining the Role of Annexin A5 Imaging in Cancer Treatment and Surveillance. *Cancer Research* **2006,** 66, 1255-1260.

115. Hellweg, T.; Eimer, W., The micro-structures formed by Ni 2 +-AOT/cyclohexane/water microemulsions: a light scattering study. *Colloids and Surfaces A: Physicochemical and Engineering Aspects* **1998,** 136, 97-107.

116. Yue, B.; Huang, C.; Nieh, M.; J., G. C.; Katsaras, J., Highly Stable Phospholipid Unilamellar Vesicles from Spontaneous Vesiculation: A DLS and SANS Study. *J. Phys. Chem. B* **2005,** 109, 609-616.

117. Barton, D. H. R.; Chern, C.-Y.; Jaszberenyi, J. C., The Invention of Radical Reactions. Part XXXIV. Homologation of Carboxylic Acids to a-Keto Carboxylic Acids by Barton-ester Based Radical Chain Chemistry. *Tetrahedron* **1995,** 51, (7), 1867-1886.

118. Huang, J.; Matyjaszewski, K., Atom Transfer Radical Polymerization of Dimethyl(1-ethoxycarbonyl)vinyl Phosphate and Corresponding Block Copolymers. *Macromolecules* **2005,** 38, (9), 3577-3583.

119. Colombani, O.; Ruppel, M.; Schubert, F.; Zettl, H.; Pergushov, D. V.; Muller, A. H. E., Synthesis of Poly(n-butyl acrylate)-block-poly(acrylic acid) Diblock Copolymers by ATRP and Their Micellization in Water. *Macromolecules* **2007**, DOI: 10.1021/ma0609578.

120. Li, X.; Reed, W. F., Polyelectrolyte properties of proteoglycan monomers. *J. Chem. Phys.* **1991,** 94, 4568-4580.

121. Moinard, D.; Borsali, R.; Taton, D.; Gnanou, Y., Scattering and Viscosimetric Behaviors of Four- and Six-Arm Star Polyelectrolyte Solutions. *Macromolecules* **2005,** 38, (16), 7105-7120.

122. Korobko, A. V.; Jesse, W.; Lapp, A.; Egelhaaf, S. U.; van der Maarel, J. R. C., Structure of strongly interacting polyelectrolyte diblock copolymer micelles. *Journal of Chemical Physics* **2005,** 122, (2).

123. Hariharan, R.; Biver, C.; Russel, W. B., Ionic Strength Effects in Polyelectrolyte Brushes: The Counterion Correction. *Macromolecules* **1998,** 31, (21), 7514-7518.

124. Muller, F.; Romet-Lemonne, G.; Delsanti, M.; Mays, J. W.; Daillant, J.; Guenoun, P., Salt-induced contraction of polyelectrolyte brushes. *J. Phys.: Condens. Matter.* **2005,** 17, (45).

125. Guenoun, P.; Davis, H. T.; Tirrell, M.; Mays, J. W., Aqueous Micellar Solutions of Hydrophobically Modified Polyelectrolytes. *Macromolecules* **1996,** 29, (11), 3965-3969.

126. Korobko, A. V.; Jesse, W.; Egelhaaf, S. U.; Lapp, A.; van der Maarel, J. R. C., Do spherical polyelectrolyte brushes interdigitate? *Physical Review Letters* **2004,** 93, (17).

127. Colombani, O.; Ruppel, M.; Burkhardt, M.; Drechsler, M.; Schumacher, M.; Gradzielski, M.; Schweins, R.; Muller, A. H. E., Structure of Micelles of Poly(n-butyl acrylate)-block-poly(acrylic acid) Diblock Copolymers in Aqueous Solution. *Macromolecules* **2007**, DOI: 10.1021/ma0609580.

128. Samokhina, L.; Schrinner, M.; Ballauff, M.; Drechsler, M., Binding of Oppositely Charged Surfactants to Spherical Polyelectrolyte Brushes: A Study by Cryogenic Transmission Electron Microscopy. *Langmuir* **2007,** 23, (7), 3615-3619.

129. Erhardt, R.; Zhang, M.; Boker, A.; Zettl, H.; Abetz, C.; Frederik, P.; Krausch, G.; Abetz, V.; Muller, A. H. E., Amphiphilic Janus Micelles with Polystyrene and Poly(methacrylic acid) Hemispheres. *J. Am. Chem. Soc.* **2003,** 125, (11), 3260-3267.

130. Suzuki, S.; Whittaker, M. R.; Grondahl, L.; Monteiro, M. J.; Wentrup-Byrne, E., Synthesis of Soluble Phosphate Polymers by RAFT and Their in Vitro Mineralization. *Biomacromolecules* **2006**, doi: 10.1021/bm060583q.

131. Davis, K. A.; Charleux, B.; K., M., Preparation of block copolymers of polystyrene and poly (t-butyl acrylate) of various molecular weights and architectures by atom transfer radical polymerization. *J. Polym. Sci. Part A* **2000,** 38, (12), 2274-2283.

132. Beers, K. L.; Boo, S.; Gaynor, S. G.; Matyjaszewski, K., Atom Transfer Radical Polymerization of 2-Hydroxyethyl Methacrylate. *Macromolecules* **1999,** 32, (18), 5772-5776.

133. Zhu, Q.; Huang, X.; Chen, G. Y. J.; Yao, S. Q., Activity-based fluorescent probes that target phosphatases. *Tetrahedron Letters* **2003,** 44, 2669-2672.

134. Giacomelli, C.; LeMen, L.; Borsali, R.; Lai-Kee-Him, J.; Brisson, A.; Armes, S. P.; Lewis, A. L., Phosphorylcholine-based pH-responsive diblock copolymer micelles as drug delivery vehicles: Light scattering, electron microscopy, and fluorescence experiments. *Biomacromolecules* **2006,** 7, (3), 817-828.

135. Kataoka, K.; Harada, A.; Nagasaki, Y., Block copolymer micelles for drug delivery: design, characterization and biological significance. *Adv. Drug Deliv. Rev.* **2001,** 47, (1), 113-131.

136. Matejicek, P.; Podhajecka, K.; Humpolickova, J.; Uhlik, F.; Jelinek, K.; Limpouchova, Z.; Prochazka, K.; Spirkova, M., Polyelectrolyte behavior of polystyrene-block-poly(methacrylic acid) micelles in aqueous solutions at low ionic strength. *Macromolecules* **2004,** 37, (26), 10141-10154.

137. Skoog, D. A.; West, D. M.; Holler, F. J., *Fundamentals of Analytical Chemistry*. 7th ed.; Saunders College Publishing: New York, 1996.

138. Schmidt, V.; Giacomelli, C.; Lecolley, F.; Lai-Kee-Him, J.; Brisson, A. R.; Borsali, R., Diblock copolymer micellar nanoparticles decorated with Annexin-A5 proteins. *J. Am. Chem. Soc.* **2006,** 128, (28), 9010-9011.

139. Narayanan, T.; Diat, O.; Boesecke, P., *Nucl. Instrum. Meth. A* **2001,** 467, 1005-1009.

List of Publications

Articles Published

1. **Schmidt, V**.; Giacomelli, C**.;** Lecolley, F.; Lai-Kee-Him, J.; Brisson, A. R.; Borsali, R. Diblock copolymer micellar nanoparticles decorated with annexin-a5 proteins, *J. Am. Chem. Soc.* **2006,** 128, (28), 9010-9011. http://dx.doi.org/10.1021/ja062408n

2. **Schmidt, V.**; Di Cola, E.; Giacomelli, C.; Brisson, A. R.; Narayanan, T.; Borsali, R. Polyelectrolyte Behavior of Diblock Copolymer Micelles Having Phosphonic Diacid Groups at the Corona**,** Macromolecules**;** **2008**; 41(6); 2195-2202. http://dx.doi.org/10.1021/ma702182p

3. **Schmidt, V.;** Giacomelli, C.; Brisson, A.; Borsali, R. Towards an easy access to Annexin-A5 protein binding block copolymer micelles, *Mater. Sci. Eng. C,* **2008**, (28), 479–488. *http://dx.doi.org/10.1016/j.msec.2007.04.025*

4. Giacomelli, C.; **Schmidt, V**.; Borsali, R. Specific interactions improve the payload capacity of block copolymer micelles in aqueous media, *Langmuir* **2007**, 23, 6947-6955. http://dx.doi.org/10.1021/la700337s

5. Giacomelli, C.; **Schmidt, V**.; Borsali, R. Nano-containers formed by self-assembly of poly(ethylene oxide)-b-poly(glycerol monomethacrylate) – drug conjugates, *Macromolecules* **2007,** 40, 2148-2157. http://dx.doi.org/10.1021/ma062562u

Articles in preparation

6 **Schmidt, V.;** Giacomelli, C.; Tessie, C. ; Lai-Kee-Him, J.; Brisson, A. R.; Borsali, R. Quartz crystal microbalance and electrophoresis analyses of Annexin-A5 protein binding block copolymer micelles. **2008**, *in prep*.

7 **Schmidt, V.**; Di Cola, E.; Giacomelli, C.; Brisson, A. R.; Narayanan, T.; Borsali, R. Nanostructured thin block copolymer films for precise positioning of protein arrays. **2008**, *in prep.*

List of Figures

169

List of Schemes

List of Schemes

List of Tables

List of Abbreviations and Symbols

A_2	Second virial coefficient
AFM	Atomic Force Microscopy
ATRP	Atom transfer radical polymerization
bpy	2,2'-bipyridyl
BSA	Bovine serum albumin
χ	Flory-Huggins interaction parameter
CAC	Critical Association Concentration
C_{lip}	Lipid concentration
CMC	Critical micelle concentration
C_p	Concentration of polymer
CRP	Controlled radical polymerization
Cryo-TEM	Cryo-transmission electron microscopy
C_s	Salt concentration
D	Diffusion coefficient
D	dissipation
ΔF	Frequency shift
DLS	Dynamic light scattering
$DOPC$	1,2-dioloeyl-sn-glycero-3-phosphocoline
DOPS	dioleoyl-phosphatidylserine
DP	Degree of polymerization
EGTA	ethylene glycol tetraacetic acid
Et_3N	Triethylamine
ϕ	Volume fraction
F	Fluorescence intensity
Γ	Relaxation frequency

GPC	Gel permeation chromatography
η	Viscosity
HMDS	hexamethyldisilazane
HMTETA	1,1,4,7,10,10-Hexamethyltriethylenetetramine
$I(q)$	Scattered intensity at the wavevector q
K_a	Acid dissociation constant
k_B	Boltzmann constant
K_V	Partition Coefficient
λ	Wavelength
LS	Light scattering
LUV	Large Unilamellar Vesicle
MLV	Multilamellar vesicle
M_n	Number average molecular weight
M_w	Weight average molecular weight
$M_{w,mic}$	Weight average molecular weight of micelles
$M_{w,unimers}$	Weight average molecular weight of unimers
M_w/M_n	Polydispersity
n	Refractive index
N_{agg}	Aggregation number
NMR	Nuclear magnetic resonance
N_x	Degree of polymerization of monomer X
P	Form factor
PAA	Poly(acrylic acid)
PAGE	Polyacrylamide gel electrophoresis
PBuA-*b*-PECVPD	poly(*n*-butyl acrylate)-b-poly((1-ethoxycarbonyl)vinylphosphonic diacid)

PEG	Poly(ethylene glycol)
PEMA	2-phospatethyl methacrylate
pH$_{mic}$	pH of micellization
PMA	Poly(methacrylic acid)
PS	Polystyrene
PS-*b*-P(PEMA-*co*-HEMA)	Polystyrene-*b*-poly(2-phosphatethyl methacrylate-*stat*-2-hydroxyethyl methacrylate)
PSS	Poly(styrene sulphonic acid)
Py	Pyrene
θ	Scattering angle
q	Wavevector
QCM-D	Quartz Crystal Microbalence with Dissipation monitoring
R_c	Core radius
R_g	Radius of gyration
R_H	Hydrodynamic radius
SEC	Size exclusion chromatogaphy
SK	Solketal
SLB	Supported Lipid Bilayer
SLS	Static light scattering
SPB	Spherical polyelectrolyte brushes
SUV	Small Unilamellar vesicle
τ	Relaxation time
T	Temperature
TEM	Transmission electron microscopy
T_g	Glass transition temperature
W	Corona width

Acknowledgments

This manuscript reports the results obtained during a 3-year period of work within the context of a joint collaboration between the Laboratoire de Chimie des Polymères Organiques (LCPO-ENSCPB-UMR-5629) and the Laboratoire de Chimie et Biologie des Membranes et Nanoobjets (CBMN, UMR-5248).

I wish to express in this part my gratitude to the scientists, technicians and other people who were directly or indirectly involved in this work, without the help of whom the findings of this thesis would not have been so multifaceted and prolific.

I would like to sincerely thank Dr. H. Cramail (Director of LCPO) and Dr. Y. Gnanou (former Director of LCPO) for giving such an opportunity to prepare my PhD thesis.

I owe special thanks for all the members of the committee – Prof. P. Labbé (Université Joseph Fourier, France), Prof. C. Rochas (Université Joseph Fourier, France), Prof. A. Brisson (Université Bordeaux 1, France), Prof. V. Soldi (Universidade Federal de Santa Catarina, Brazil), Dr. A. Deffieux (Université Bordeaux 1, France) and Dr. R. Borsali (CERMAV, France) – for helpful discussions, comments and contributions that improved and created new perspectives related to the present work.

The financial support from the Conselho Nacional de Desenvolvimento Científico e Tecnológico (CNPq, Brazil) and Centre Nationale de la Recherche Scientifique (CNRS, France), is deeply acknowledged.

I would like to tender my heartfelt thanks to my advisors, Dr. Redouane Borsali and Dr. Alain Brisson, for giving me the opportunity to do my PhD thesis under their supervision, working on this interesting project and all the fruitful results. I wish to express my appreciation to them for giving me enough freedom and independence in this successful endeavor, and their constant enthusiasm for open discussions. I really appreciated their guidance through the theoretical and practical aspects of my research. Many thanks, Dr. Borsali and Dr. Brisson.

I would like to thank Dr. J. Lai-Kee-Him, and C. Tessier for their valued contribution to my work regarding the preparation, manipulation and characterization of protein-containing systems.

Vanessa